IN-43

1638

NASA Contractor Report 4347

P 141

Theory of CW Lidar Aerosol Backscatter Measurements and Development of a 2.1-μm Solid-State Pulsed Laser Radar for Aerosol Backscatter Profiling

M. J. Kavaya, S. W. Henderson,
and R. G. Frehlich

CONTRACT NAS8-37580
MARCH 1991

NASA Contractor Report 4347

Theory of CW Lidar Aerosol Backscatter Measurements and Development of a 2.1-μm Solid-State Pulsed Laser Radar for Aerosol Backscatter Profiling

M. J. Kavaya, S. W. Henderson,
and R. G. Frehlich
Coherent Technologies, Inc.
Boulder, Colorado

Prepared for
George C. Marshall Space Flight Center
under Contract NAS8-37580

NASA
National Aeronautics and
Space Administration
Office of Management
Scientific and Technical
Information Division

1991

FOREWORD

This final report presents the results of work performed by Coherent Technologies, Inc. under contract NAS8-37580 for NASA Marshall Space Flight Center. The contract covered the period 29 July 1988 to 1 September 1990.

ACKNOWLEDGMENTS

The technical monitor of this contract was William D. Jones. The authors appreciate the technical contributions of Charley P. Hale, R. Milton Huffaker, James R. Magee, and Paul J. Suni; the computer programming assistance of Daniel B. Austin, A. Vincent Huffaker, Edward C. Russell, and Michael L. Smith; and many contributions by Vicky M. Judish, including the preparation of this report.

TABLE OF CONTENTS

1. INTRODUCTION

The aerosol backscatter coefficient β $[m^2 m^{-3} sr^{-1} = m^{-1} sr^{-1}]$ is defined as the fraction of incident electromagnetic energy at wavelength λ [m] which is scattered by atmospheric aerosol particles in the backward direction per unit solid angle, per unit atmospheric length (Measures, 1984, pgs. 53 and 239, and Kavaya and Menzies, 1985). It is assumed to be constant over the measurement volume of interest. In general, the atmospheric scattering (including backscattering) will be due to a complex distribution of scatterers that vary in composition, size, and shape. In order to account for arbitrary polarizations of the incident and scattered (detected) light, β must be generalized to a 4 x 4 Mueller matrix (Kavaya, 1987; Anderson, 1989). Once the Stokes vectors of the incident and detected light are specified, e.g. for a specific laser radar (lidar) system, then the backscattered energy is proportional to a weighted sum of a subset of the 16 β Mueller matrix elements. The weighted sum may be considered an effective scalar value of β. This will be assumed here.

A LIght Detection And Ranging (lidar) system may measure β in many different ways: 1) the lidar may be continuous-wave (CW) or pulsed; 2) the lidar may employ direct detection or heterodyne detection; 3) the laser beam may be focused or collimated; and 4) the measurement volume may contain numerous aerosol particles (volume mode - VM), a few particles, or only one particle at a time (single particle mode - SPM). The NASA GLObal Backscatter Experiment (GLOBE) program is attempting to increase the knowledge data base of global aerosols and their backscatter coefficient with particular emphasis on assisting the design of the proposed NASA Laser Atmospheric Wind Sounder (LAWS) lidar system. This Earth-orbiting wind profiling lidar will depend on aerosol backscatter for its signal. It will most likely be a pulsed, heterodyne (coherent) detection, collimated lidar system making global β measurements in the volume mode over the entire troposphere. If it orbits at a height of 800 km and if the laser beam has a nadir angle of 52.7^0, for example, then the interaction of the laser light with tropospheric aerosol particles will occur at a range of 1500 km with an effective (local) nadir angle of 63.5^0. The relative Doppler shift between the laser light and the aerosol particles will depend on the satellite velocity, the lidar's azimuth scan angle, the latitude, and the wind velocity.

This contract effort addressed the measurement and calibration of β by a CW, coherent detection, focused lidar system operating either in single particle mode or in volume mode. It will be shown that within reasonable assumptions, the value of β measured by the CW VM or SPM lidar is identical to the β value which affects the LAWS instrument performance.

Other important issues of position (latitude, longitude, altitude), spatial resolution, time, temporal resolution, wavelength, Doppler shift, incident and detected polarizations, atmospheric conditions, origin of air mass, recent weather conditions, measurement volume size and shape, and lidar beam-to-measurement volume orientation are not addressed here.

In Section 9 we describe the work performed in development and testing of a 2-μm Tm,Ho:YAG coherent lidar system. The system was recently moved to the Table Mountain remote field site (~ 10 miles north of Boulder, CO). Preliminary hard target and atmospheric data are presented in Section 9.3. We believe this to be the first demonstration of a coherent eyesafe solid-state lidar system.

2. OVERVIEW OF THEORY

The aerosol backscatter coefficient β is a measure of the average power backscattered by the atmosphere. For coherent detection laser radar, the transmitted beam is confined to a narrow angular region of the atmosphere. This permits the propagation, scattering, and reception of the fields to be described by Fresnel diffraction theory. For coherent detection lidar, the intermediate frequency (IF) signal from the detector $I_S(t)[A]$ is the basic signal for generating statistics to estimate β. Since the IF signal is a random quantity, a statistical estimate for β (a function of IF signal samples that approximates the true value of β) is required.

A satisfactory estimate for β requires that it is an unbiased estimate of β and that the estimate is accurate. Both volume mode (VM) and single particle mode (SPM) estimates of β are unbiased for ideal operating conditions. The ideal operating condition for the SPM method requires that the "threshold level" for identifying single particle events is low enough to sample enough of the scattering particles that contribute to β.

The accuracy of the estimates is affected by three main sources of error: 1) the additive noise of the detector, 2) the random fluctuations of the heterodyne power, and 3) the systematic errors of the system. The relative errors of these three components are denoted by $\frac{\Delta\beta(noise)}{\beta}$, $\frac{\Delta\beta(random)}{\beta}$, and $\frac{\Delta\beta(systematic)}{\beta}$, respectively. If all these errors are small, then the total relative error (i.e., accuracy of estimate or figure of merit) of the estimate is

$$\frac{\Delta\beta}{\beta} = \left[\left[\frac{\Delta\beta(noise)}{\beta}\right]^2 + \left[\frac{\Delta\beta(random)}{\beta}\right]^2 + \left[\frac{\Delta\beta(systematic)}{\beta}\right]^2\right]^{1/2} \tag{1}$$

Note that $\Delta\beta$ (noise) is related to the signal-to-noise ratio (SNR), $\Delta\beta$(random) arises from the random heterodyne detection process, and $\Delta\beta$(systematic) is linked to sensitivity analysis.

The merit of any unbiased estimate of β is then given by this total relative error. The first two error terms will be considered in this report, for both VM and SPM operation. The systematic error requires involved calculations of the actual lidar system parameters. This analysis may be the most important since systematic errors may be the dominant source of error. Sensitivity analysis is one part of systematic error analysis. Quantitative analysis of performance will be obtained using the current Marshall Space Flight Center (MSFC) CW coherent lidar system parameters [W.D. Jones, personal communication, 12/9/89 & 1/4/90].

3. VOLUME MODE (VM) MEASUREMENTS OF β

3.1 Introduction

A coherent detection lidar [See Figure 1] consists of a transmitter laser described by the scalar field $E_T(\vec{u},z)[(Wm^{-2})^{1/2}]$ where $\vec{u} = (u_x, u_y)[m]$ is the transverse coordinate at a propagation distance $z[m]$; a dimensionless effective receiver lens $W(\vec{v})$ where $\vec{v} = (v_x, v_y)[m]$ is the transverse coordinate in the receiver plane $z = 0$; a detector in the plane $z = L$ described by the quantum efficiency function $\eta(\vec{w})[electrons/photon]$ at transverse coordinate $\vec{w}[m]$ on the detector surface; and a local-oscillator (LO) field $E_{LO}(\vec{v},z)$. The irradiance profile of the transmitter beam $I_T(\vec{u},z)[Wm^{-2}]$ is given by

$$I_T(\vec{u},z) = E_T(\vec{u},z)E_T^{*}(\vec{u},z) \tag{2}$$

and normalized such that

$$P_T = \int_{-\infty}^{\infty} I_T(\vec{p},z)d\vec{p} \tag{3}$$

where $P_T[W]$ is the power of the transmitted beam in the absence of extinction.

An analytic expression for lidar performance can be obtained for a Gaussian lidar system; i.e., when

$$E_T(\vec{u},0) = \left[\frac{P_T}{\pi r_T^2}\right]^{1/2} \exp\left[-\frac{u^2}{2r_T^2} - \frac{iku^2}{2F_T}\right] \tag{4}$$

is the transmitter field,

$$W(\vec{v}) = \exp\left[-\frac{v^2}{2r_R^2} - \frac{ikv^2}{2F_R} \right] \tag{5}$$

is the receiver lens, and

$$E_{LO}(\vec{v},0) = \left[\frac{P_{LO}}{\pi r_T^2} \right]^{1/2} \exp\left[-\frac{v^2}{2r_{LO}^2} - \frac{ikv^2}{2F_{LO}} \right] \tag{6}$$

is the LO field backpropagated to the receiver plane $z = 0$. The parameters r_T, r_R, and r_{LO} [m] represent e^{-1} (37%) intensity radii; and the parameters F_T, F_R, and F_{LO} [m] represent phase curvatures. (The actual MSFC CW coherent focused lidar systems may have truncated Gaussian transmitted and LO beams due to a 15 cm diameter rectangular or "top hat" receiver mirror function. The solution for this case is much harder and may not lead to an analytic expression.) The current MSFC CW lidar system will be modeled as a matched monostatic Gaussian lidar:

$r_T = r_{LO} = 0.02157\ m$, transmitter and local oscillator 1/e intensity radii ($1/e^2$ radii = 0.0305m)

$r_R = \infty$, no truncation of the LO by the receiver

$F_T = F_R = F = 10.59\ m$, transmitter and receiver radius of curvature

$F_{LO} = \infty$, local oscillator phase radius of curvature at receiver plane

$\lambda = 9.114519\ \mu m$, CO_2 laser wavelength [9R(20) line of $^{12}C^{18}O_2$ isotope]

$\eta = 0.12$, optical transmission + detector AC quantum efficiency [electrons/photon]

$P_T = 4\ W$, transmitted power

$B_{VM} = 100\ kHz$, VM bandwidth (SAW)

$B_{SPM} = 1.5\ MHz$, SPM bandwidth

$V_A T \cos\theta = 100\ m$

$V_A\,[m/s] =$ airplane velocity

$T\,[s] = 1$s observation time

$\theta\,[rad] =$ angle between lidar optical axis and the perpendicular to the airplane velocity vector

Volume mode operation occurs when many scattering aerosols are illuminated by the transmitter laser. The statistics of the backscattered field is then described as a complex Gaussian random process which is sometimes called speckle statistics. The backscattered field from the aerosols is collected by the receiver lens and mixed with the local oscillator field in the detector plane. The square of the IF signal i_S^2 $[A^2]$ (obtained using a square-law-detector) is the coherent IF power. If the detector is larger than the local oscillator beam and if the detector quantum efficiency is uniform over the illuminated area of the local oscillator, and if the additive shot noise is negligible, then the average IF power is related to β by (see Appendix A)

$$<i_S^2> = \beta G_V P_T \tag{7}$$

where $<\bullet>$ denotes ensemble average, G_V is the system gain $[A^2\, m\ sr\ W^{-1}]$, i.e.,

$$G_V = \int_0^{\infty} G_V(R)\, dR \tag{8}$$

and

$$G_V(R) = 2\left(\frac{\eta G_D e}{h\nu}\right)^2 \frac{\lambda^2}{P_T} \int_{-\infty}^{\infty}\int_{-\infty}^{\infty}\int_{-\infty}^{\infty} <I_T(\vec{\mathbf{p}},R)\, G(\vec{\mathbf{v}}_1,\vec{\mathbf{p}},R)\, G^*(\vec{\mathbf{v}}_2,\vec{\mathbf{p}},R)>$$

$$W(\vec{\mathbf{v}}_1) W^*(\vec{\mathbf{v}}_2) E_{LO}{}^*(\vec{\mathbf{v}}_1,0) E_{LO}(\vec{\mathbf{v}}_2,0)\, d\vec{\mathbf{v}}_1\, d\vec{\mathbf{v}}_2\, d\vec{\mathbf{p}} \tag{9}$$

is the volume mode coherent lidar system range gain density $[A^2\, sr\ W^{-1}]$ as a function of range $R\,[m]$. Here, G_D = dimensionless amplifier gain, $h = 6.626\text{x}10^{-34}$ $[Js]$ is Plancks constant, and $G(\vec{\mathbf{v}},\vec{\mathbf{p}},R)[m^{-2}]$ is the Green's function; i.e., the field at $(\vec{\mathbf{v}},0)$ due to a unit point source at $(\vec{\mathbf{p}},R)$. Under the Fresnel approximation and no extinction

$$G(\vec{\mathbf{v}},\vec{\mathbf{p}},R) = \frac{k}{2\pi i R}\exp\left[\frac{ik}{2R}(\vec{\mathbf{v}} - \vec{\mathbf{p}})^2\right] \tag{10}$$

where $k = 2\pi/\lambda$ $[m^{-1}]$ is the wavenumber of the optical field. The system range gain density function identifies the dominant scattering regions as a function of range.

The aerosol backscatter coefficient $\beta[m^{-1}\,sr^{-1}]$ is given by

$$\beta = \int_0^\infty \sigma n(\sigma) d\sigma \tag{11}$$

where $n(\sigma)\,[m^{-5}sr]$ is the number of aerosol particles per unit volume per unit cross-section $\sigma[m^2\,sr^{-1}]$ and is assumed to be constant over the measurement volume defined by $G_V(R)$. The system gain G_V can be determined from the system components which requires integration of Eq. (9), which is difficult for a real system. Alternatively, the system gain G_V can be characterized by a measurement of $G_V(R)$ at appropriate ranges R.

Since a measurement of lidar IF power includes the additive shot noise signal $i_n(t)$, the correct statistic for VM measurement of β is

$$P = P(signal) - P(noise) \tag{12}$$

where

$$P(signal) = \frac{1}{T}\int_0^T i_S^2(t)dt \tag{13}$$

is an estimate of the IF coherent signal power $[A^2]$ with shot noise included for an observation time $T[s]$, and

$$P(noise) = \frac{1}{T}\int_0^T i_n^2(t)dt \tag{14}$$

is an estimate of the IF noise power $[A^2]$. The estimate $P\,[A^2]$ is an unbiased estimate of β, i.e.,

$$<P> = \beta\, G_V\, P_T\ . \tag{15}$$

The dimensionless lidar SNR is the average coherent lidar power $<i_S^2>$ normalized by the average noise power $<i_n^2>$. For the given assumptions

$$SNR = \beta G_{SNR} P_T \tag{16}$$

where the system gain $[m\ sr\ W^{-1}]$ for SNR is

$$G_{SNR} = \frac{\lambda^2\eta}{h\nu B P_{LO}} \int_0^{\infty} \int_{-\infty}^{\infty} \int_{-\infty}^{\infty} \int_{-\infty}^{\infty} < I_T(\vec{p},R) G(\vec{v}_1,\vec{p},R) G^*(\vec{v}_2,\vec{p},R) >$$

$$W(\vec{v}_1) W^*(\vec{v}_2) E_{LO}{}^*(\vec{v}_1,0) E_{LO}(\vec{v}_2,0)\, d\vec{v}_1\, d\vec{v}_2\, d\vec{p}\, dR \tag{17}$$

where

$$P_{LO} = \int_{-\infty}^{\infty} |E_{LO}(\vec{v},L)|^2 d\vec{v} \tag{18}$$

is the LO power [W] measured by the detector. Then

$$G_{SNR} = \int_0^{\infty} G_{SNR}(R)\, dR, \tag{19}$$

where $G_{SNR}(R)$ $[sr\ W^{-1}]$ is the SNR range density function. $G_{SNR}(R)$ can also be determined from system parameters but this is difficult to do accurately.

The system range density function $(G_V(R), G_{SNR}(R))$ indicate the regions of propagation range that are most important for system performance. Another measure of this behavior is the cumulative distribution function (CDF) defined by

$$CDF(R) = \frac{\int_0^{R} G_V(R')\, dR'}{\int_0^{\infty} G_V(R)\, dR} \tag{20}$$

which indicates the fraction of the signal statistic from aerosols with range less than R.

For the Gaussian lidar system, the range density function is

$$G_V(R) = 8\pi \left[\frac{\eta G_D e}{h\nu}\right]^2 \frac{P_{LO} r_E^2 [K(R)]^2}{r_{LO}^2 R^2 \left[\frac{1}{r_T^2} + \frac{1}{r_E^2} + (1-\frac{R}{F_T})^2 \frac{k^2 r_T^2}{R^2} + (1-\frac{R}{F_R} + \frac{R}{F_{LO}})^2 \frac{k^2 r_E^2}{R^2}\right]} \tag{21}$$

where

$$\frac{1}{r_E^2} = \frac{1}{r_R^2} + \frac{1}{r_{LO}^2} \tag{22}$$

and $K(R)$ is the dimensionless one-way irradiance extinction.

For the Gaussian lidar system, the SNR range density function is

$$G_{SNR}(R) = \frac{4\pi\eta r_E^2[K(R)]^2}{h\nu B_{VM} r_{LO}^2 R^2\left[\frac{1}{r_T^2} + \frac{1}{r_E^2} + (1-\frac{R}{F_T})^2\frac{k^2 r_T^2}{R^2} + (1-\frac{R}{F_R} + \frac{R}{F_{LO}})^2\frac{k^2 r_E^2}{R^2}\right]} \tag{23}$$

In the limit as $R \rightarrow 0$, the range density function approaches a constant. Normalizing the range density function by this constant produces

$$G_{VN}(R) = \frac{k^2(r_T^2 + r_E^2)}{R^2\left[\frac{1}{r_T^2} + \frac{1}{r_E^2} + (1-\frac{R}{F_T})^2\frac{k^2 r_T^2}{R^2} + (1-\frac{R}{F_R} + \frac{R}{F_{LO}})^2\frac{k^2 r_E^2}{R^2}\right]} \tag{24}$$

Performing the integrals in Eqs. (8) and (19) for the matched monostatic model of the MSFC lidar, uniform β, and constant extinction K produces

$$G_V = 2\lambda P_{LO}\left[\frac{KG_D\eta e}{h\nu}\right]^2\left[\frac{\pi}{2} + \tan^{-1}(kr^2/F)\right] \tag{25}$$

and

$$G_{SNR} = \frac{\lambda\eta K^2}{h\nu B_{VM}}\left[\frac{\pi}{2} + \tan^{-1}(kr^2/F)\right] \tag{26}$$

The total system gain for a focused lidar will vary by only a factor of two for any change in radius of curvature F or beam dimensions r, assuming uniform β and constant K. Therefore, these parameters can be chosen to improve other aspects of system performance.

3.2 Error Due to Additive Shot Noise

For the VM estimate of β, a measure of the shot noise component of error is defined as

$$\frac{\Delta\beta(noise)}{\beta} = \frac{(VAR\,[P\,(noise)])^{1/2}}{<P>} = \frac{<i_n^2>}{<P>(TB_{VM})^{1/2}} \qquad (27)$$

where $B_{VM}\,[Hz]$ is the VM bandwidth of the square-law-detector and the noise power has been accurately estimated from a calibration run. For the MSFC matched monostatic system using the SAW spectrum analyzer with a 100 kHz bandwidth,

$$\frac{\Delta\beta(noise)}{\beta} = \frac{h\nu B_{VM}}{\pi\lambda\beta P_T\eta\cos\theta(TB_{VM})^{1/2}} = \frac{5.02\mathrm{x}10^{-13}}{\beta\cos\theta} \qquad (28)$$

For $\cos\theta = 1$ and $\beta = 10^{-12}\,m^{-1}sr^{-1}$, $\frac{\Delta\beta(noise)}{\beta} = 0.5$, which is detectable (50% error). An observation time of $T = 10\,s$ would produce $\frac{\Delta\beta(noise)}{\beta} = 0.16$, and an observation time of $T = 100\,s$ would yield $\frac{\Delta\beta(noise)}{\beta} = 0.05$ (5% error).

3.3 Error Due to the Random Process

The error of the VM estimate for β due to the random fluctuations in heterodyne power is the dominant source of error for high SNR and negligible systematic error. For ideal VM performance, the heterodyne power has "speckle statistics," i.e., the IF current is a zero-mean complex Gaussian random process and the heterodyne power has a negative exponential distribution. For focused VM operation, the IF power may be characterized by single particle events. The IF power then has non-ideal statistics (not speckle statistics) and a more complex analysis must be performed.

The variance of the VM estimate P [Eq. (12)] due to speckle statistics is

$$VAR\,[P\,] = \frac{<P>^2 T_d}{T} \qquad (29)$$

where T_d $[s\,]$ is the temporal decorrelation time of the "speckle process." The accuracy of P is then

$$\frac{\Delta\beta(random)}{\beta} = \frac{(VAR\,[P\,])^{1/2}}{<P>} = [T_d/T\,]^{1/2} \tag{30}$$

For $T_d = 1\mu s$, $\frac{\Delta\beta(random)}{\beta} = 0.001 = 0.1\%$, assuming a $T = 1\ s$ observation time.

3.4 Calibration of VM Measurement of β

VM measurements of β can be calibrated using a diffuse target with reflection coefficient $\rho\ [sr^{-1}]$. The backscattered irradiance $I\,(\vec{v},0)\ [Wm^{-2}]$ at the receiver is given by

$$I\,(\vec{v},0) = \frac{\rho P_C}{R^2} \tag{31}$$

where $P_C\,[W\,]$ is the calibration power transmitted onto the target. The average coherent IF power from the hard target at range R is then

$$<i_S^2(R\,)>_C\ = \rho P_C\, G_V(R\,) \tag{32}$$

yielding

$$G_V(R\,) = \frac{<i_S^2(R\,)>_C}{\rho P_C} \tag{33}$$

as a measure of $G_V\,(R\,)$. The system gain G_V is obtained by integration of $G_V(R\,)$ with respect to R.

As with calibration of lidar power range density, a measurement of SNR from a known hard diffuse target is a measure of $G_{SNR}\,(R\,)$; i.e.,

$$G_{SNR}\,(R\,) = \frac{SNR\,(R\,)}{\rho P_C}\ . \tag{34}$$

4. SINGLE PARTICLE MODE (SPM) MEASUREMENTS OF β

4.1 Introduction

A focused CW lidar beam will have an effective sensitivity or gain along its optical axis which is peaked at the focus. For a tightly focused lidar beam, and for sufficiently low values of β (this implies low particle concentration), the received signal power will be characterized by randomly occurring events as particles of different composition, size, and shape traverse the focused beam at different ranges along the optical axis $R\,[m]$ and at different distances $p_x\ [m]$ above or below the optical axis. We assume the lidar system is moving through the atmosphere with velocity V_A in the direction of the $+y$ axis (e.g., in an aircraft) and that it is aimed in the $y-z$ plane at an angle to the $+z$ axis (see Figure 2). For example, θ was $+17.44^0$ during a recent flight measurement program (Gras et al, 1988).

The maximum lidar signal $S_j(p_x, p_{ym}, R)\ [A^2]$ for the jth particle event will occur at some coordinate $(p_x, p_{ym}, R) = (\vec{p}_m, R)$ of the trajectory, where p_x is the displacement from the laser beam axis. The proper statistic for estimating β in the absence of additive noise (see Section 4.6 for correction for noise spikes) is the sum S $[A^2]$ of the maximum (or peak) signals:

$$S = \sum_{j=1}^{N} S_j(p_x, p_{ym}, R) \tag{35}$$

If the threshold for the identification of peak signals is low enough to identify all the scattering particles, then

$$<S> = \beta V_A T P_T G_S \cos\theta \tag{36}$$

where $G_S\,[A^2 W^{-1} sr]$ is the total system gain given by

$$G_S = \int_0^{\infty}\int_{-\infty}^{\infty} G_S(p_x, R)\,dp_x\,dR \tag{37}$$

and

$$G_S(p_x,R) = 2P_T\left[\frac{\eta G_D e}{h\nu}\right]^2 \int_{-\infty}^{\infty}\int_{-\infty}^{\infty} \frac{J_T(\vec{p}_m,R)}{R^2}\exp\left[\frac{ik}{2R}\left[(\vec{p}_m - \vec{v}_1)^2 - (\vec{p}_m - \vec{v}_2)^2\right]\right]$$

$$W(\vec{v}_1)W^*(\vec{v}_2)E_{LO}{}^*(\vec{v}_1,0)E_{LO}(\vec{v}_2,0)d\vec{v}_1 d\vec{v}_2 \tag{38}$$

is the system's transverse area gain density $[A^2W^{-1}m^{-2}sr\ ]$ for a scattering particle at $(\vec{p}_m,R)$ and

$$J_T(\vec{p},R) = \frac{I_T(\vec{p},R)}{P_T} \tag{39}$$

is the normalized transmitter irradiance $[m^{-2}]$ at transverse coordinate $\vec{p}\,[m]$ and range R. For the general Gaussian lidar system, the ensemble average of the normalized transmitted beam profile is then

$$<J_T(\vec{p},R)> = \frac{1}{\pi r_B^2(R)}\exp\left[-\frac{p^2}{r_B^2(R)}\right] \tag{40}$$

where

$$r_B^2(R) = r_T^2(1-\frac{R}{F_T})^2 + (\frac{R}{kr_T})^2 + 2[\frac{R}{kS_0(R)}]^2, \tag{41}$$

where r_B is the e^{-1} intensity radius $[m]$ of the ensemble averaged transmitted beam profile, and

$$S_0(R) = \left[Hk^2\int_0^R C_n^2(R')(1-\frac{R'}{R})dR'\right]^{-3/5} \tag{42}$$

is the field coherence length $[m]$ due to refractive turbulence, $H = 2.914383$, and $C_n^2(R)\ [m^{-2/3}]$ is the refractive index structure constant profile. The last term in Eq. (41) is the spread of the transmitted beam profile due to Kolmogorov refractive turbulence with zero inner scale. This effect must be negligible for simple calibration. If it is not negligible, then the calibration will depend on refractive turbulence conditions. We assume it is negligible in this paper.

The transverse area gain density function $G_S(p_x,R)$ for this idealized system is

$$G_S(p_x,R) = 8\left[\frac{\eta G_D e}{h\nu}\right]^2 \frac{P_{LO} r_E^2}{k^2 r_{LO}^2 r_B^2(R) r_M^2(R)} \exp\left[-\frac{p_x{}^2}{r_B^2(R)} - \frac{p_x{}^2}{r_M^2(R)}\right] \tag{43}$$

where

$$\frac{1}{r_E^2} = \frac{1}{r_R^2} + \frac{1}{r_{LO}^2} \tag{44}$$

and the effective receiver area is πr_E^2, and

$$r_M^2(R) = r_E^2\left(1 - \frac{R}{F_R} + \frac{R}{F_{LO}}\right)^2 + \left(\frac{R}{k r_E}\right)^2. \tag{45}$$

$r_M(R)\,[m]$ is the contribution to the gain function from phase mismatch between the received field and the local oscillator.

The range gain density function $G_S(R)[A^2W^{-1}m^{-1}sr]$ is obtained by integrating $G_S(p_x,R)$ over p_x, i.e.

$$G_S(R) = 8\pi^{1/2}\left[\frac{\eta G_D e}{h\nu}\right]^2 \frac{P_{LO} r_E^2}{k^2 r_{LO}^2 [r_B^2(R) r_M^2(R)(r_B^2(R) + r_M^2(R))]^{1/2}} \tag{46}$$

It is highly recommended that both theoretical and experimental sensitivity analyses of $G_S(R)$ be performed about a candidate operating point of the lidar system.

In the limit of small R

$$G_S(0) = 8\pi^{1/2}\left[\frac{\eta G_D e}{h\nu}\right]^2 \frac{P_{LO} r_E^2}{k^2 r_{LO}^2 [r_T^2 r_E^2 (r_T^2 + r_E^2)]^{1/2}} \tag{47}$$

$G_S(R)$ becomes independent of R for small R just as the VM range gain density function $G_V(R)$, did. We may normalize Eq. (46) with Eq. (47) to obtain

$$G_{SN}(R) = \frac{G_S(R)}{G_S(0)} = \frac{[r_T^2 r_E^2 (r_T^2 + r_E^2)]^{1/2}}{[r_B^2(R) r_M^2(R)(r_B^2(R) + r_M^2(R))]^{1/2}} \tag{48}$$

For the MSFC matched monostatic system, $[r_{LO} = r_T = r,\ F_{LO} = r_R = \infty,\ F_T = F_R = F,\ C_n^2 = 0]$

$$r_B^2(R) = r_M^2 = r_B^2 = r^2(1 - \frac{R}{F})^2 + (\frac{R}{kr})^2 \tag{49}$$

and

$$r_E^2 = r_{LO}^2 = r^2 . \tag{50}$$

Assuming $R = F$

$$G_{SN}(F) = \frac{k^3 r^6}{F^3 2^{3/2}} \tag{51}$$

If $R \to \infty$

$$G_{SN}(R \to \infty) \approx \frac{r^3 (3/4)^{1/2}}{R^3 \left[(\frac{r^2}{F^2} + \frac{1}{k^2 r^2})(\frac{r^2}{2F^2} + \frac{2}{k^2 r^2})(\frac{3r^2}{2F^2} + \frac{3}{k^2 r^2}) \right]^{1/2}} \tag{52}$$

For tightly focused conditions, it is safe to assume $F \ll kr^2/2$, so that Eq. (52) becomes

$$G_{SN}(R \to \infty) \approx \frac{F^3}{R^3} \tag{53}$$

If $F \gg kr^2$, Eq. (51) should be used with R substituted for F.

4.2 Error Due to Additive Shot Noise

For an unbiased estimate of β in SPM operation, the threshold level for signal spike identification must be low enough to sample the majority of aerosol particles that contribute to β. When this is satisfied, the contribution of noise spikes that are erroneously counted as signal spikes is negligible unless β is low and few spikes are observed. The error analysis will assume that the number of signal spikes is much larger than the number of noise spikes.

For the SPM estimate, the error due to additive shot noise is

$$\frac{\Delta\beta(noise)}{\beta} = \frac{(VAR\,[S\,(noise)])^{1/2}}{<S>} = \frac{<i_n^2><N_{spike}>^{1/2}}{<S>} = \frac{<i_n^2>}{<N_{spike}>^{1/2}<S_j>} \tag{54}$$

where $<N_{spike}>$ is the average number of spikes observed. For the MSFC matched monostatic Gaussian system

$$\frac{<i_n^2>}{<S_j>} = \frac{Fh\nu B}{4(2\pi)^{1/2} r V_A T P_T \beta\eta\cos\theta} \approx \frac{3.34\text{x}10^{-14}}{\beta\cos\theta} \tag{55}$$

Determining the error of the SPM estimate due to additive shot noise requires knowledge of the average number of spikes observed in the observation time T. This is given by

$$<N_{spike}> = V_A T \int_0^{\infty}\int_{-\infty}^{\infty}\left[\int_{\sigma_C(p_x,R)}^{\infty} n(\sigma)d\sigma\right]dp_x dR \tag{56}$$

where

$$\sigma_C(p_x,R) = \frac{h\nu B\varepsilon}{\eta P_T H(p_x,R)} \tag{57}$$

is the cross section $[m^2\, sr^{-1}]$ for particles at range R and offset p_x that produces a peak spike at the threshold of the peak detector and the function $H(p_x,R)$ $[m^{-2}\, sr]$ is

$$H(p_x,R) = \int_{-\infty}^{\infty}\int_{-\infty}^{\infty}\frac{J_T(\vec{p}_m,R)}{R^2 P_{LO}}\exp\left[\frac{ik}{2R}\left[(\vec{p}_m - \vec{v}_1)^2 - (\vec{p}_m - \vec{v}_2)^2\right]\right]$$

$$W(\vec{v}_1)W^*(\vec{v}_2)E_{LO}^*(\vec{v}_1,0)E_{LO}(\vec{v}_2,0)d\vec{v}_1 d\vec{v}_2 . \tag{58}$$

The function $H(p_x,R)$ is the normalized system gain at range R and offset p_x . The threshold is defined as $\varepsilon<i_n^2>$ and it is assumed that the contribution of the noise spikes above the threshold is negligible (see Section 4.6 for noise spike correction). For useful operation, $\varepsilon>3$, provided there are more signal spikes than noise spikes. If ε is not high enough, especially for low β, the number of noise spikes will become larger than the number of signal spikes, and it will be difficult to accurately correct for the noise spikes. For a matched monostatic Gaussian system with no beam truncation

$$H(p_x,R) = \frac{4}{k^2 r^4}\exp\left[-2\frac{p_x^2}{r_B^2}\right] \tag{59}$$

The average number of peak signals above the threshold level depends on system geometry and the form of the distribution of scattering cross section $n(\sigma)$.

4.3 Error Due to the Random Process

The accuracy of the SPM estimate of β, due to the random fluctuations of heterodyne power, is determined by the fluctuations in peak signal levels, i.e.,

$$\frac{\Delta\beta(random)}{\beta} = \frac{(VAR[S])^{1/2}}{<S>} = \frac{\beta_2^{1/2}\left[\int_{-\infty}^{\infty}\int_{0}^{\infty} H^2(p_x,R)\,dR\,dp_x\right]^{1/2}}{\beta[V_A T\cos\theta]^{1/2}\int_{-\infty}^{\infty}\int_{0}^{\infty} H(p_x,R)\,dR\,dp_x} \qquad (60)$$

where

$$\beta_2 = \int_0^{\infty} \sigma^2 n(\sigma)\,d\sigma \qquad (61)$$

is the second moment $[m\ sr^{-2}]$ of particle cross section. A small ratio of $\frac{\beta_2^{1/2}}{\beta}$ is desired (a narrow distribution of σ values for a small SPM random error). For the MSFC matched monostatic Gaussian system

$$\frac{\Delta\beta(random)}{\beta} = \frac{2^{3/4}k(r/F)^{3/2}\beta_2^{1/2}}{\beta[15V_A T\cos\theta]^{1/2}} \qquad (62)$$

An accurate estimate for β requires sampling many spikes, which samples the many different sized aerosols. If β is significantly affected by large particles, then the estimate for β can be poor since it would require a long time to observe the rare events due to the relatively few large particles. The first and second moments of β provide the insight into the importance of different sized particles within $n(\sigma)$ for accurately estimating β.

4.4 Calibration of SPM Measurement of β

The lidar system can be calibrated by shooting test particles with cross section σ_C through the laser beam of power P_C, at an angle $90^0 - \theta_C$, beam offset p_{xc}, and range R_C. The particle's cross section σ_C may be determined theoretically or experimentally. The maximum (peak) lidar signal S_C $[A^2]$ is

$$S_C(p_{xc}, R_C) = P_C \sigma_C G_S(p_{xc}, R_C) \tag{63}$$

Therefore,

$$G_S(p_{xc}, R_C) = S_C(p_{xc}, R_C)/(P_C \sigma_C) \tag{64}$$

may be experimentally determined. Ideally the measurement is deterministic, but averaging of multiple test particle shots may be employed to reduce noise, trajectory jitter, etc.

The total system gain G_S requires a 2-D integration over range R_C and offset p_{xc}. The integration over p_{xc} produces the system's range gain density $[A^2W^{-1}m^{-1}sr]$ as a function of range , i.e.,

$$G_S(R_C) = \int_{-\infty}^{\infty} G_S(p_{xc}, R_C) dp_{xc}, \tag{65}$$

which allows identification of the region (in R) of the maximum contribution to the overall system gain G_S. This region will be near the focus of the lidar system.

The dependence of the functions $G_S(p_x, R)$ and $G_S(R)$ on various system parameters is important for optimal design of a CW SPM lidar system, and for optimum calibration methodology. The calibration apparatus should span values of p_x and R sufficient to include, for example, all values of $G_S(p_x, R)$ down to 1% of its maximum value.

Assume that $\theta_C = \theta$, i.e., the trajectory of the calibration test particles through the laser beam is at the same angle as the trajectories of atmospheric aerosol particles during flight. Then, an estimate for β is [see Appendix B, Eq. (B6)]

$$\beta = \frac{\sum_{j=1}^{N} S_j}{P_T G_S V_A T \cos\theta} \tag{66}$$

The $\cos\theta$ dependence reflects that the effective sensing volume of the lidar decreases with increasing θ. For the same SPM statistic S, a larger value of θ implies a larger value of β.

Table 1 summarizes the assumptions made in arriving at Eq. (66) for calibrated SPM. Appendix C discusses the calibration methodology if the particular value of p_{xc} for a test particle is not known, but the probability density function (PDF) of the values of p_{xc} for many particles is known to be uniform.

Table 1. Assumptions of Calibration Methodology

1. Fresnel approximation (narrow angle scattering).
2. Negligible refractive turbulence.
3. Sufficient resolution and coverage in p_{xc} and R_C during calibration to accurately determine system gain.
4. $\theta_C = \theta$.
5. The test particle's velocity equals the atmospheric measurement lidar system velocity or the lidar system receiver gives the same peak signal reading for different particle speeds (i.e., flat bandwidth).
6. Known value of σ_C of test particles.
7. Good linear peak power detector.
8. Lidar system unchanged between calibration and aerosol backscatter measurements.
9. β represents weighted sum of 16 Mueller matrix elements.
10. Statistical process yielding peak signals is ergodic and stationary.
11. $n(\sigma)$ constant over dominant region of measurement volume.
12. β uniform over measurement volume.
13. Sufficiently large number of particle events during SPM atmospheric measurement.
14. Sufficient SNR.
15. The mean heterodyne signal power is available.
16. The heterodyne detector is bigger than the LO beam.

4.5. Requirements for SPM Operation

The requirements for accurate SPM estimates include:

1) Heterodyne power signal with well defined peak signals.
2) Enough peak signals above threshold to produce unbiased estimates of β.
3) Errors due to shot noise and statistical fluctuations in peak signals require knowledge of $n(\sigma)$.
4) Errors due to misalignment and optical mismatch (beam size and curvature) require numerical calculations.
5) Accurate method of obtaining peak signals:
    a) $\Delta\omega$ must be large enough to sample spike events. For the MSFC system and $V_A = 100\,m/s$, the spike events are $7.1\mu s$ (τ_w in Figure 3).
    b) Either average IF power (dashed line in Figure 3) is used or peak IF power (solid line in Figure 3) with no filtering is used. If $\tau_d \ll \tau_w$, then using a smoothing filter with time constant τ_f, where $\tau_d < \tau_f < \tau_w$, will produce a more accurate signal where the peak value is the average IF power of the signal. If $\tau_d = \tau_w$, then the maximum IF power must be used, and then the peak power $P_{peak} = 2\langle P_{peak}\rangle$, where $\langle P_{peak}\rangle$ is the peak of the average IF power $\langle i_S^2\rangle$ shown as the dashed line. If $\tau_d > \tau_w$, the IF frequency is not high enough to sample the single spike event and SPM is not recommended.

4.6. Noise Signal Correction for SPM

For low β, the number of signal spikes from aerosol scatterers will be small and the contribution from random noise spikes must be considered. An estimate that removes the contribution of noise spikes is

$$\hat{S} = \sum_{j=1}^{N} S_j(p_x, p_{ym}, R) - \langle N_{spike(noise)}\rangle\langle S_{noise}\rangle - [\langle N_{spike}\rangle - \langle N_{spike(noise)}\rangle]\langle i_n^2\rangle \qquad (67)$$

where $\langle N_{spike(noise)}\rangle$ is the average number of noise spikes above the threshold and $\langle S_{noise}\rangle$ is the average lidar power of the noise spikes. The second term corrects the contribution from noise spikes and the last term corrects the contribution of the additive noise power to the signal spikes. When the number of noise spikes is comparable to the number of signal spikes, the error analysis must be extended to include the noise spike contribution.

4.7. VM Random Error in SPM Regime

The VM estimate for β is unbiased even when operating in the SPM regime (i.e., the measurement volume does not include enough particles to cause speckle statistics). However, the random fluctuations of the heterodyne power are not characterized by exponential statistics but determined by the random fluctuations of the single particle events. The accuracy of the VM estimate due to these random fluctuations is given by

$$\frac{\Delta\beta(random)}{\beta} = \frac{(VAR\,[P\,])^{1/2}}{<P>} = \frac{\beta_2^{1/2}\left[\int_{-\infty}^{\infty}\int_{0}^{\infty} F^2(p_x,R)\,dR\,dp_x\right]^{1/2}}{\beta[V_A T\cos\theta]^{1/2}\int_{-\infty}^{\infty}\int_{0}^{\infty} F(p_x,R)\,dR\,dp_x} \tag{68}$$

where

$$F(p_x,R) = \int_{-\infty}^{\infty}\int_{-\infty}^{\infty}\int_{-\infty}^{\infty} \frac{J_T(\vec{p}_m,R)}{R^2 P_{LO}} \exp\left[\frac{ik}{2R}\left[(\vec{p}-\vec{v}_1)^2-(\vec{p}-\vec{v}_2)^2\right]\right]$$
$$W(\vec{v}_1)W^*(\vec{v}_2)E_{LO}{}^*(\vec{v}_1,0)E_{LO}(\vec{v}_2,0)\,d\vec{v}_1\,d\vec{v}_2\,dp_y \tag{69}$$

is the integrated IF power [W] for a single particle event with offset p_x. For the tightly focused MSFC matched monostatic Gaussian lidar system ($F \ll kr^2$)

$$\frac{\Delta\beta(random)}{\beta} = \frac{4\beta_2{}^{1/2}}{\pi^{5/4}\beta[6FrV_A T\cos\theta]^{1/2}} \tag{70}$$

5. SYSTEMATIC ERRORS

There are many systematic errors in lidar calibrations. These include nonuniformities in quantum efficiency over the detector; non-linearities in the photo detector and square-law-detector; errors in the parameters of the transmitter field, LO field, and receiver response; and fluctuations in all parameter settings after calibration is performed. The magnitude of the systematic errors that involve system parameters can be determined by a sensitivity analysis, which identifies which parameter settings cause the most change in system gain due to small changes from their nominal settings. A major source of sensitivity for coherent detection lidar is beam alignment. Ideal operation of coherent detection lidar requires an excellent match between the transmitted Gaussian beam and the back-propagated local oscillator (BPLO) beam, especially for tightly focused conditions. For VM operation and equal transmitter and BPLO radii, the effects of beam axis offset $\vec{d}\,[m]$ and pointing angle error $\Delta\vec{\theta}\,[rad]$ are given by

$$G_V(R) = G_{VI}(R)\exp[-(\Delta\vec{\theta}R + \vec{d})^2/(2r_B^2(R))] \tag{71}$$

where $G_{VI}(R)$ is the ideal system gain density with no misalignment between the transmitted beam and local oscillator beam. The effects of misalignment can be easily calculated.

For the focused system, the major contribution to β comes from a small region around the focus. An angle error of 67 μrad between a perfectly matched transmit beam and local oscillator beam would produce a 40% error in the estimate of β . An offset of 0.71 mm between a parallel transmit and LO beam would also produce a 40% error.

The error in the SPM estimate of β due to misalignment of the transmitter and LO beams can be calculated in a similar fashion as for the VM case. The behavior will be more complex but have a similar scaling.

SPM measurements suffer from a bias since a threshold is required to determine if a single particle event occurred. A measure of this bias is the ratio of the ensemble average of the SPM statistic with a threshold $<S_{th}>$ to the ensemble average with no threshold, i.e.

$$BIAS = \frac{<S_{th}>}{<S>} = \frac{\int_{0}^{\infty}\int_{-\infty}^{\infty} D_N[\sigma_C(p_x,R)]H(p_x,R)dp_x dR}{\int_{0}^{\infty}\int_{-\infty}^{\infty} H(p_x,R)dp_x dR} \tag{72}$$

where

$$D_N[x] = \frac{\int_{x}^{\infty}\sigma n(\sigma)d\sigma}{\int_{0}^{\infty}\sigma n(\sigma)d\sigma} = \frac{\int_{x}^{\infty}\sigma n(\sigma)d\sigma}{\beta} \tag{73}$$

is the fraction of β due to aerosol particles with a cross section σ larger than x.

6. COMPARISON OF VM AND SPM

6.1 Comparison of Range Gain Density Functions

Figure 4 shows the normalized range gain density functions for both SPM and VM plotted vs R/F for the MSFC matched monostatic Gaussian system. Both curves become independent of R and equal to 1 for small R. The SPM $G_S(R)$ falls as R^{-3} for large R [see Eq. (53)] and the VM SNR falls as R^{-2} for large R [see Eq. (24)]. This difference is due to the effective 1-D integral through the Gaussian beam in SPM and the effective 2-D integral over the entire Gaussian beam in VM. For large R the beam waist is proportional to R. Therefore the 1-D integral is proportional to R^{-1} and the 2-D integral is independent of R. Both SPM and VM have a further R^{-2} dependence due to the decreasing solid angle of the receiver aperture. It is difficult to tell from Figure 4 how big an interval in range must be included to account for 90% of the gain, for example. This requires the cumulative density function (CDF) of $G_S(R)$ and $G_V(R)$ [see Eq. (20)] which is plotted in Figure 5. Since $F_T = F_R$ = 10.59 m, the abscissa values of 0.9 and 1.1 correspond to R = 9.53 and 11.65 m, respectively. A slightly larger range interval is required for the VM case for equal percentages of the signal. Figures 6 and 7 show the same plots with the larger focal range and smaller beam radius used in a recent NASA GLOBE flight (W. D. Jones, personal communication, 4/20/90 and 9/18/90). Since $F_T = F_R = 50\,m$ in Fig. 7, the abscissa values of 0.5 and 1.5 correspond to R=25 and 75 m, respectively. As expected from Eq. (51), the SPM peak at $R = F$ (≈90) is approximately a factor of 9 10^{-3} smaller than the SPM peak at $R = F$ in Fig. 4 (≈10^4). Figure 8 shows the SPM $G_S(R)$ and the VM $G_V(R)$ for the same conditions as Figure 4 except $\lambda = 1.064158$ μm. The focusing is much tighter with the shorter wavelength. As expected from Eq. (51), the SPM peak at $R = F$ (≈6 10^6) is approximately a factor of 628 higher than the SPM peak in Fig. 4. The tighter focusing is also exhibited in the CDF curves of Figure 7.

6.2 Error Comparison

Calculations of SPM performance require the distribution of aerosol particle scattering cross-section $n(\sigma)$ $[m^{-5}sr]$. We assume a bi-modal, log-normal distribution of cross-section $n(\sigma)$ [David A. Bowdle, " $n(\sigma)$ Distributions," 1-31-90]:

$$n(\sigma) = \frac{\beta}{(2\pi)^{1/2} f(\chi)\sigma \ln[\delta_1]}\left[\exp\left[\frac{-\ln^2(\sigma/\sigma_1)}{2\ln^2\delta_1}\right] + \frac{\chi \ln\delta_1}{\ln\delta_2}\exp\left[\frac{-\ln^2(\sigma/\sigma_2)}{2\ln^2\delta_2}\right]\right] \tag{74}$$

where

$$f(\chi) = \sigma_1 \exp\left[\frac{\ln^2\delta_1}{2}\right] + \chi\sigma_2 \exp\left[\frac{\ln^2\delta_2}{2}\right] \tag{75}$$

is a normalizing parameter $[m^2sr^{-1}]$, $\sigma_1 = 2\text{x}10^{-12}\,m^2sr^{-1}$, $\sigma_2 = 3\text{x}10^{-15}\,m^2sr^{-1}$, and

$$\chi = \frac{A_2}{A_1} \tag{76}$$

where A_1 and A_2 are empirical coefficients $[m^{-3}]$ of the two aerosol modes, $\delta_1 = 1.4$ and $\delta_2 = 1.6$ are the dimensionless geometric standard deviations of the two aerosol modes, and where $n(\sigma)$ = Bowdle's $n(\sigma)$ $[m^{-3}]$ divided by σ $[m^2sr^{-1}]$. For this example we chose $\chi = 0.0003$.

The SPM gives a biased estimate of β because the smallest aerosol particles (values of σ) produce signal spikes below the threshold level, $\varepsilon\langle i_n^2 \rangle$. In this case $\beta_{measured} = 0.185\ \beta_{true}$, i.e., there is a -81% bias in addition to the two error sources. The bias is independent of β for SPM if the shape of $n(\sigma)$ does not change, (i.e., $\sigma_1, \sigma_2, \delta_1, \delta_2$, and χ are constant). Note that there is no bias for VM measurements of β. The value of ε is a free parameter. Raising ε will worsen the bias, cause less spikes to be seen in an observation time, but will reduce the number of noise spikes. Lowering ε will do the opposite. Moving to a tighter (closer) focus will lower (improve) the bias, but will increase alignment difficulty, and might cause the laser beam to change the properties of the aerosol particles. The effect this would have on $\langle N_{spike} \rangle$ is not clear.

Figure 10 shows the results for SPM. Both SPM noise error, and SPM random error assuming no bias due to the threshold level are plotted vs β. (The effects of bias due to threshold level on SPM random error could be calculated. A finite bias will increase SPM random error because the average number of spikes above the threshold decreases.) The average number of SPM signal events or spikes, $\langle N_{spike} \rangle = N$, that are greater than three times the average noise level ($3\langle i_n^2 \rangle$) in the measurement volume ($V_A T \cos\theta = 100m$) is shown in the figure. As long as the $n(\sigma)$ model is held constant, as in this case, N is proportional to β. Both sources of SPM error in β are proportional to $\beta^{-1/2}$. The curve $N^{-1/2}$, which is proportional to $\beta^{-1/2}$, is plotted for reference. In this example the random error is greater than the noise error and exceeds 10% when $\beta < 3\text{x}10^{-12}$. As β approaches 10^{-12}, the SPM number of spikes per observation time, N, approaches 1. It is very difficult to estimate β with a small number of signal spikes because of the large number of noise spikes. The noise spike correction of section 4.6 should be employed. Future analysis should include the effects of the noise spikes above the threshold. Increasing laser power will always improve SPM performance until the laser power begins to change the particles properties. The SPM analysis is only valid if indeed there are only single particle events.

Comparing SPM to VM is a difficult undertaking fraught with many subtleties. Figure 11 is similar to Figure 10, but the N and $N^{-1/2}$ curves are removed, and a VM noise error and two VM random error curves are added. The theory for VM error diverges whether one assumes operation in a single-particle regime or in a many-particle regime (Gaussian statistics). The VM error curves in Figure 11 assume the many-particle VM regime except for the curve for VM random error in the SPM regime. Here, the many signal spikes below the SPM threshold level are included in the VM estimate. This reduces the random fluctuations of the VM estimate compared to the SPM estimate which improves the VM accuracy. The random error for VM in the SPM regime may be better than the VM speckle regime. This can only be determined by calculating the boundary between the VM and SPM regimes. The VM random error in the speckle regime is independent of β and equals $[T_d/T]^{1/2}$. We assumed T_d = signal decorrelation time = $1\mu s$, and T = observation time = 1 s, yielding an error of 10^{-3} (0.1%). The VM noise error is proportional to β^{-1} and to $B^{1/2}$ [see Eq. (28)]. We assumed $B_{VM} = B_{SPM} = 1.5\,MHz$ for these calculations. In actual practice, one would try to reduce B_{VM} as much as possible. The curve may be scaled for other values of B_{VM}, e.g., if $B_{VM} = 150\,kHz$, the VM noise error is lower by $10^{1/2}$.

For this particular example, SPM appears to be the best choice only for a narrow region near $\beta = 10^{-11}$. For $\beta > 3\text{x}10^{-11}$, the VM errors are lower, and for $\beta < 3\text{x}10^{-12}$, the number of SPM spikes per observation time is less than 3. This eliminates SPM because the noise spikes would contaminate the estimate. The SPM error is dominated by the random error component while the VM error is dominated by the additive noise component.

It must be remembered that the SPM measurement is biased low, while the VM measurement is unbiased; that the SPM and VM analyses are only valid in SPM and VM regimes, respectively; that the operational value of B_{VM} may be much lower than B_{SPM}; and that systematic errors have not been addressed.

The two methods of operation (VM and SPM) should be compared with separate optimization of parameters, and not necessarily equal focal settings or detection bandwidths, if the main goal is accurate measurement of β. However, if information about $n(\sigma)$ is also desired, then a tightly focused geometry is required, and the VM-SPM comparison should be done with the same system parameters. Without this theory it is not clear whether focused VM operation, which violates the Gaussian statistics assumption (many particles), is better or worse than collimated VM operation.

7. TRADE-OFFS

7.1 VM Trade-offs

The shot noise and random error (speckle statistics) contributions to total error for ideal VM operation are very small. The main sources of error are systematic. A focused beam has a factor of 2 more system gain than a collimated beam. However, a focused beam senses a much smaller volume, may not have "speckle statistics," is more difficult to align, and may change or destroy the aerosol particles. Since systematic errors are likely dominant, a factor of 2 loss in gain with a collimated beam could be worth the decrease in systematic errors. Improving beam quality at the expense of transmitted power may improve overall performance.

7.2 SPM Trade-offs

SPM operation is more complex and difficult to analyze. For useful operation, the system parameters must be chosen to provide single particle events over the specified range of β. This requires a focused system where beam alignment may be difficult. There are many trade-offs between beam geometry and system gain. The transmitted beam can be focused and the local oscillator beam collimated. This provides a larger range of SPM operation at the expense of system gain. A tightly focused system also requires higher bandwidth to observe the narrow brief pulses. This sacrifices SNR. Improving beam quality at the expense of transmitted power may improve overall performance.

8. FUTURE WORK

8.1 VM

1) Investigate temporal decorrelation time (we assumed 1 μs).
2) Investigate systematic errors:
   a) Beam geometry (collimated vs focused)
   b) Specifications on sensing volume and range
   c) Signal processing (rms detector, peak detector, power detector, linearity, background subtraction, drift)
3) $\frac{\Delta\beta(random)}{\beta}$ with single particle behavior. Are there parameter regimes where VM estimates in the SPM regime have better accuracy compared to speckle statistics (many scattering particles) i.e., collimated vs focused?
4) Improved signal processing. What is the IF signal bandwidth (instantaneous and IF drift)?
5) Is there an automatic gain control and what are the specifications?

8.2 SPM

1) Need reliable $n(\sigma)$ models.
2) Calculate $\frac{\Delta\beta(noise)}{\beta}$ and $\frac{\Delta\beta(random)}{\beta}$ for general parameters (beam size, focus, alignment, beam offset).
3) Calculate average number of spikes $<N_{spike}>$ for general system.
4) Calculate distribution of spike amplitude and width.
5) Determine SPM operating regions.

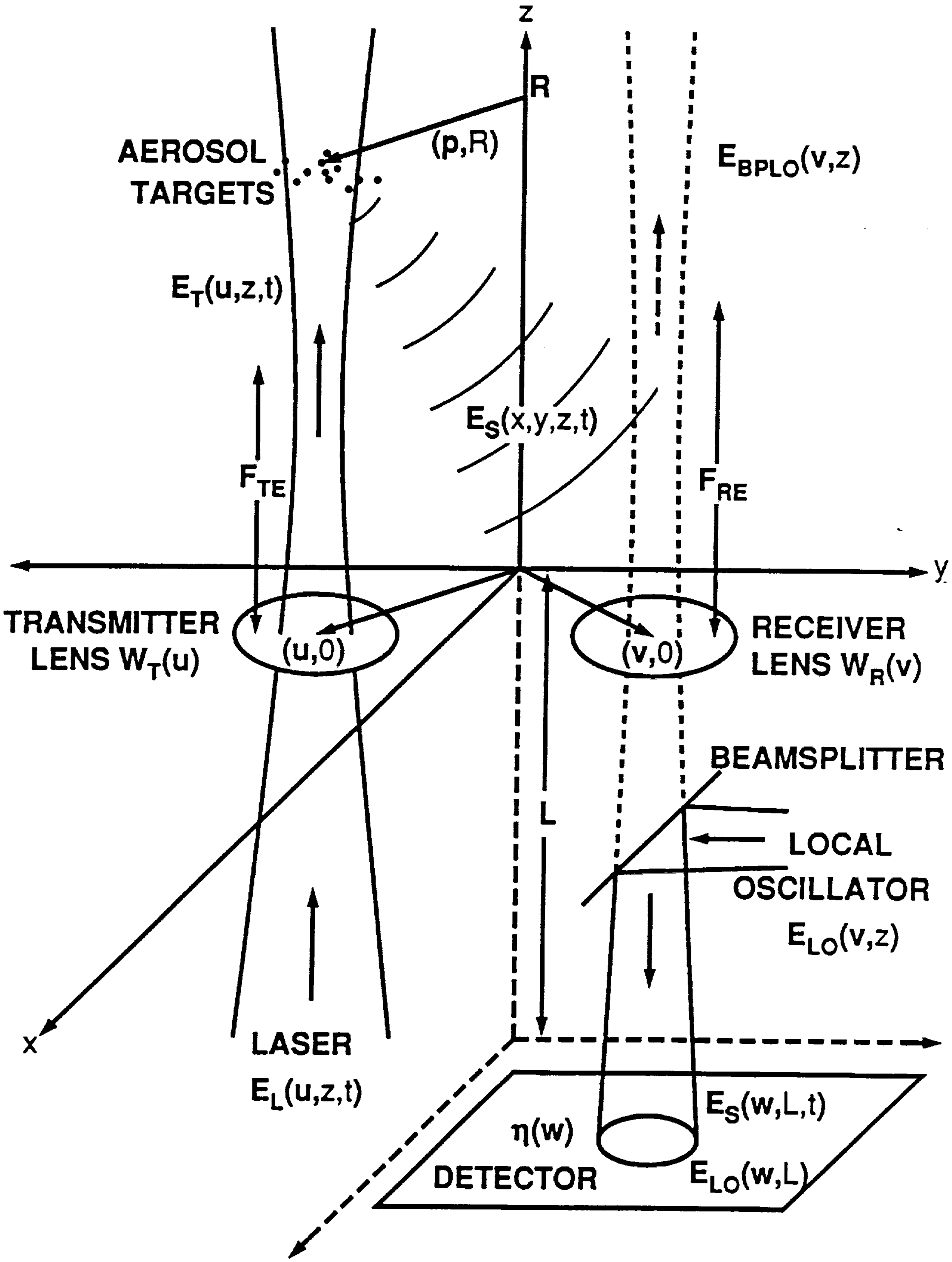

Figure 1. Geometry for a coherent detection laser radar system. An actual system would have overlap of the XMTR and BPLO beams at the target.

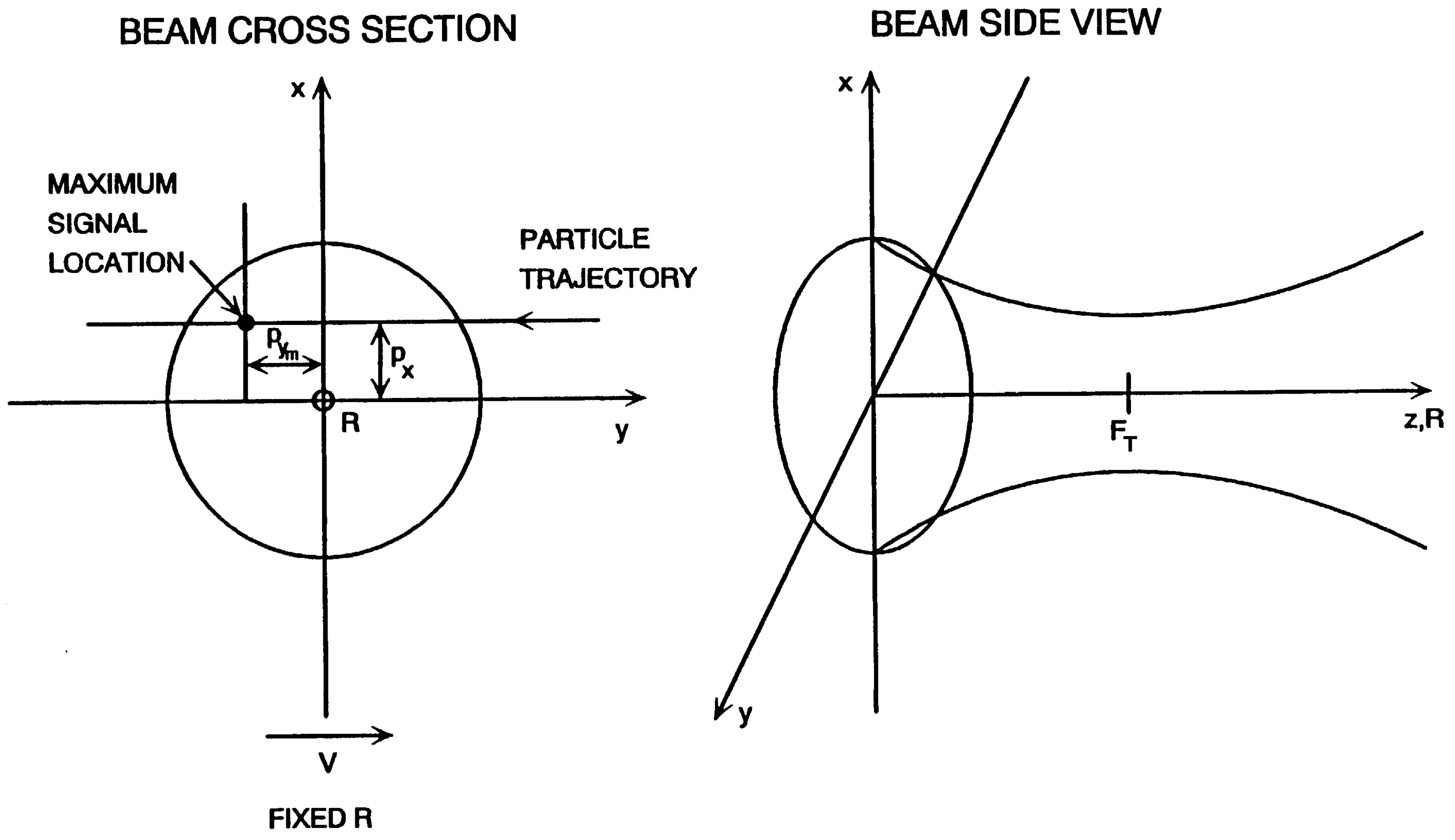

Figure 2. Geometry of single particle mode (SPM) operation.

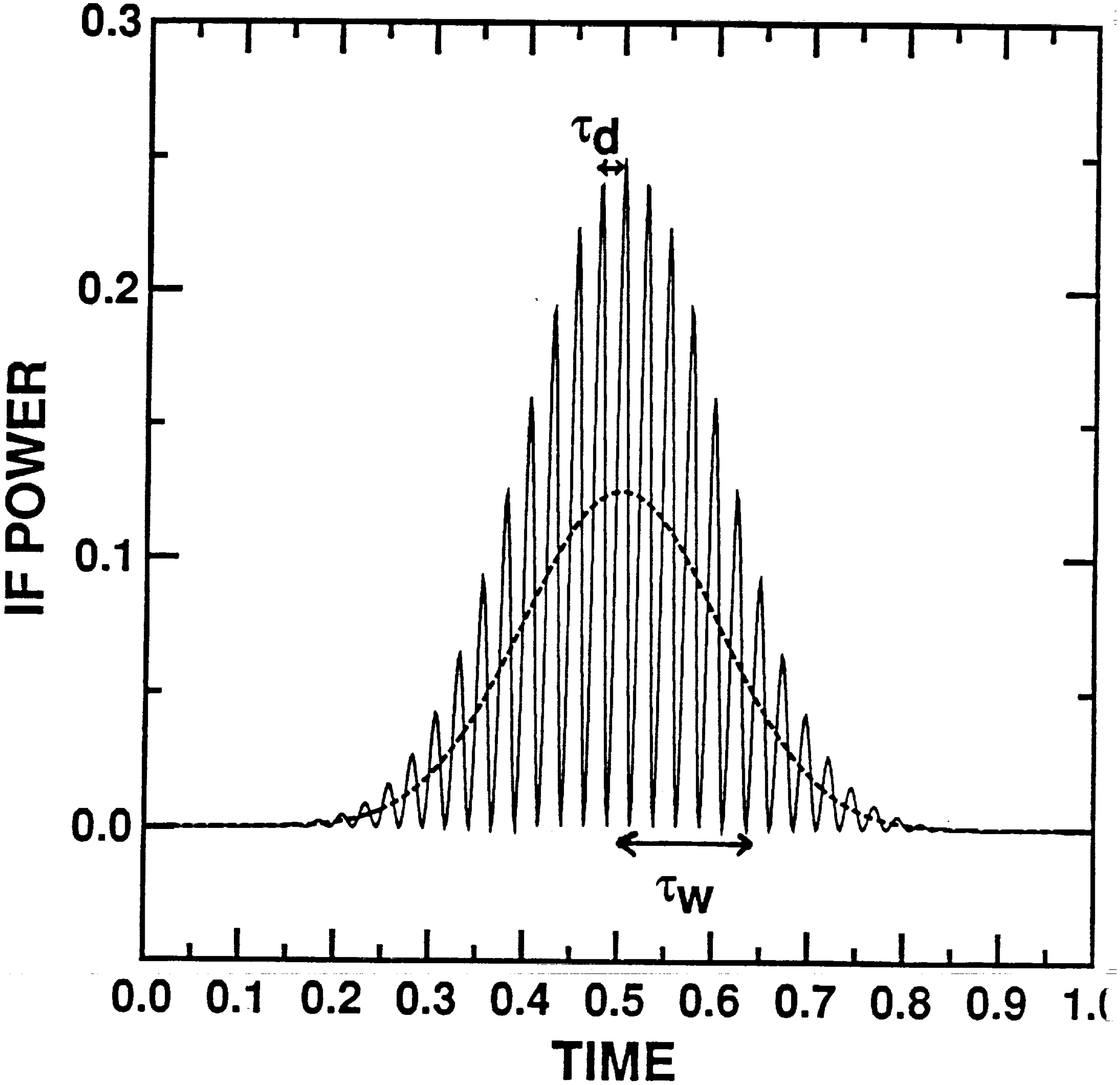

Figure 3. Simulation of IF power (the square of the IF voltage) with no noise for a moving point scatterer through a Gaussian transmitted beam. The average IF power (SPM lidar signal) is indicated by the dashed line.

Figure 4.

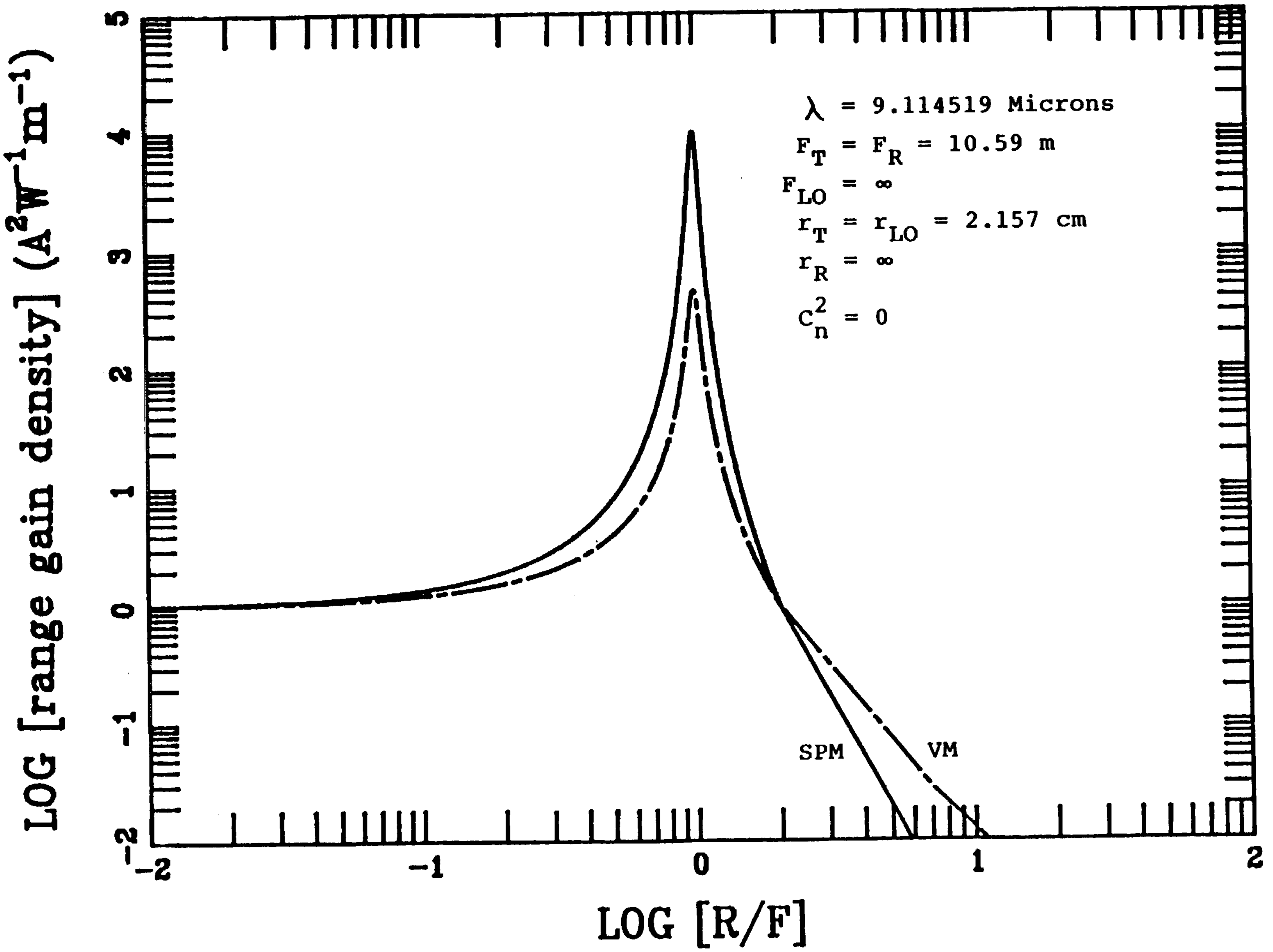

λ = 9.114519 Microns
F_T = F_R = 10.59 m
F_{LO} = ∞
r_T = r_{LO} = 2.157 cm
r_R = ∞
C_n^2 = 0
SPM
VM
LOG [range gain density] ($A^2W^{-1}m^{-1}$)
5
4
3
2
1
0
−1
−2
−2
−1
0
1
2
LOG [R/F]

Figure 5.

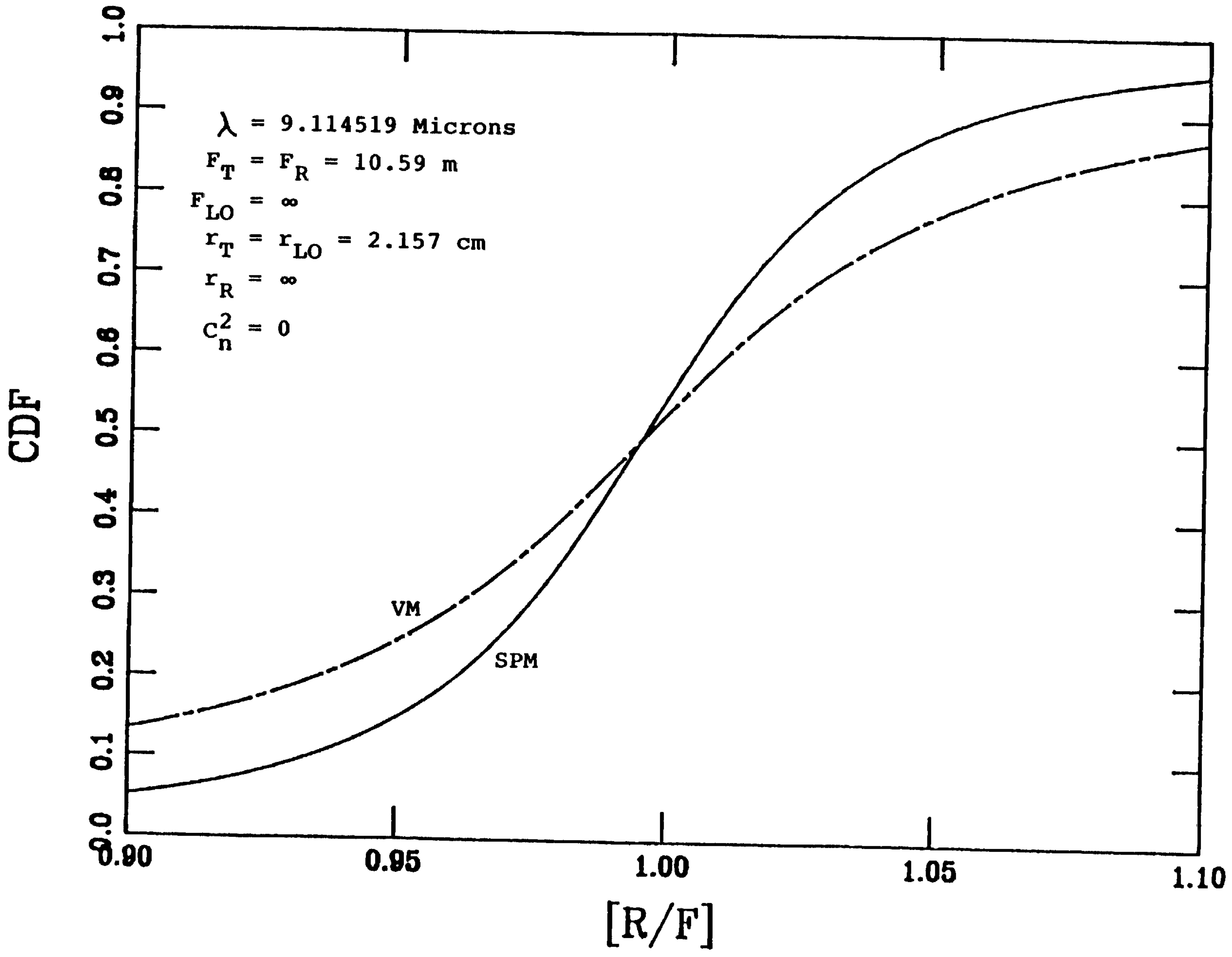

λ = 9.114519 Microns
$F_T = F_R$ = 10.59 m
$F_{LO} = \infty$
$r_T = r_{LO}$ = 2.157 cm
$r_R = \infty$
$C_n^2 = 0$
VM
SPM
CDF
0.0
0.1
0.2
0.3
0.4
0.5
0.6
0.7
0.8
0.9
1.0
0.90
0.95
1.00
1.05
1.10
[R/F]

Figure 6.

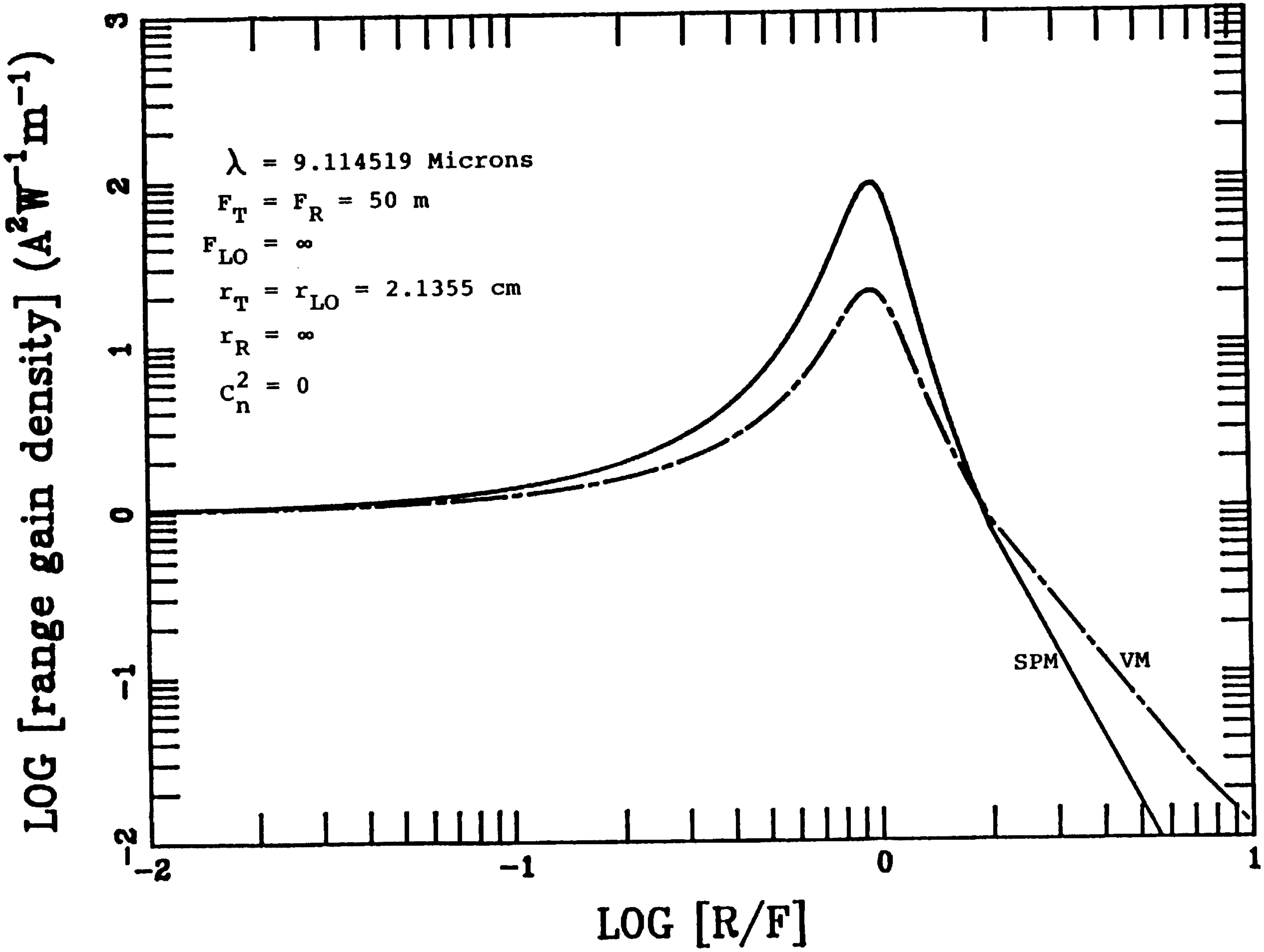
λ = 9.114519 Microns
$F_T = F_R = 50$ m
$F_{LO} = \infty$
$r_T = r_{LO} = 2.1355$ cm
$r_R = \infty$
$C_n^2 = 0$
SPM
VM
3
2
1
0
−1
−2
−2
−1
0
1
LOG [range gain density] $(A^2W^{-1}m^{-1})$
LOG [R/F]

Figure 7.

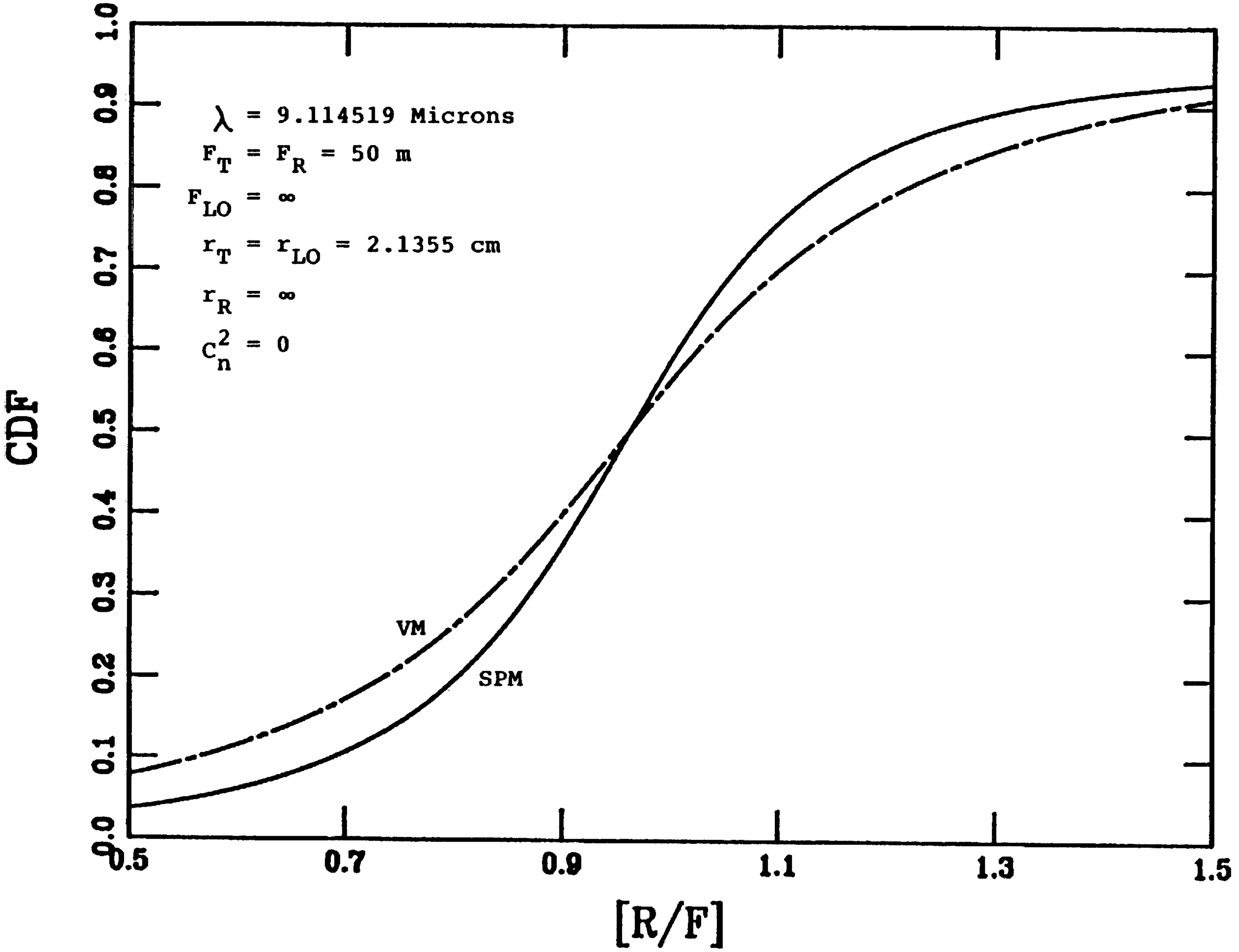
λ = 9.114519 Microns
$F_T = F_R$ = 50 m
$F_{LO} = \infty$
$r_T = r_{LO}$ = 2.1355 cm
$r_R = \infty$
$C_n^2 = 0$
VM
SPM
CDF
0.0
0.1
0.2
0.3
0.4
0.5
0.6
0.7
0.8
0.9
1.0
0.5
0.7
0.9
1.1
1.3
1.5
[R/F]

Figure 8.

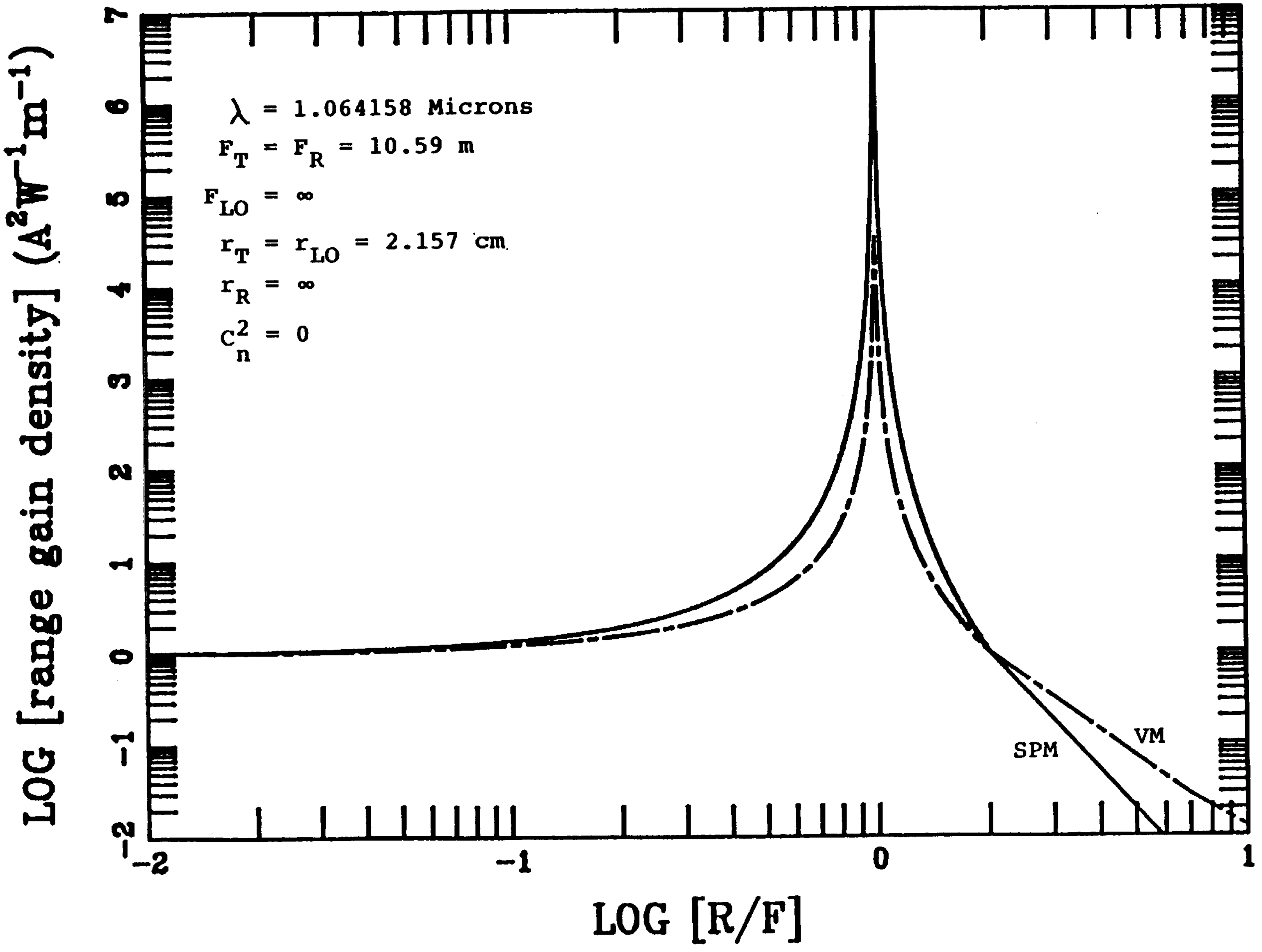
λ = 1.064158 Microns
$F_T = F_R = 10.59$ m
$F_{LO} = \infty$
$r_T = r_{LO} = 2.157$ cm
$r_R = \infty$
$C_n^2 = 0$
SPM
VM
LOG [range gain density] $(A^2W^{-1}m^{-1})$
7
6
5
4
3
2
1
0
−1
−2
−2
−1
0
1
LOG [R/F]

Figure 9.

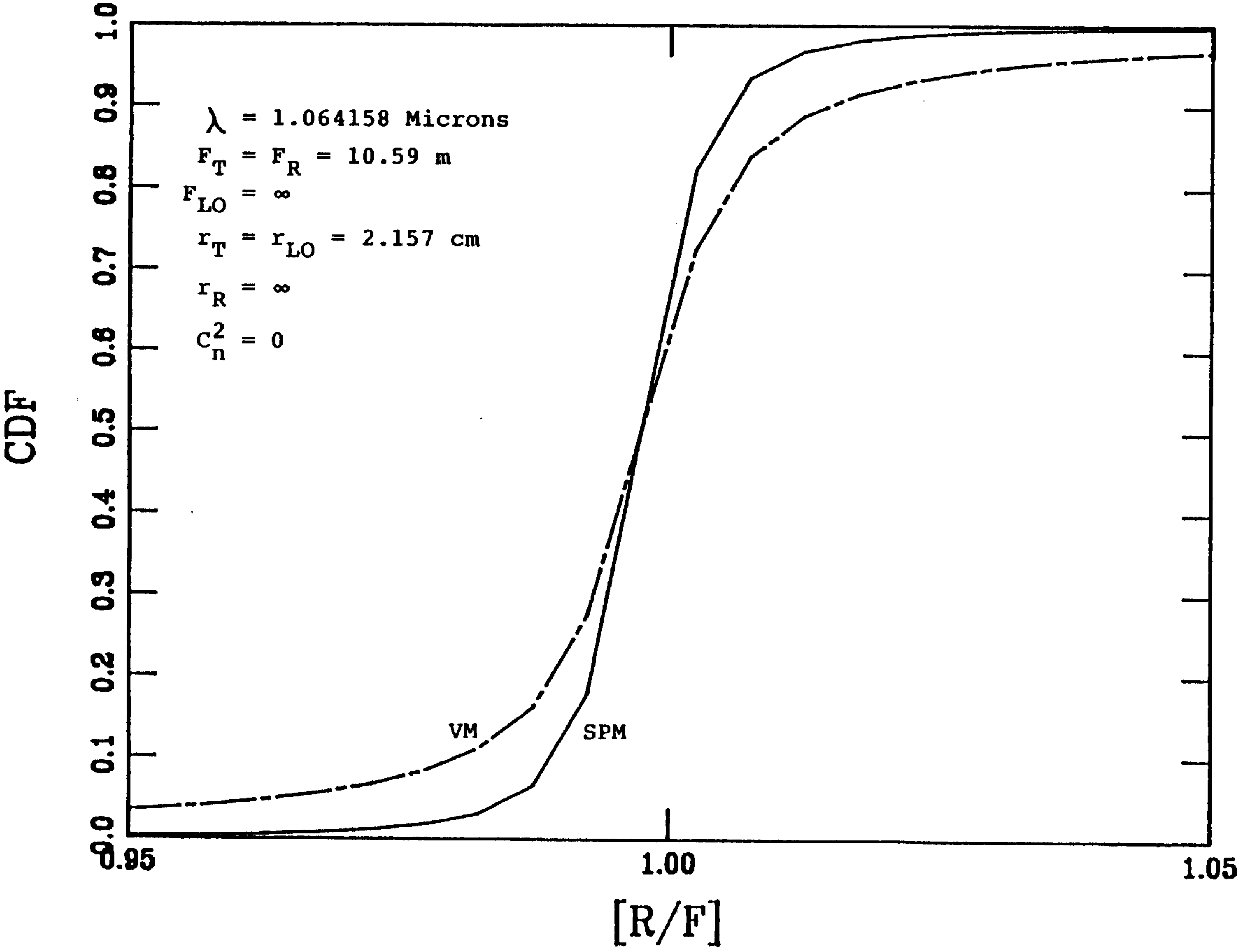
λ = 1.064158 Microns
$F_T = F_R = 10.59$ m
$F_{LO} = \infty$
$r_T = r_{LO} = 2.157$ cm
$r_R = \infty$
$C_n^2 = 0$
VM
SPM
CDF
0.0
0.1
0.2
0.3
0.4
0.5
0.6
0.7
0.8
0.9
1.0
0.95
1.00
1.05
[R/F]

Figure 10.

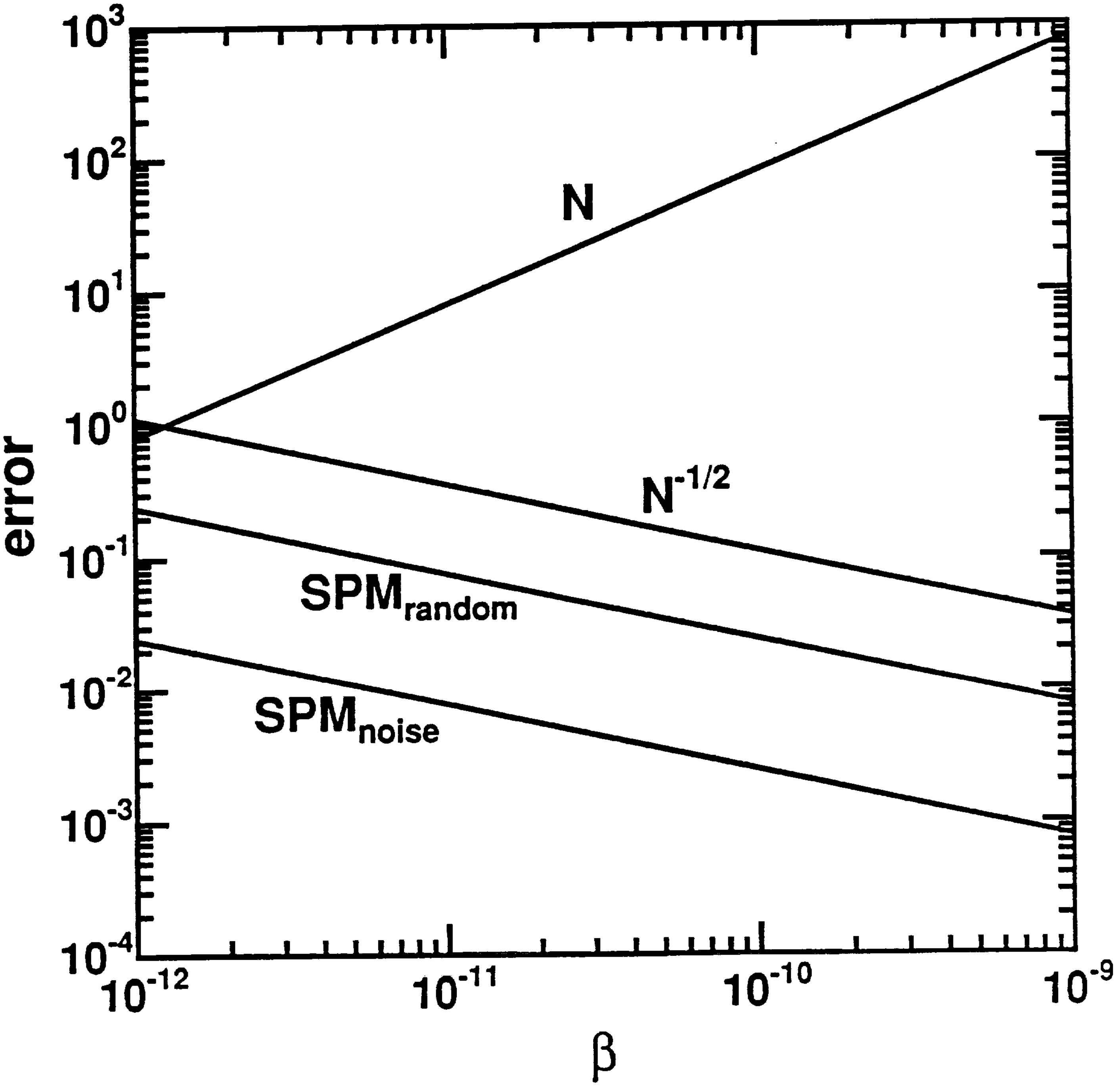

Figure 10. Error in β vs β for the MSFC lidar in SPM. N is the average number of spikes observed.

Figure 11.

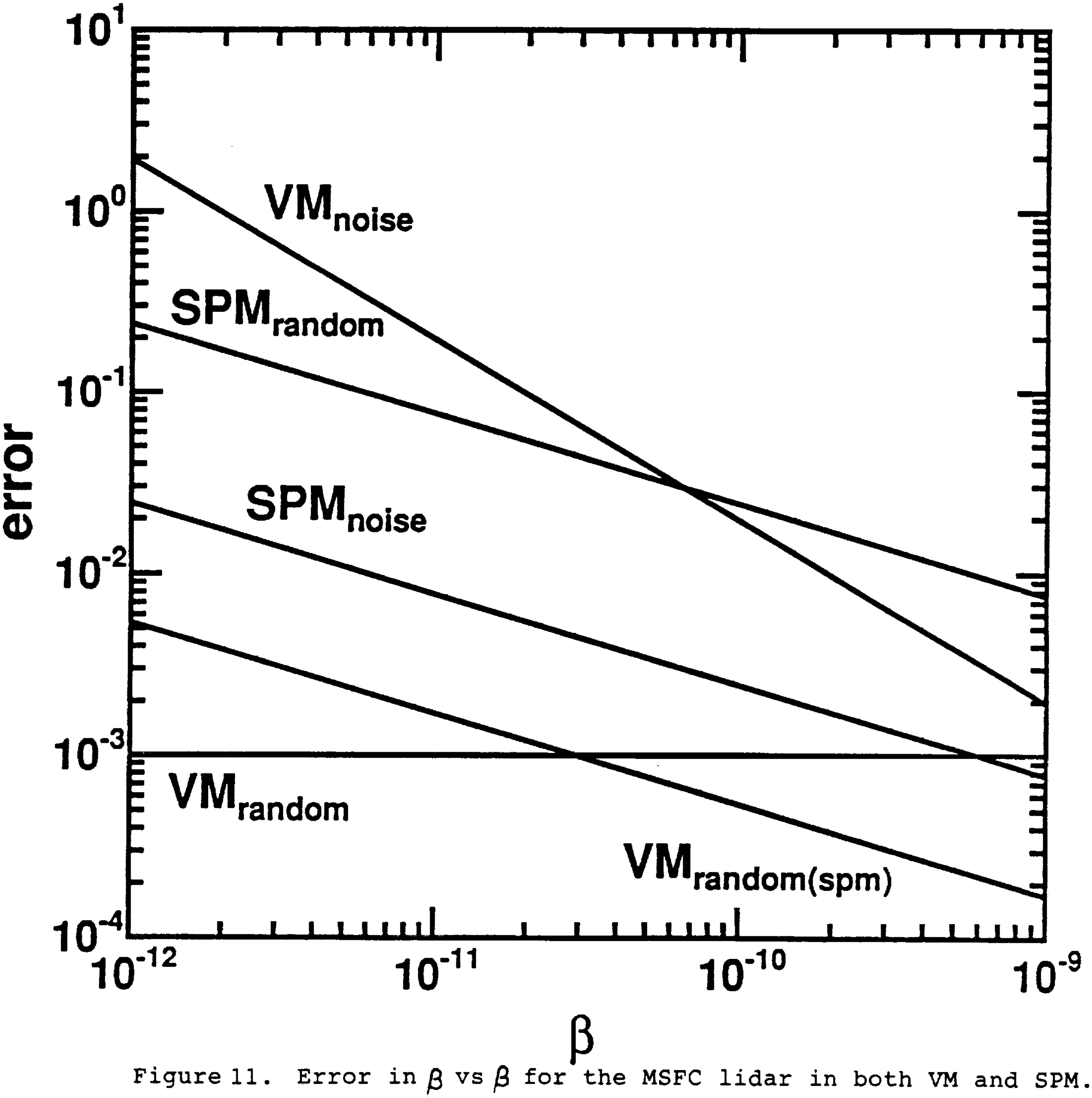

Figure 11. Error in β vs β for the MSFC lidar in both VM and SPM.

9.0 DEVELOPMENT OF A Ho:YAG SOLID-STATE PULSED LIDAR

Spatially resolved, accurate measurements of atmospheric wind velocity are needed for many civilian, military, and commercial applications where the state-of-the atmosphere is important. Examples include weather forecasting [National Academy of Sciences (1980)], and the premonitory detection of low altitude wind shear by aircraft [R. Targ et al. (1990)]. This section documents the results of work performed during this effort toward the development of a pulsed, coherent, Tm,Ho:YAG, 2 μm laser radar system capable of making range-resolved measurement of atmospheric wind and aerosol backscatter profiles.

Until recently, the mature CO_2 laser has been the almost exclusive type of transmitter employed in coherent laser radar (CLR) systems. The CO_2 laser and CLR technology has developed to the point where several CLR systems have been built for wind velocity and/or aerosol backscatter measurements. [see e.g., Hardesty, et al. (1988) and Menzies et al. (1984)]. The CO_2-based LAWS instrument is currently being designed for space-based measurement of global wind fields [Beranek et al. (1989)]. Several issues relating to frequency stability, lifetime, pulse frequency chirp, and efficiency remain to be solved or demonstrated before CO_2 CLR transmitters can be space qualified [Hardesty et al. (1988)].

Solid-state laser technology is a rapidly advancing competing technology. With the advent of high efficiency, high power, semiconductor laser diodes as pump sources for solid-state lasers, all-solid-state CLR transmitters can be envisioned which have the advantages of low mass, small size, long shelf and operating lifetime, and the absence of consumables. In applications where atmospheric turbulence isn't too severe, the shorter wavelengths of solid-state lasers (0.7 - 3.0 μm) offer superior overall performance compared to the longer wavelengths of CO_2 lasers (9-11 μm). In addition, the continuous-tuning ranges of solid-state lasers are typically large enough to allow very low atmospheric extinction and/or multiwavelength differential absorption lidar (DIAL) measurements.

A 1.06-μm CLR system using Nd:YAG lasers was recently developed by Coherent Technologies, Inc. [Kavaya et al. (1989)]. Velocity and range measurements from hard targets and atmospheric aerosol particles have been routinely demonstrated using this system at a remote site near Boulder, CO [Henderson et al. (1990A)]. One of the chief deficiencies in the 1.06-μm Nd:YAG technology is the lack of eye safety.

The advances made in eyesafe 2 μm solid-state lasers during the mid-1980s led CTI to begin, under funding from the U.S. Air Force-Space Division, the development of the first eyesafe solid-state CLR system in 1987. Details of the 2-μm CLR development are included in the Air Force final report [Henderson et al. (1990B)]. An overview of the 2-μm CLR is given in Section 9.1.

A breadboard master oscillator (MO) was developed under the Air Force funding and was utilized to demonstrate, for the first time, single-longitudinal-mode operation of a Tm,Ho:YAG laser [see Appendix E]. This breadboard was also used to "zero in" on a MO design which was functional. The NASA/MSFC funds provided during this effort were used to design, construct and test a "hardened" version of this MO which exhibits much better long and short-term frequency stability. This hardened MO is described in detail in Section 9.2.

With the aid of funding from the Wright Research and Development Center (Wright-Patterson AFB), the coherent 2-μm CLR system was recently relocated to the Table Mountain field test site located ~ 10 miles north of Boulder, CO. In Section 9.3, we describe preliminary field measurement results using the CLR.

9.1 Overview of the 2-μm CLR System

This section contains an overview of the Tm,Ho:YAG coherent laser radar system. More detail about the master oscillator developed during this effort is provided in Section 9.2. The 2-μm CLR system was primarily designed for measurements of atmospheric water vapor.

A diagram illustrating the CTI Tm,Ho:YAG CLR system is shown in Figure 12. The MO is a continuous-wave (CW) diode laser pumped single-longitudinal-mode (SLM) Tm,Ho:YAG laser. This oscillator, which we designed and built, utilizes a linear cavity with an intracavity Brewster plate for polarization control, and two solid fused silica etalons for frequency control. With the MO laser crystal thermo-electrically cooled to ~ 230 K, the SLM output power is ~ 50 mW near 2090 and 2097 nm. The wavelength can be tuned continuously between 2086 and 2100 nm. By changing the reflectivity of the output coupler, tuning near 2121 nm has also been achieved. The linewidth and short-term frequency jitter (seconds) of the MO is < 1 MHz, and the long-term frequency drift (~ 1 day) is ~ 300 MHz peak-to-peak.

The output of the MO is first passed through a Faraday isolator which isolates the MO from the rest of the system. Additional isolation from the slave oscillator is provided by a 98% reflector. A portion of the reflected power serves as the local oscillator (LO) beam. The MO power that is transmitted by the 98% reflector is frequency shifted by 27 MHz using an acousto-optic frequency shifter (AOM in Figure 12). The frequency-shifted beam is then mode-matched and injected into the Q-switched slave oscillator. The flashlamp-pumped Cr,Tm,Ho:YAG laser crystal in the slave oscillator is water cooled and operates at approximately room temperature. The injection-seeded slave oscillator is capable of producing 50 mJ, ~ 150 ns, SLM, TEM_{00} pulses at 3 Hz. The required frequency match between the slave oscillator and the MO is maintained by an automatic servo system which controls the slave cavity length using an end mirror mounted on a piezo-electric translator (PZT). More detail about the performance of the injection-seeded transmitter is provided in Appendix F.

The SLM output of the slave oscillator is incident upon an eccentric-pupil Dall-Kirkham telescope which expands the beam to ~ 20 cm and transmits the pulse into the atmosphere. Backscattered radiation from the atmosphere is collected by the telescope and mixed with the LO beam using a beam splitter whose reflectivity is ~ 15%. The coherently-mixed signal and LO beams are then focused onto a 100 μm-diameter room-temperature extended-wavelength InGaAs detector. The quantum efficiency of this detector at 2.1 μm was measured to be 0.69 electrons/photon. The heterodyne signal from the detector, which is in the bandwidth between ~ 5 and 50 MHz (target velocities from ~ 23 m/s to ~ -24 m/s), is amplified, filtered, then digitized every 10 ns using one channel of a LeCroy 9400 dual-channel digital storage oscilloscope (DSO). The digital data is then transferred to a DEC MicroVax II digital computer using a general purpose interface bus (GPIB). The raw data is then processed using very flexible processing software, to extract Doppler velocity (first moment), velocity width (second moment), and backscatter (zero moment) information.

The CLR is constructed on a 4′ x 8′ Newport optical table. The laser transmitter consisting of the MO, Faraday isolator, AOM, and slave oscillator, is mounted on a separate 1′ x 5′ breadboard. Figure 13 consists of two photographs showing different views of the complete laser transmitter. The scale in the photos is given by the 1" hole pattern of the 1′ x 5′ breadboard.

9.2 Frequency Stabilized Master Oscillator

As described in Section 9.0, a breadboard oscillator was used to demonstrate that SLM oscillation could be achieved. This hardware allowed us to try many different resonator configurations to arrive at an operating condition which performed best. The performance we were able to achieve with this breadboard hardware is described in Appendix E and in the final report to the Air Force [Henderson et al. (1990B)]. A photograph of the breadboard hardware is shown on the top half of Figure 14.

The performance data collected with the breadboard-level oscillator was used to design and construct a highly stabilized SLM laser (Figure 14 bottom). In addition to mechanical and thermal improvements, a significant change in the basic cavity design (as compared to the design presented in Appendix E) was incorporated as a result of earlier tests. The resonator configuration chosen for the stabilized laser is shown in Figure 15. The intracavity lens L_1 allows for a "collimated" leg inside the cavity between the lens and the output coupler M_2, where the Brewster plate polarizer P and tilted etalons E_1 and E_2 could be installed. This effectively reduces the walkoff loss experienced in those elements, which reduces overall circulating intracavity losses and permits higher tilt angles of the etalons before excessive loss is incurred. This in turn assures a very clean TEM_{00} spatial profile in the output beam, as all intracavity optics (and their inevitable surface reflections) are capable of being tilted well off of the beam axis. This technique also reduces output beam astigmatism due to the tilted Brewster polarizer to a negligible level. Very high spatial beam quality in the LO source is essential for maximum heterodyne efficiency, and could not be compromised in the laser design. Details of the resonator optics follow.

The flat resonator mirror M_1 is a high reflector at wavelengths near 2100 nm and transmits ~ 88% of the diode laser pump light near 785 nm. Resonator mirror M_2 is also flat and serves as the output coupler, transmitting ~ 2.5% of the laser light near 2100 nm. The cavity mirrors M_1 and M_2 are separated by ~ 117 mm. The intracavity lens L_1 has a focal length of ~ 75 mm, is located ~ 75 mm from M_1, and is AR-coated at 2100 nm. The uncoated solid-fused silica etalon E_2 is 0.09 mm thick. E_1 is a 0.5 mm thick solid-fused silica etalon with the surfaces coated for 18% power reflectivity near 2100 nm. The Tm:Ho:YAG laser rod is 4 mm in diameter and 4 mm long. The end faces of the crystal are polished flat and AR-coated for wavelength near 2100 nm. The AR-coating reflects < 0.5% of the 785 nm pump light. The laser rod is cooled to ~ -40^0 C using a 3-stage thermo-electric cooler.

A great deal of effort was expended on the opto-mechanical, thermal, and acoustical engineering issues associated with producing a very frequency-stable oscillator. To assure absolute frequency jitter of less than 1 MHz out of 1.4×10^{14} Hz (i.e., 2.1 μm wavelength), requires dimensional stability of the resonator mirror spacing on the order of ~ 8 Å (for the cavity length of ~ 117 mm). In addition, it is desirable to limit long-term frequency drift due to thermal and/or pressure changes in the environment to a very low level. Negligible frequency drift must be achieved in the MO/LO both to assure that the effects of atmospheric absorption remain constant during laser radar operation, and to simplify the frequency-locking requirements in the injection-seeding subsystem.

For these reasons, we designed and built a box-like resonator structure made from super-invar, an ultra-low thermal expansion steel alloy, shown in Figure 14 (bottom). Both resonator mirrors are located against solid shoulders milled into either end of the common structure, assuring immunity against mechanical vibration and, to first order, thermal changes in the environment. The entire super-invar body is temperature stabilized using a small closed-loop constant-temperature water circulator. This arrangement also permits cooling and thermal stabilization of the thermoelectric (TE) heat pump module used to cool the laser rod. This TE cooler module is powered by a very low noise (a few mV p-p) DC power supply, further assuring that thermally-induced refractive index fluctuations in the laser rod are held to a minimum.

To provide isolation from acoustic vibrations and pressure changes in the environment, the entire resonator body structure is hermetically-sealed and filled with dry nitrogen. The nitrogen backfill also prevents frost buildup on the YAG rod, which is typically operated at -40^0 C. The stabilized laser's output power and frequency tuning, as observed with the quarter-meter monochromator and complementary spectrum analyzers, produced data very similar to that described in Appendix E for the breadboard-level oscillator.

As expected, the engineering refinements described above have resulted in very low short-term jitter and drift in the laser output frequency. By optimizing the finesse of a scanning confocal spectrum analyzer (free spectral range of 300 MHz), it was possible to resolve and characterize sub-megahertz frequency fluctuations in the stabilized laser output. Figure 16 shows typical frequency jitter and drift magnitudes for one-second and five-second operating periods. The horizontal dimension of the oscilloscope traces represents 1.13 MHz per major division (200 μs); frequency jitter is observed as a horizontal movement of the interferometer transmission profile over the scope camera exposure time. The width of the transmission profile is due to the resolution of the 300 MHz interferometer. Typical jitter and drift values observed were less than 0.5 MHz peak-to-peak for up to 5 second periods, and correspondingly much less for the short-term (10's of μsec) round trip times of interest for atmospheric coherent laser radar. Long-term frequency drift has been found to be ~ 300 MHz/day peak-to-peak in this laser, resulting in extremely stable, mode-hop-free SLM operation. It should also be noted that jitter and drift recorded in these photographs are contributed to further by the scanning interferometer diagnostic itself. Finally, the photographs were taken with the laser and interferometer mounted on a standard optical table which was <u>not</u> vibration isolated. The optical table was located inside a relatively noisy laboratory on the third floor of an office building.

9.3 Preliminary Field Measurement Results

The system was very recently moved and integrated at our remote field test site ~ 10 miles north of Boulder, CO (Building T-1 at Table Mountain - a DOC facility). Only a small amount of CLR data has been taken at this time. We include here examples showing some of the preliminary results which exhibit the fundamental operation of the CLR system.

For all of the examples shown below, the transmitted pulse energy of the CLR was ~ 20 mJ. The CLR was running at a PRF of 3.2 Hz. A LeCroy 9400 DSO was used to capture the temporal data shown in the following figures. Figure 17 shows the temporal profile of the 20 mJ pulses. Note that the full-width at half-maximum (FWHM) duration of the SLM pulses is ~ 220 ns. Figure 18 shows the heterodyne signal due to the single-shot CLR return from a mountainside located ~ 14.9 km down range. The telescope was focused at infinity for this data taken on October 4, 1990. Figure 19 shows an example of a return from clouds located ~ 13.8 km from the CLR taken on October 4, 1990. When this single-shot data was taken, the telescope was focused at 2 km.

Figure 20 plots the power spectrum of the return from a cloud located approximately 10 km from the CLR. A 256-pt. fast-Fourier-transform (FFT) centered at 9.89 km was used to compute the power spectrum. Note that the radial velocity of the cloud is ~ 7 m/s toward the laser radar. Figure 21 gives an example of a wind measurement made on October 7, 1990. The telescope was focused at 2 km and the beam was aimed to the north at ~ +8° from horizontal. Figure 21 is the plot of the power spectrum of aerosol return in a thin slab of atmosphere centered at 3.75 km. A 256-pt. FFT was used to generate the spectrum. Note that the radial wind velocity is ~ 8 m/s toward the CLR.

To date, atmospheric wind velocity has successfully been measured to horizontal ranges exceeding 20 km on hazy days and 5 km on very clear days. When the lidar beam is pointed vertically, the highest altitudes above ground level for which aerosol return has been observed to date is ~ 4 km. Figure 22 shows the A-scope display of aerosol return signal for 111 shots averaged. For this data taken on 24 Oct. 1990, the lidar was aimed approximately horizontal and focused at ∞. The receiver bandwidth was ~ 41 MHz. The A-scope display is the result of squaring the IF aerosol signal from each shot and averaging 111 consecutive shots. The lower trace of Figure 22 defines the background noise and is the result of averaging 111 shots with the telescope output blocked. When narrowband FFT processing is utilized, the signal-to-noise levels shown in Figure 22 are sufficient for wind measurements beyond 20 km (> 130 μs).

Figure 12.

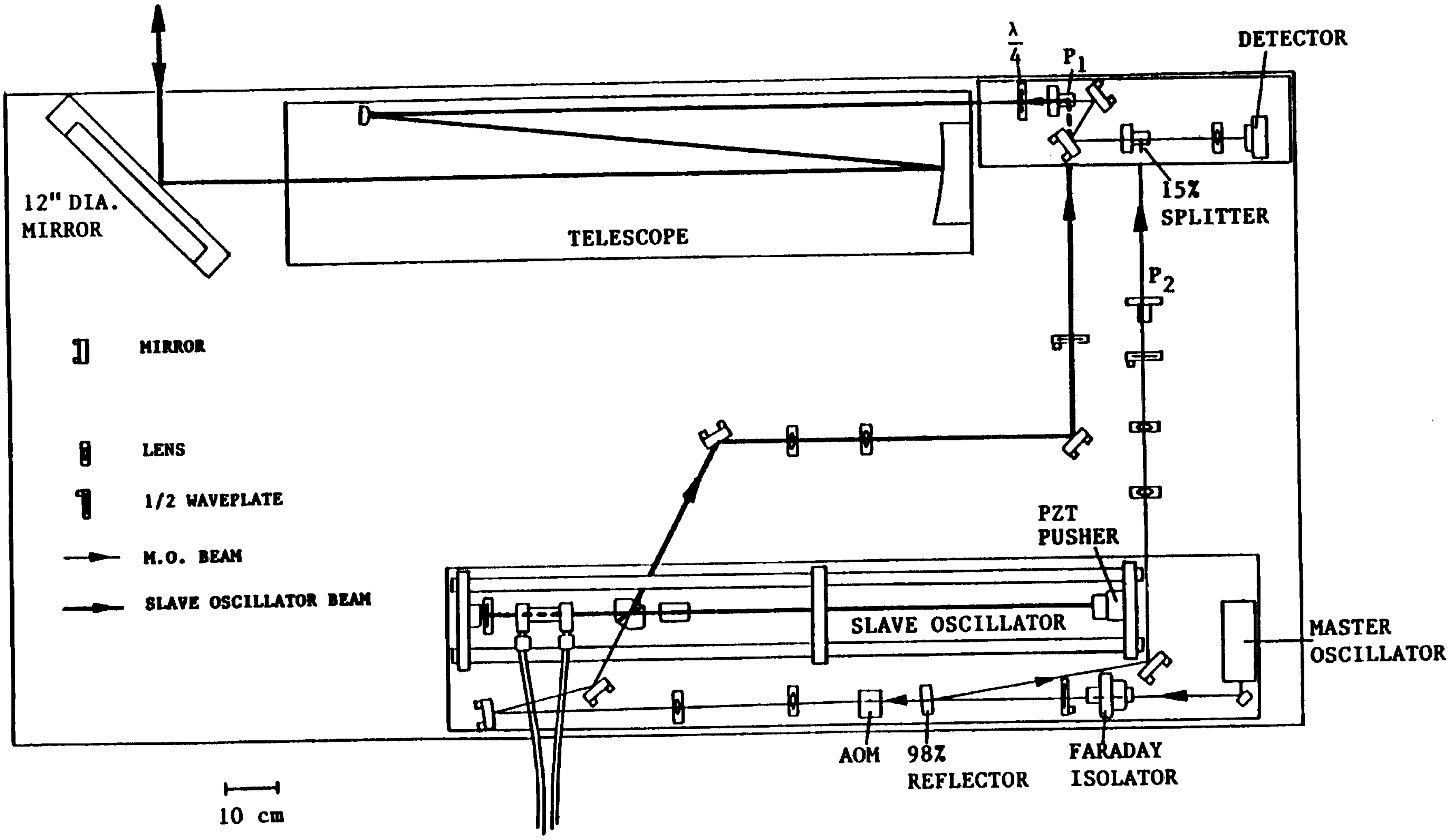

Figure 12. Plan view diagram of the 2 μm Tm,Ho:YAG coherent laser radar system.

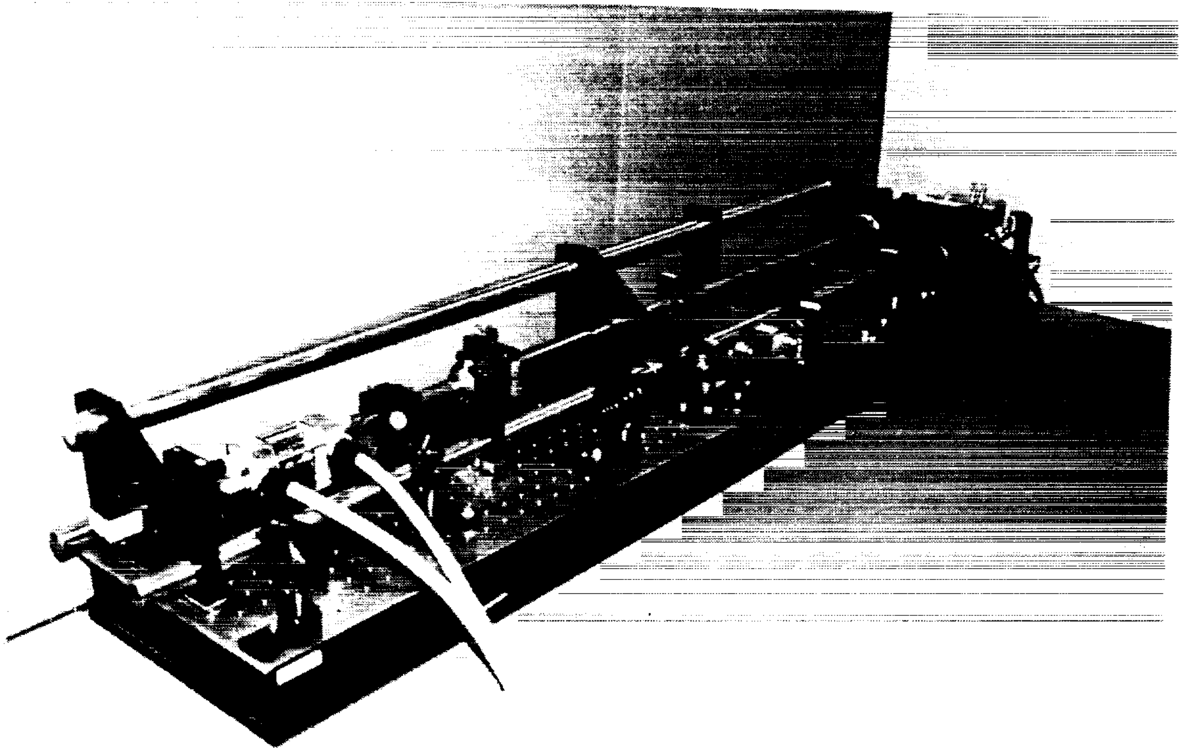

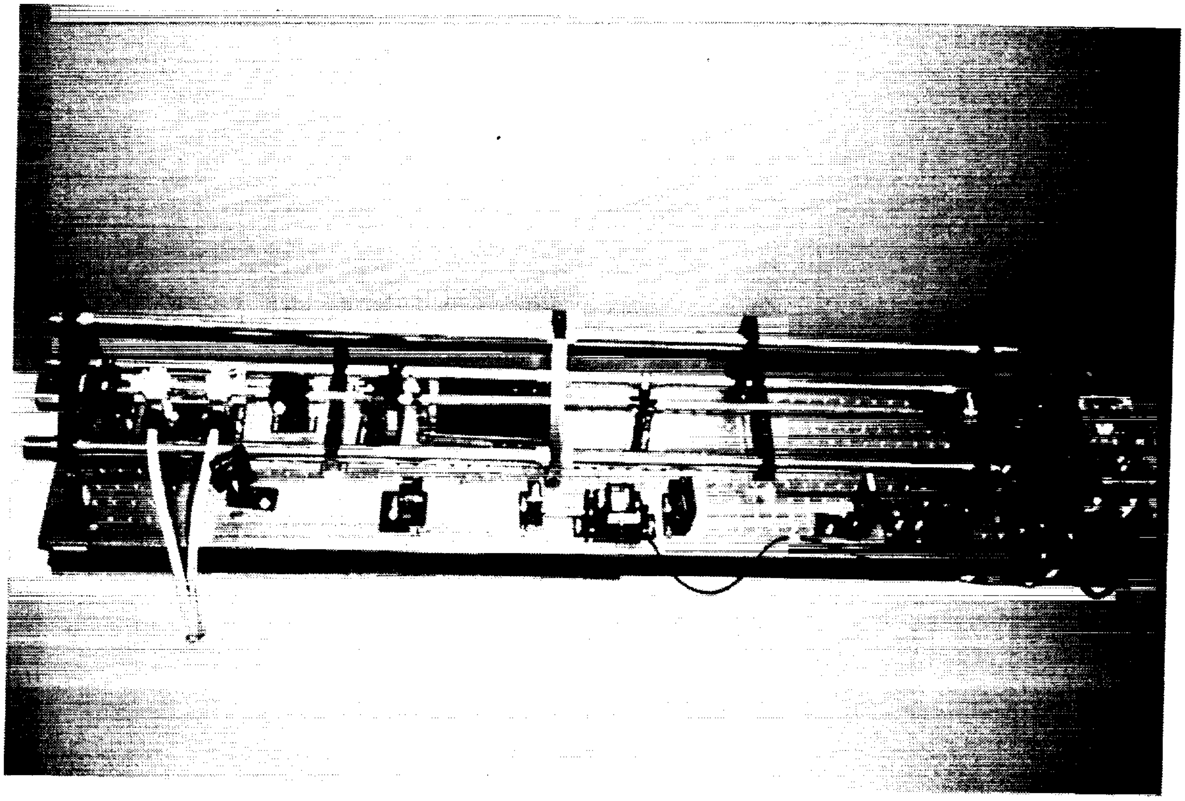

Figure 13. Injection-seeded Cr,Tm,Ho:YAG transmitter, comprised of master oscillator, slave oscillator, and 27 MHz AO modulator.

ORIGINAL PAGE
BLACK AND WHITE PHOTOGRAPH

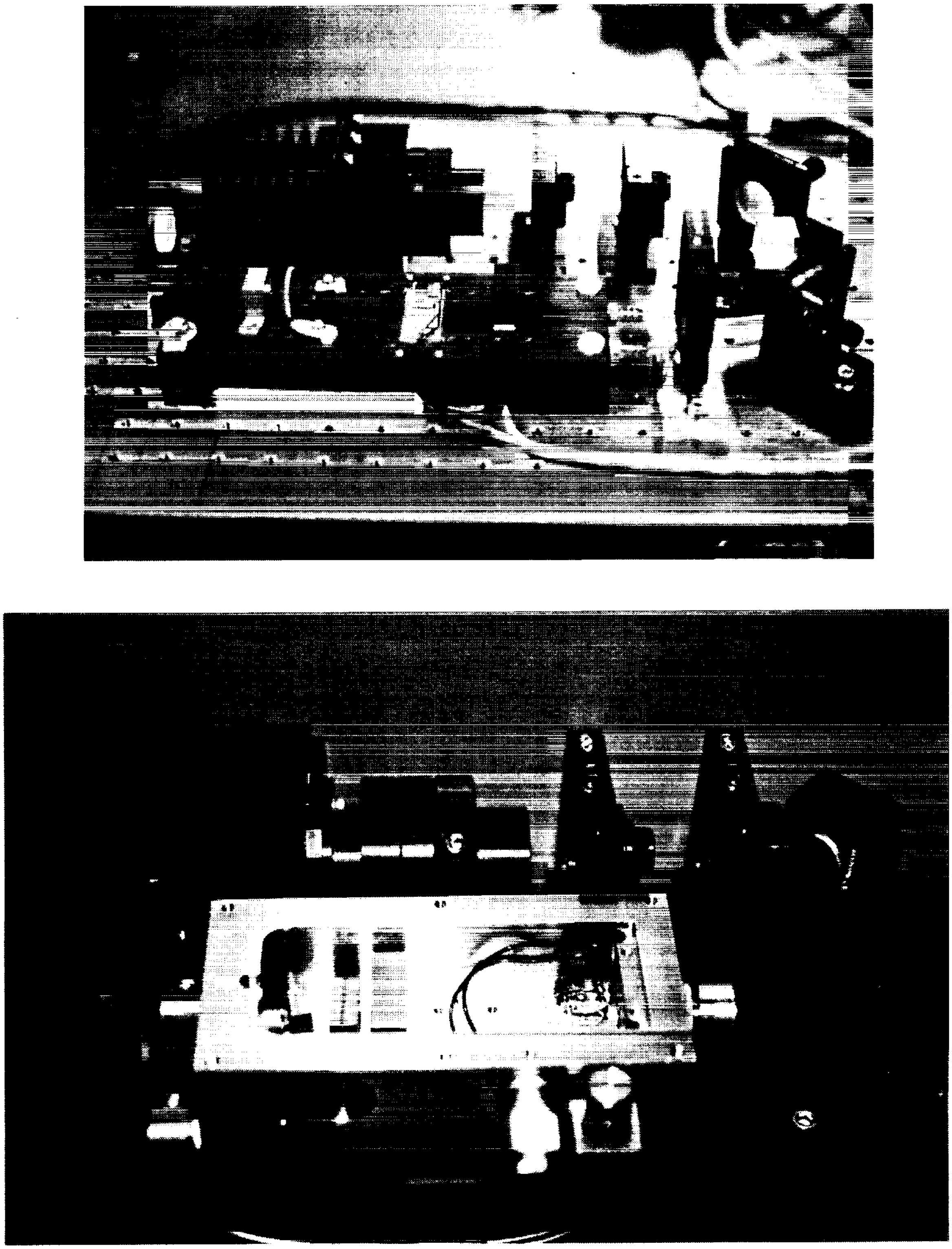

Figure 14. CW Master Oscillator. Top: Breadboard-level hardware configuration. Bottom: Final stabilized oscillator with top removed from resonator structure.

ORIGINAL PAGE
BLACK AND WHITE PHOTOGRAPH

MASTER OSCILLATOR
(WITH INTERNAL LENS)

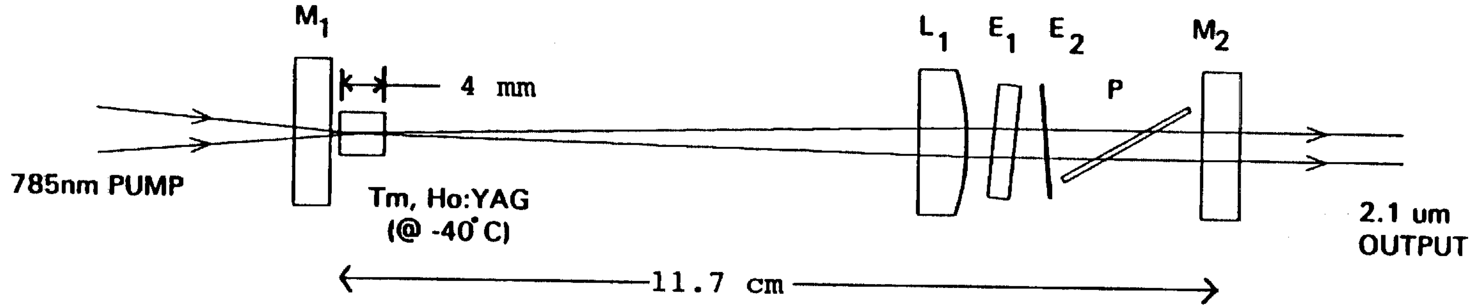

Figure 15. Schematic of the diode laser-pumped SLM Tm,Ho:YAG master oscillator resonator configuration.

1 second

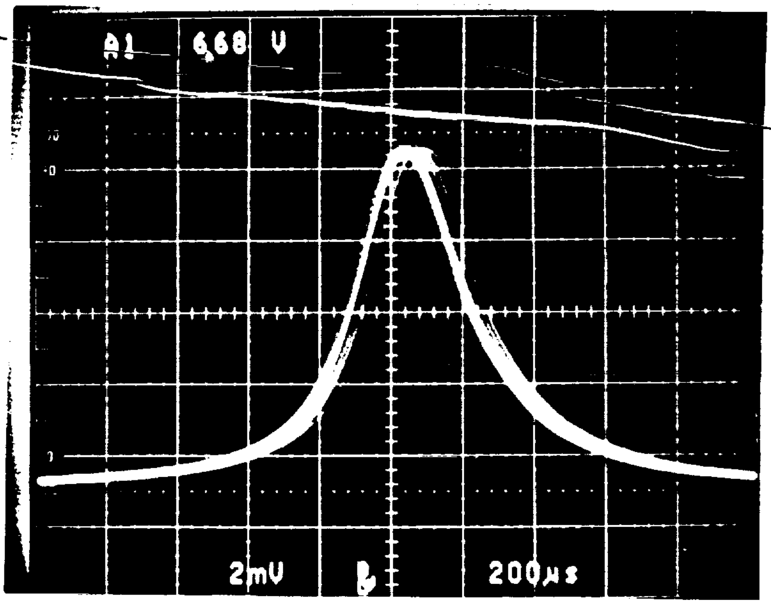

5 seconds

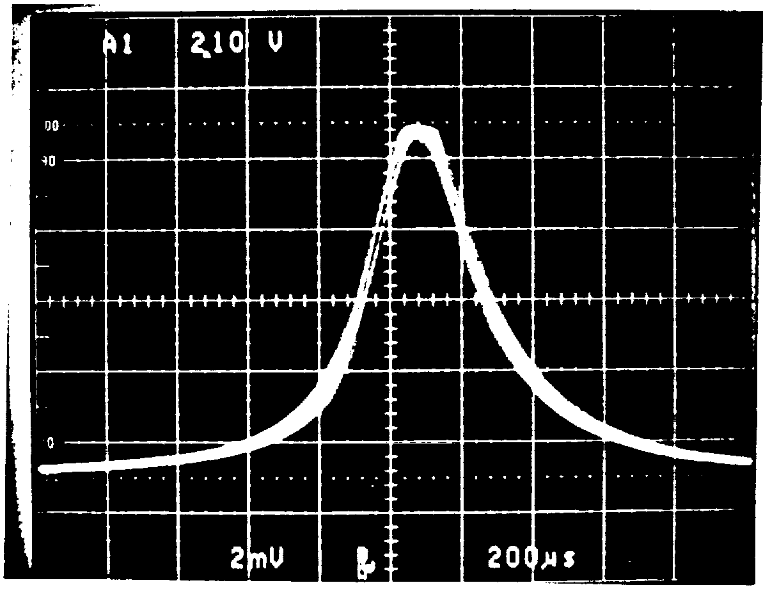

Figure 16. Typical frequency jitter and drift measured during 1 second and 5 second observation times using a 300 MHz free spectral range interferometer. The combined jitter and drift is <0.45 MHz peak to peak.

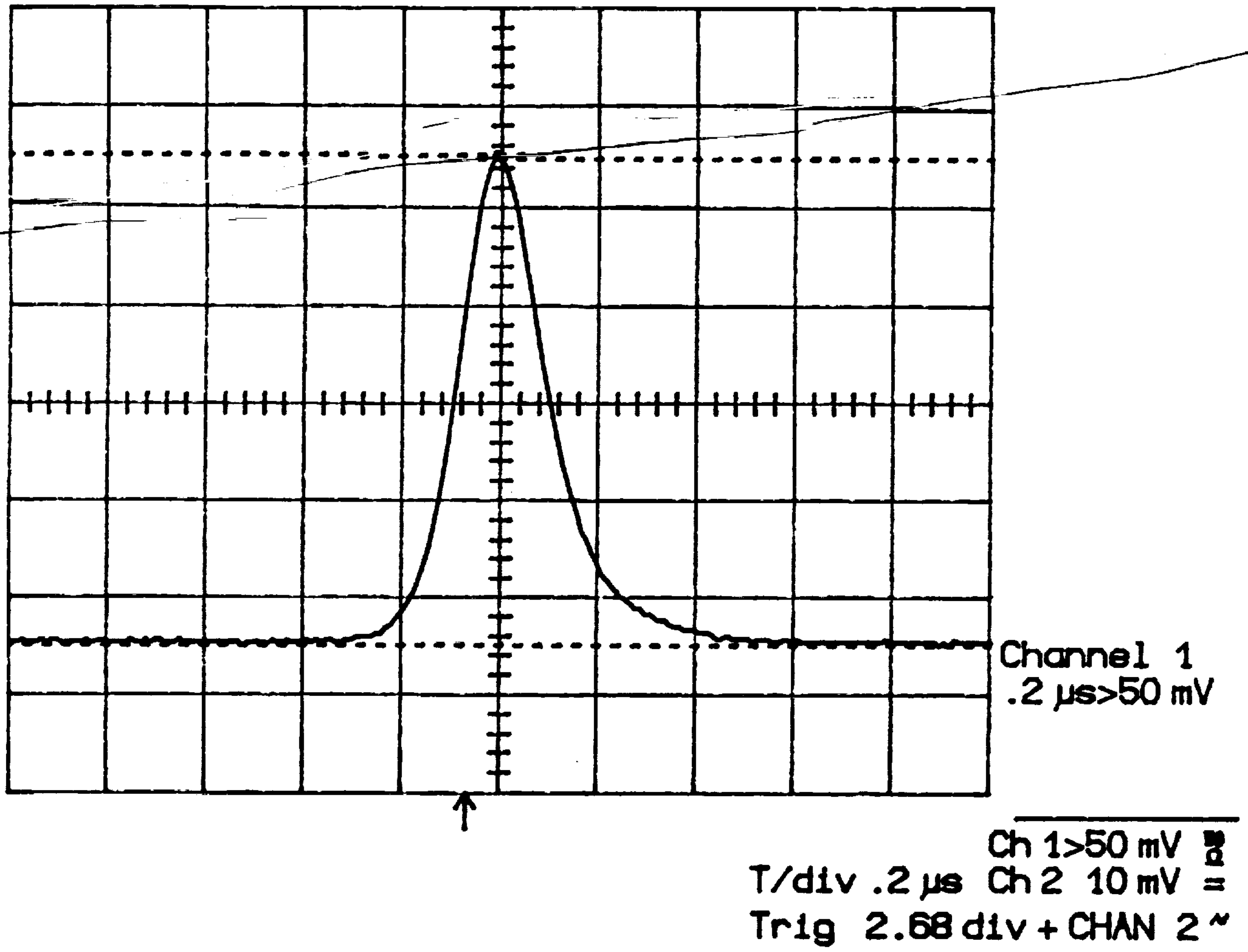

Figure 17. Intensity vs time of the transmitted 2.1 um CLR pulses with the pulse energy set to ~20 mJ.

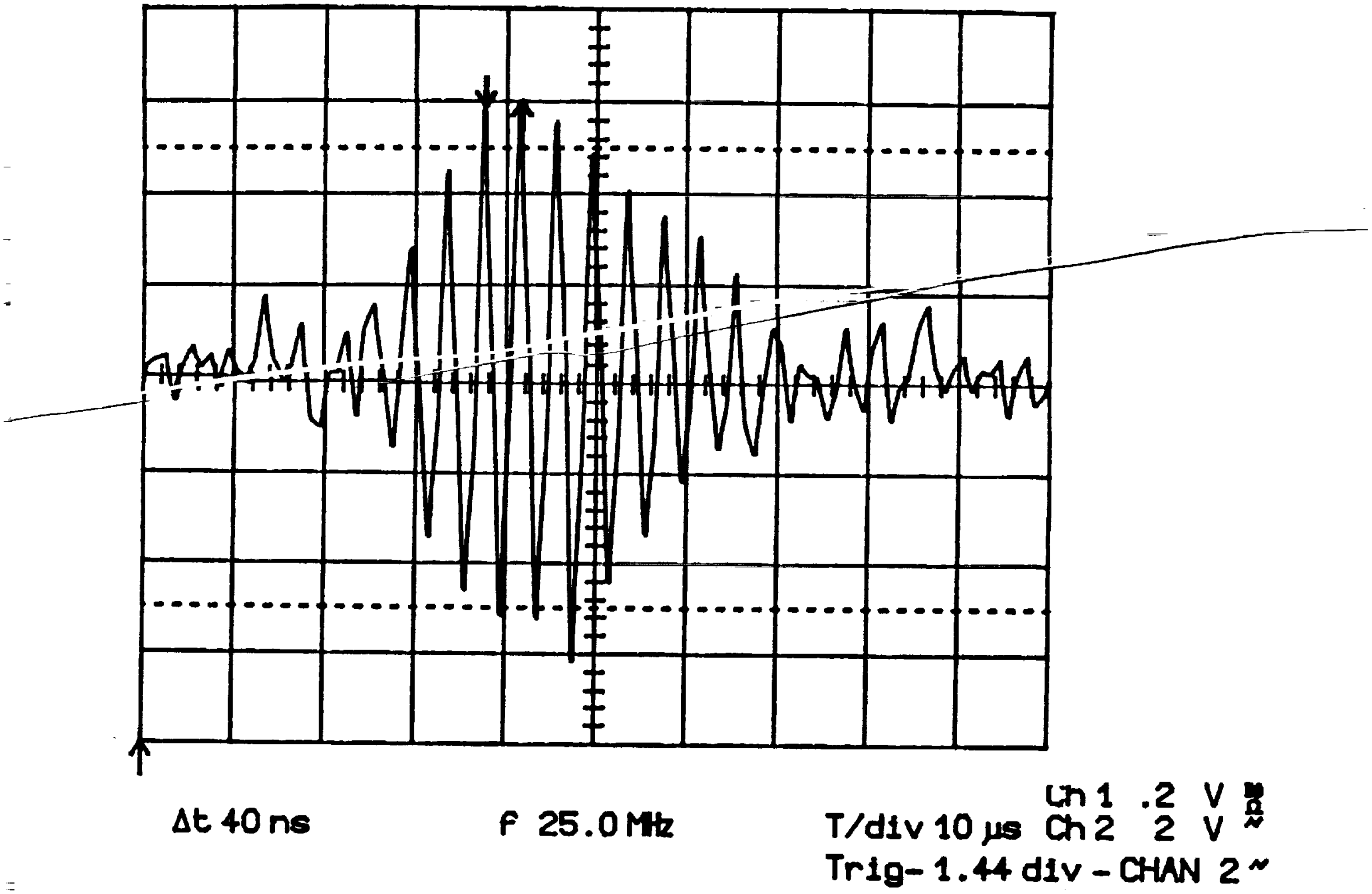

Figure 18. Single-shot CLR return on 4 Oct. 1990 from a mountainside located 14.9 km down range.

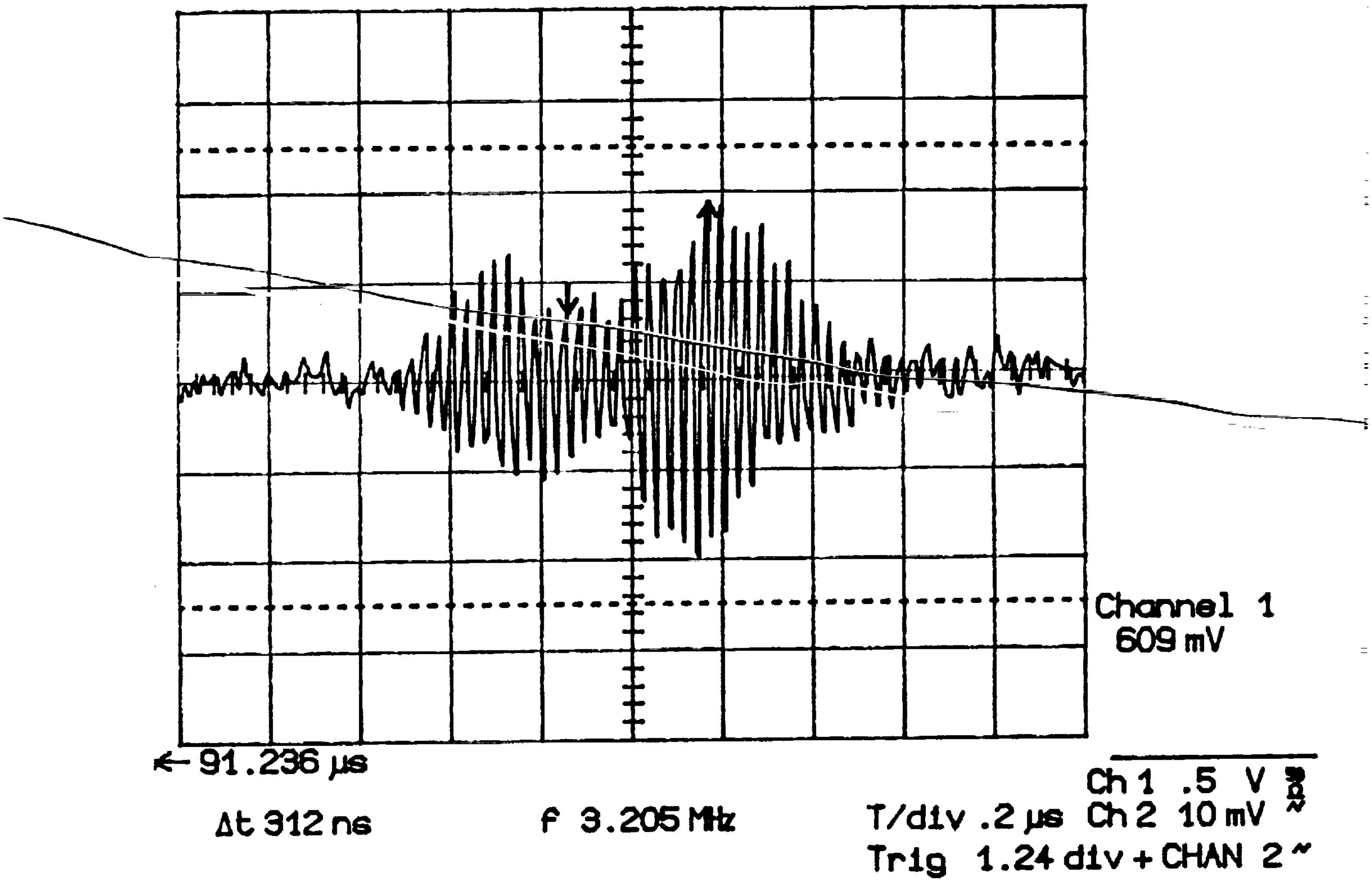

Figure 19. Single-shot CLR return on 4 Oct. 1990 from clouds located at ~13.8 km range.

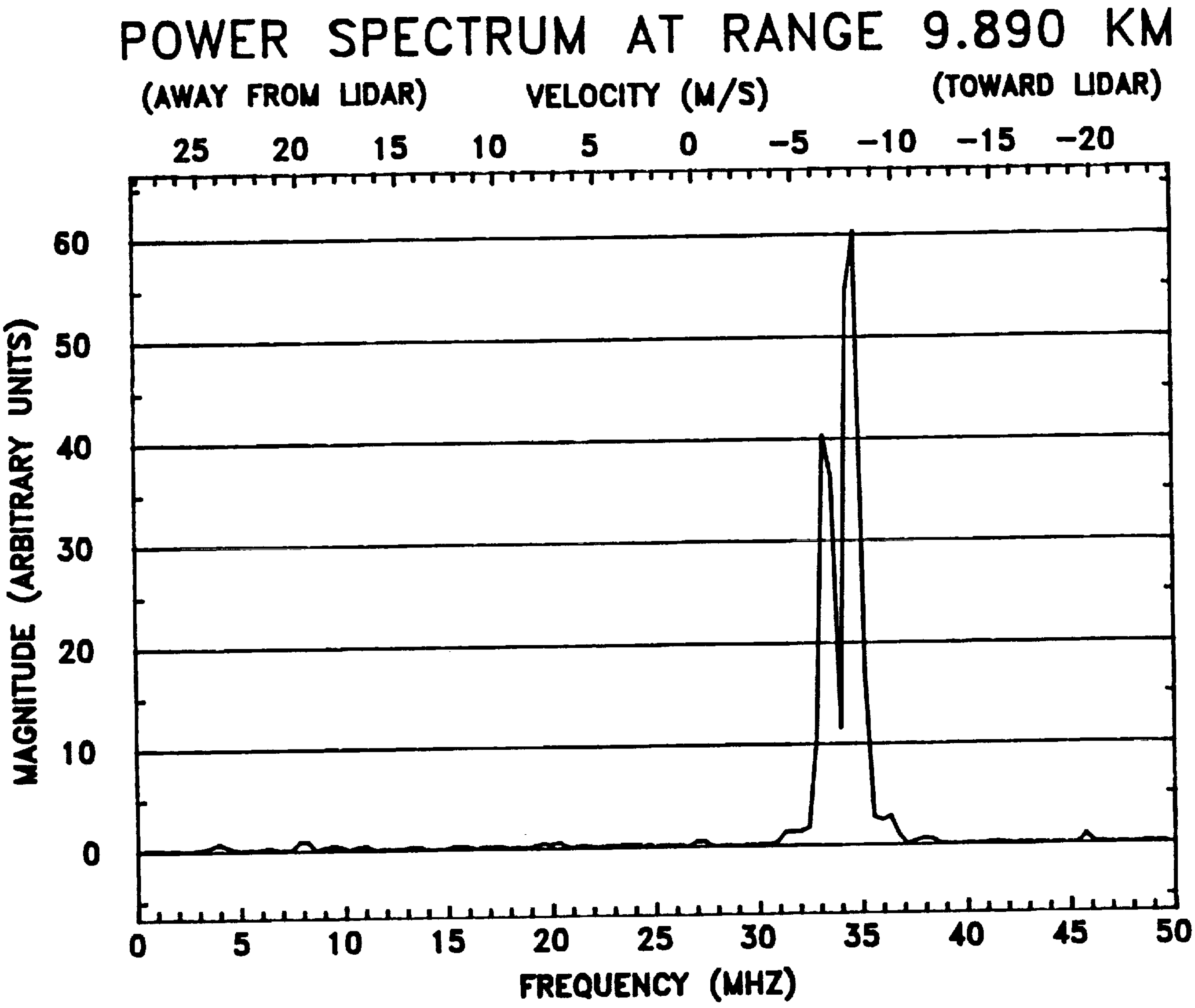

Figure 20. Power spectrum of a single-shot cloud return located ~9.9 km from the CLR.

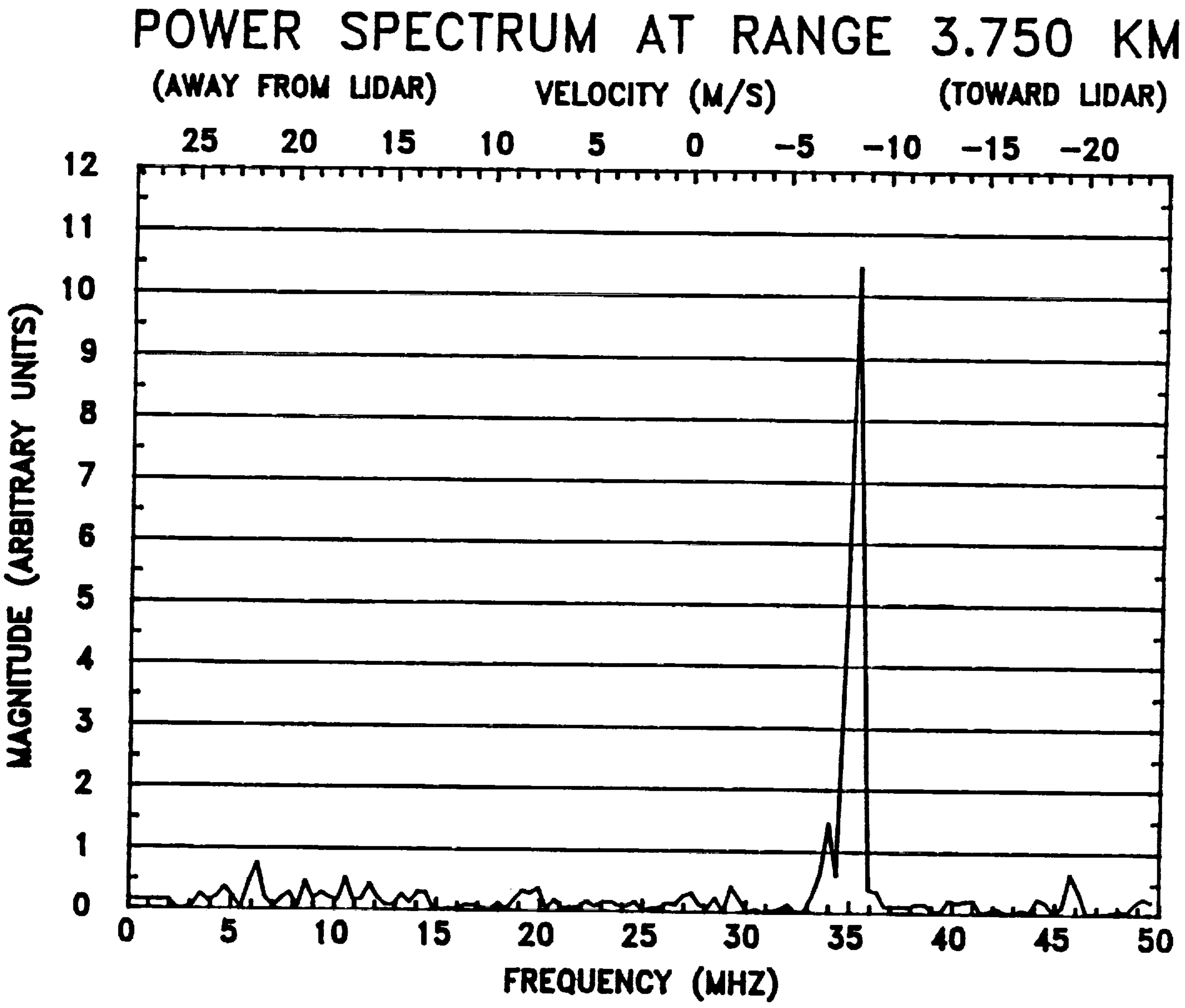

Figure 21. Power spectrum of aerosol return from 3.75 km range taken on 7 Oct. 1990.

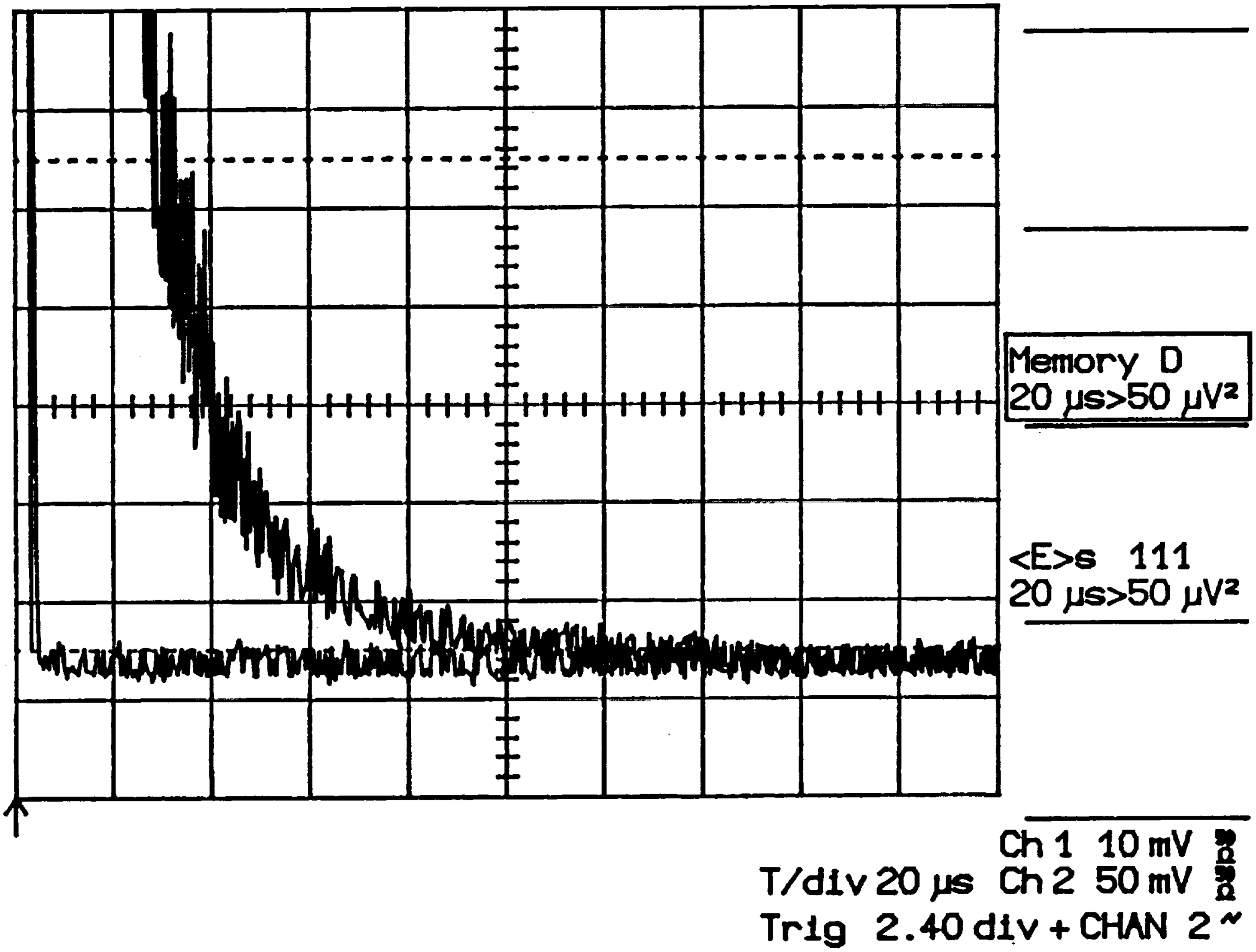

Figure 22. Upper Trace: A-scope display of aerosol return from 0-30 km for 111 shots averaged. Lower Trace: Background noise level.

10. SUMMARY AND CONCLUSIONS

VM is much simpler and more promising than SPM. The SPM analysis is much harder than the VM analysis. The non-systematic errors for VM (shot noise and speckle contributions) are less than 1% for $\beta > 10^{-11} m^{-1} sr^{-1}$ with a 10 s measurement time. Therefore, VM systematic errors will dominate. Priority should be given to perfecting VM operation, e.g., ensuring small systematic errors by optimal choice of system parameters (sensitivity analysis), improving alignment methods, improving signal processing methods, improving field calibration techniques, and improving beam quality. A crucial element of VM and SPM operation is accurate conversion of IF signal to IF power. Alternativces to a SAW processor should be investigated and may prove to be cheaper, more accurate (linear), and more reliable (less drift, etc.).

A Tm,Ho:YAG 2-μm laser radar system has been constructed and preliminary measurements demonstrating the first laser radar returns using an eyesafe solid-state CLR have been made.

11. REFERENCES

S.B. Alejandro, G.C. Koenig, J.M. Vaughan, and P.H. Davis, "SABLE: A South Atlantic Aerosol Backscatter Measurement Program," Bull. Amer. Meteorol. Soc. 71, 281 (1990).

G.M. Ancellet, M.J. Kavaya, R.T. Menzies, and A.M. Brothers, "Lidar telescope overlap function and effects of misalignment for unstable resonator transmitter and coherent receiver," Appl. Opt. 25, 2886 (1986).

R. Anderson, "Polarization and atmospheric backscatter coefficient measurements," Appl. Opt. 28, 865 (1989).

R.G. Beranek, J.R. Bilbro, D.E. Fitzjarrald, W.D. Jones, V.W. Keller, and B.S. Perrine, "Laser Atmospheric Wind Sounder (LAWS)," Proc. SPIE 1062, 234 (1989).

R.G. Frehlich and M.J. Kavaya, "Coherent Laser Radar Performance for General Conditions," submitted to Applied Optics (1990).

J.L Gras, C.M. Platt, R.M. Huffaker, W.D. Jones, and M.J. Kavaya, "Report of the Joint CSIRO/NASA Study. Optical Properties of Southern Hemisphere Aerosols," Coherent Technologies, Inc. Technical Report CTI-TR-8801 (Feb. 1988). Also NTIS report NASA CR-179287.

R.M. Hardesty, R.E. Cupp, M.J. Post, and T.R. Lawrence, "A ground-based, injection-locked, pulsed TEA laser for atmospheric wind measurements," Proc. SPIE 889, 23 (1988).

S.W. Henderson, R. M. Huffaker, M.J. Kavaya, C.P. Hale, J.R. Magee, and L.E. Myers, "Pulsed coherent solid-state 1.06 μm and 2.1 μm laser radar systems for remote velocity measurement," paper 1222-15, Proc. SPIE 1222, "Laser Radar V," Los Angeles, CA (18-19 Jan. 1990A).

S.W. Henderson, C.P Hale, J.R. Magee, and M.J. Kavaya, "Eyesafe Solid-State Coherent Lidar System for Wind and Water Vapor Measurements," Technical Report CTI-TR-9008 (July 1990B), Final Report for AF contract F047001-87-C-0144,

M.J. Kavaya, R.T. Menzies, D.A. Haner, U.P. Oppenheim, and P.H. Flamant, "Target reflectance measurements for calibration of lidar atmospheric backscatter data," Appl. Opt. 22, 2619 (1983).

M.J. Kavaya, "The JPL Lidar Target Calibration Facility," paper 11.1, Digest of Third Topical Meeting on Coherent Laser Radar: Technology and Applications," Great Malvern, England (8-11 July 1985).

M.J. Kavaya and R.T Menzies, "Lidar aerosol backscatter measurements: systematic, modeling, and calibration error considerations," Appl Opt. 24, 3444 (1985).

M.J. Kavaya, "Polarization effects on hard target calibration of lidar systems," Appl Opt. 26, 796 (1987).

M.J. Kavaya, S.W. Henderson, J.R. Magee, C.P. Hale, and R.M. Huffaker, "Remote wind profiling with a solid-state Nd:YAG coherent lidar," Opt. Lett. 14, 776 (1989).

R.M. Measures, "Laser Remote Sensing. Fundamentals and Applications," John Wiley & Sons, New York, New York (1984).

R.T. Menzies, M.J. Kavaya, P.H. Flamant, and D.A. Haner, "Atmospheric aerosol backscatter measurements using a tunable coherent CO_2 lidar," Appl. Opt. 23, 2510 (1984).

National Academy of Sciences, "Technological and Scientific Opportunities for Improved Weather and Hydrological Services in the Coming Decade," Select Committee on the National Weather Service (1980).

M.J. Post and R.E. Cupp, "Optimizing a pulsed Doppler lidar," Appl. Opt. 29, 4145 (1990).

R. Targ, M.J. Kavaya, R.M. Huffaker, and R.L. Bowles, "Coherent Lidar Airborne Windshear Sensor: Performance Evaluation," to be published in Appl. Opt. (1990).

APPENDIX A. Volume Mode Estimation of β

The average coherent lidar power $<i_S^2>[A^2]$ is given by

$$<i_S^2> = 2\left[\frac{\eta G_D e}{h\nu}\right]^2 \int_{-\infty}^{\infty}\int_{-\infty}^{\infty} M_S(\vec{r}_1,\vec{r}_2,0)W(\vec{r}_1)W^*(\vec{r}_2)E_{LO}^*(\vec{r}_1,0)E_{LO}(\vec{r}_2,0)d\vec{r}_1 d\vec{r}_2 \qquad \text{(A1)}$$

η = detector AC quantum efficiency [electrons/photon]

G_D = amplifier gain [dimensionless]

$h = 6.626\text{x}10^{-34}$ $[Js]$ = Plancks constant

$\nu = \frac{c}{\lambda}$ = frequency of the optical field $[s^{-1}]$

$E_{LO}(\vec{r},0)$ = LO field back-propagated to receiver plane $[Wm^{-2}]^{1/2}$

$W(\vec{r})$ = transfer function of receiver lens [dimensionless]

$M_S(\vec{r}_1,\vec{r}_2,0) = <E_S(\vec{r}_1,0)E_S^*(\vec{r}_2,0)>$ = mutual coherence function of received field at the receiver $[Wm^{-2}]$

For randomly distributed aerosol particles, the mutual coherence function of the total backscattered field is the sum of the mutual coherence functions from each aerosol particle. The mutual coherence of the backscattered field from an aerosol at $(\vec{p},R)$ with cross section σ $[m^2sr^{-1}]$ is

$$M_S(\vec{r}_1,\vec{r}_2,0) = \lambda^2\sigma<I_T(\vec{p},R)G(\vec{r}_1,\vec{p},R)G^*(\vec{r}_2,\vec{p},R)> \qquad \text{(A2)}$$

where $G(\vec{r},\vec{p},R)$ is the Green's function $[m^{-4}]$; i.e., the field at $(\vec{r},0)$ due to a unit point source at $(\vec{p},R)$. The mutual coherence function of the total field is the sum of the mutual coherence functions of all the scattering aerosol particles, i.e.,

$$M_S(\vec{r}_1,\vec{r}_2,0) = \int_0^{\infty}\int_{-\infty}^{\infty}\int_0^{\infty}\lambda^2\sigma n(\sigma,R)<I_T(\vec{p},R)G(\vec{r}_1,\vec{p},R)G^*(\vec{r}_2,\vec{p},R)>d\sigma d\vec{p}dR \qquad \text{(A3)}$$

where $n(\sigma,R)[m^{-5}sr]$ is the number of aerosol particles per unit volume per unit σ at range R. If $n(\sigma,R)$ is independent of range R, then

$$M_S(\vec{v}_1,\vec{v}_2,0) = \beta\int_0^{\infty}\int_{-\infty}^{\infty}\lambda^2 < I_T(\vec{p},R)G(\vec{v}_1,\vec{p},R)G^*(\vec{v}_2,\vec{p},R) > d\vec{p}\,dR \tag{A4}$$

where

$$\beta = \int_0^{\infty}\sigma n(\sigma)d\sigma \tag{A5}$$

is the aerosol backscatter coefficient $[m^{-1}sr^{-1}]$. The average coherent lidar power is then

$$< i_S^2 > = 2\beta\left[\frac{\eta G_D e}{h\nu}\right]^2 \int_0^{\infty}\int_{-\infty}^{\infty}\int_{-\infty}^{\infty}\int_{-\infty}^{\infty}\lambda^2 < I_T(\vec{p},R)G(\vec{v}_1,\vec{p},R)G^*(\vec{v}_2,\vec{p},R) > W(\vec{v}_1)W^*(\vec{v}_2)E_{LO}^*(\vec{v}_1,0)E_{LO}(\vec{v}_2,0)d\vec{v}_1 d\vec{v}_2 d\vec{p}\,dR \tag{A6}$$

It may be written

$$< i_S^2 > = \beta G_V P_T \tag{A7}$$

where G_V is the system gain $[A^2mW^{-1}sr]$, i.e.,

$$G_V = \int_0^{\infty}G_V(R)dR \tag{A8}$$

and

$$G_V(R) = 2\left[\frac{\eta G_D e}{h\nu}\right]^2 \frac{\lambda^2}{P_T}\int_{-\infty}^{\infty}\int_{-\infty}^{\infty}\int_{-\infty}^{\infty} < I_T(\vec{p},R)G(\vec{v}_1,\vec{p},R)G^*(\vec{v}_2,\vec{p},R) > W(\vec{v}_1)W^*(\vec{v}_2)E_{LO}^*(\vec{v}_1,0)E_{LO}(\vec{v}_2,0)d\vec{v}_1 d\vec{v}_2 d\vec{p} \tag{A9}$$

is the coherent lidar system gain density $[A^2srW^{-1}]$.

APPENDIX B. Single Particle Mode Estimation of β

The mutual coherence function of the backscattered field from a single particle of cross section $\sigma\,[m^2 sr^{-1}]$, which is far enough away that the received field approximates the field from a point source under the parabolic approximation, is given by

$$M_S(\vec{v}_1,\vec{v}_2,0) = \frac{\sigma I(\vec{p},R)}{R^2}\exp\left[\frac{ik}{2R}\left[(\vec{p}-\vec{v}_1)^2 - (\vec{p}-\vec{v}_2)^2\right]\right] \tag{B1}$$

where

$\vec{p} = [p_x, p_y]$ = transverse trajectory of the particle [m] at range R,

$$I_T(\vec{p},R) = \frac{k^2}{(2\pi R)^2}\int_{-\infty}^{\infty}\int_{-\infty}^{\infty} E_T(\vec{u}_1,0)E_T^{*}(\vec{u}_2,0)\exp\left[\frac{ik}{2R}\left[(\vec{p}-\vec{u}_1)^2 - (\vec{p}-\vec{u}_2)^2\right]\right]d\vec{u}_1 d\vec{u}_2\,, \tag{B2}$$

$\vec{u} = [u_x, u_y]$ is the transverse coordinate [m] at the transmitter plane perpendicular to the R axis,

$E_T(\vec{u},0)$ = transmitted field $[Wm^{-2}]^{1/2}$ at R = 0,

$I_T(\vec{u},0) = E_T(\vec{u},0)E_T^{*}(\vec{u},0)$ = transmitted irradiance $[Wm^{-2}]$.

The maximum lidar signal $S_j\,[A^2]$ for the jth particle event will occur for some coordinate (p_x, p_{ym}, R) of the trajectory, where p_x is the displacement from the laser beam axis. This maximum signal is given by

$$S_j(p_x,p_{ym},R) = \frac{2P_T\sigma}{R^2}\left[\frac{\eta G_D e}{h\nu}\right]^2\int_{-\infty}^{\infty}\int_{-\infty}^{\infty} J_T(\vec{p}_m,R)\exp\left[\frac{ik}{2R}\left[(\vec{p}_m-\vec{v}_1)^2 - (\vec{p}_m-\vec{v}_2)^2\right]\right]$$

$$W(\vec{v}_1)W^{*}(\vec{v}_2)E_{LO}^{*}(\vec{v}_1,0)E_{LO}(\vec{v}_2,0)d\vec{v}_1 d\vec{v}_2 \tag{B3}$$

where $\vec{p}_m = (p_x, p_{ym})$ is the transverse coordinate of the maximum signal for the jth particle (see Figure 2) and $J_T(\vec{p},R) = I_T(\vec{p},R)/P_T\ [m^{-2}]$ is the normalized irradiance.

The proper statistic for estimating β is the sum S $[A^2]$ of the maximum (or peak) signals:

$$S = \sum_{j=1}^{N} S_j(p_x,p_{ym},R) \tag{B4}$$

For large N (many particle events), this statistic will be very close to its ensemble average <S>. (Since is assumed constant over the observation volume, the statistical process is ergodic and stationary.) The observation volume is determined by the observation time $T\,[s]$. During this time the lidar system will have traversed a distance $V_A T$ through the atmosphere. We obtain $<S>$ by performing an ensemble average over all the aerosol particles contained in the observation volume:

$$<S> = \int_0^\infty \int_{-\infty}^\infty \int_0^{V_A T} \int_0^\infty S_j(p_x, p_{ym}, R)\, n(\sigma) d\sigma dy dp_x dz = 2P_T \int_0^\infty \int_{-\infty}^\infty \int_0^{V_A T} \int_0^\infty \int_{-\infty}^\infty \int_{-\infty}^\infty \left[\frac{\eta G_D e}{h\nu}\right]^2 \sigma n(\sigma) \frac{J_T(\vec{p}_m, R)}{R^2}$$

$$\exp\left[\frac{ik}{2R}\left[(\vec{p}_m - \vec{v}_1)^2 - (\vec{p}_m - \vec{v}_2)^2\right]\right] W(\vec{v}_1) W^*(\vec{v}_2) M_{LO}{}^*(\vec{v}_1, \vec{v}_2, 0)\, d\vec{v}_1 d\vec{v}_2 d\sigma dy dp_x dz \qquad \text{(B5)}$$

The integrand in Eq. (B5) is independent of y so the y integral may be evaluated, producing $V_A T$. If the laser's optic axis is at angle θ to the z axis, then $z = R\cos\theta$. The angle between the R axis and the particles' trajectories will be $90^0 - \theta$. The integration over z is more conveniently performed by changing variables using $dz = dR\cos\theta$ and integrating over R. The σ integration may be performed if we assume $n(\sigma)$ is constant over the dominant region of integration. Then

$$<S> = \beta P_T G_S V_A T \cos\theta, \qquad \text{(B6)}$$

where $G_S\ [A^2 W^{-1} sr]$ is the total system gain given by

$$G_S = \int_0^\infty \int_{-\infty}^\infty G_S(p_x, R)\, dp_x dR. \qquad \text{(B7)}$$

(The definition of β in Eq. (B6) is the same for direct detection and heterodyne detection volume mode measurements.) $G_S(p_x, R)$ is the system's transverse area gain density $[A^2 W^{-1} m^{-2} sr]$ for a scattering particle at $(\vec{p}, R)$ given by

$$G_S(p_x, R) = 2\left[\frac{\eta G_D e}{h\nu}\right]^2 \int_{-\infty}^\infty \int_{-\infty}^\infty \frac{J_T(\vec{p}_m, R)}{R^2} \exp\left[\frac{ik}{2R}\left[(\vec{p}_m - \vec{v}_1)^2 - (\vec{p}_m - \vec{v}_2)^2\right]\right]$$

$$W(\vec{v}_1) W^*(\vec{v}_2) E_{LO}{}^*(\vec{v}_1, 0) E_{LO}(\vec{v}_2, 0)\, d\vec{v}_1 d\vec{v}_2 \qquad \text{(B8)}$$

APPENDIX C. Monte Carlo Calibration of SPM

Section 4 assumed that the calibration of the lidar system utilized apparatus that shot individual test particles through the beam with known test parameters σ_C, P_C, p_{xc}, and R_C. Both p_x and R were assumed adjustable over a sufficient volume. This appendix treats the case when the particle's value of p_{xc} is not known, but the probability density function (PDF) $f(p_{xc})$ of the value p_{xc} is uniform. Specifically,

$$f(p_{xc}) = \begin{cases} \frac{1}{L} \text{ if } -L/2 < p_{xc} < L/2 \\ 0 \quad \mathit{otherwise} \end{cases} \tag{C1}$$

We define the Monte Carlo statistic Z to be

$$Z(p_{xc}) = \frac{L}{P_C \sigma_C N_C} \sum_{j=1}^{N_C} S_C(p_{xc}, R_C) \tag{C2}$$

where $S_C(p_{xc}, R_C)$ is the maximum lidar signal power for the jth calibration particle event, p_{xc} is the random displacement from the laser beam axis, and N_C is the (large) number of observed events. The average of the statistic Z is

$$<Z(p_{xc})> = \int_{-\infty}^{\infty} f(p_{xc}) Z(p_{xc}) dp_{xc} = \frac{1}{P_C \sigma_C N_C} \int_{-L/2}^{L/2} \sum_{j=1}^{N_C} S_C(p_{xc}, R_C) dp_{xc} \tag{C3}$$

If we assume L is much larger than the beam width at R_C, the integration may be considered from $-\infty$ to ∞, and, referring to Eqs. (64) and (65),

$$<Z> = G_S(R_C). \tag{C4}$$

Equation (C4) is used to obtain the system gain G_S in Eq. (36) to calibrate β. Any deviation from the uniform PDF behavior of p_{xc} will produce an error in β.

APPENDIX D

CW COHERENT LASER RADAR: CALCULATION OF MEASUREMENT LOCATION AND VOLUME

Michael J. Kavaya
Paul J. M. Suni

Coherent Technologies, Inc.
3300 Mitchell Lane, Suite 330
Boulder, CO 80301-2272 USA
(303) 449-8736
(303) 449-8780 (FAX)

ABSTRACT

The SNR equation of a CW, monostatic, coherent laser radar system is examined for the case of a distributed aerosol target. Calculations and plots are presented showing the location in range and the volume of the laser radar measurement.

KEY WORDS

Laser Radar, LIDAR, LADAR, CW LIDAR, Coherent LIDAR, Heterodyne LIDAR

1. Introduction

Monostatic, coherent detection laser radar (LADAR or LIDAR, light detection and ranging) systems with continuous-wave (CW) laser sources, with the atmosphere serving as a distributed target, have proven to be important remote sensing tools for many applications such as measurements of radial or line-of-sight (LOS) wind velocity,[1-6] true airspeed of aircraft,[7-8] transverse wind velocity,[9] aircraft trailing vortices,[10] and atmospheric aerosol backscatter coefficients.[11-14] Comparisons of CW laser radar wind measurements with other wind velocity monitors have been performed, [3,6,7,9,15,16] as have investigations of intensity calibration issues.[11,12,17,18]

A separate but very important consideration when discussing CW coherent laser radar (CLR) measurements based on backscatter from atmospheric aerosol particles is the question: "Exactly where along the optic (range) axis is the measurement being made?" This question comprises the issues of 1) whether the range resolution of the measurement is too small or too big, 2) whether a high backscatter region far from the laser radar (e.g., cloud or ground) corrupts the desired backscatter or wind velocity measurement,[16] 3) whether a region of large wind shear far from the laser radar corrupts a wind velocity measurement by broadening the signal spectrum, and 4) over what ranges must a hard calibration target be used to achieve a desired characterization of the laser radar. The laser beam diameter vs range is important to ascertain eye safety and whether the beam irradiance may alter the properties of the aerosol particles. Also, the laser radar measurement volume is important since too small a volume may violate the statistical assumptions (many particles) of the laser radar theory, or may cause a measurement bias by missing scarce yet important large aerosol particles that contribute to the backscatter coefficient. The measurement volume is also important in explaining differences between CW laser radar measurements, and measurements made with other instruments. To our knowledge, published discussions of these effects have been limited to the range interval yielding, e.g., 50% of the signal under tight focusing conditions.[1,3,7,10-12,16]

In this paper we solve the laser radar SNR equation for any percentile range of the received signal, and therefore for any definition of range resolution; and we also solve for the measurement volume of a CW coherent laser radar system under any focusing conditions.

2. SNR Equation

We start with the general untruncated Gaussian beam monostatic, pulsed, shot-noise-limited CLR signal-to-noise ratio (SNR) equation and assume: 1) CW transmit laser power P_{CW} [W], 2) negligible atmospheric extinction, 3) negligible atmospheric refractive turbulence effects, 4) constant aerosol backscatter coefficient β [$m^{-1}sr^{-1}$] vs range R [m], 5) matched diameter and phase curvature F [m] of the untruncated Gaussian transmitted and back propagated local oscillator (BPLO) optical fields, 6) negligible beam truncation by the transmit/receive lens or telescope, and 7) a photovoltaic detector. Under these conditions the dimensionless SNR equation becomes[19]

$$\mathrm{SNR} = \frac{\eta\pi P_{CW}\beta}{h\nu B}\int_0^\infty \frac{dR}{\frac{4R^2}{D_o^2} + \left(1 - \frac{R}{F}\right)^2 \frac{\pi^2 D_o^2}{4\lambda^2}}$$

$$= \frac{\eta P_{CW}\beta\lambda}{h\nu B}\int_0^\infty \frac{R_R\,dR}{R^2 + \left(1 - \frac{R}{F}\right)^2 R_R^2} \tag{1}$$

where η [electrons/photon] is the detector quantum efficiency at the signal frequency, $h = 6.626\ 10^{-34}$ [Js] is Planck's constant, ν [Hz] is the optical frequency, B [Hz] is the receiver bandwidth, $\lambda = c/\nu$ [m] is the wavelength of the optical field, c [m/s] is the speed of light, and D_o [m] is the e^{-2} (14%) intensity diameter of the transmitted and BPLO Gaussian fields. The Rayleigh range [m],

$$R_R \triangleq \frac{\pi D_o^2}{4\lambda}, \tag{2}$$

is defined for Gaussian beams as the distance from the beam waist (minimum diameter = D_o) to the point where the beam area has doubled.[20] Alternatively, for light diffracted by an aperture of diameter D_o, ranges much larger than R_R will satisfy the

Fraunhofer or far-field assumption, and the field at range R will be the Fourier transform of the field in the aperture,[21] changing only in size but not in shape with increasing R.

The two terms in the denominator of Eq. (1) reduce the coherent detection SNR. The first term represents the effect of the finite receiver solid angle, and the second term represents both the speckle effects from the size of the illuminated diffuse aerosol target, and the phase-front mismatch (PFM) at the receiver when $R \neq F$. The integrand I in Eq. (1) is the "weighting function" of the received signal along the range axis under the assumed conditions. For small R ($R \ll F$ <u>and</u> $R \ll R_R$), the integrand becomes independent of R and equal to R_R^{-1}. As R decreases, the gain in SNR, due to increasing receiver solid angle, exactly cancels the SNR loss due to speckle/PFM. For large R ($R \gg F$ <u>or</u> $R \gg R_R$) the integrand decreases as R^{-2} due to the decreasing receiver solid angle.

For $R = F$, the integrand equals

$$I(R = F) = \frac{R_R}{F^2} = \frac{\pi D_o^2}{4\lambda F^2}, \tag{3}$$

which is the proportional to the effective solid angle of the receiver.

The range to the peak R_p [m] of the SNR weighting function is found by setting the derivative of the integrand in Eq. (1) with respect to range R to zero, yielding:

$$R_p = \frac{F R_R^2}{R_R^2 + F^2} = \frac{F}{1 + F_N^2} \tag{4}$$

where

$$F_N \triangleq F/R_R \tag{5}$$

is the focal range normalized by the Rayleigh range (dimensionless). For small F_N ($F << R_R$),

$$R_p \approx F, \tag{6}$$

and the peak SNR occurs at the focal range (i.e., tight focusing). For large F_N ($F >> R_R$),

$$R_p \approx \frac{R_R^2}{F} = \frac{F}{F_N^2}, \tag{7}$$

and the peak SNR range is proportional to F^{-1}, i.e., the peak originates close to the laser radar. One result of this is that for laser radars focused far away ($F >> R_R$), the very term "focus" loses its meaning. The range to the peak SNR goes to zero for both very small and very large F. Since Eq. (4) is also the range to the Gaussian beam waist,[20] we conclude that the peak SNR <u>always</u> comes from the beam waist position.

For $R = R_p$, the peak SNR will be proportional to the integrand in Eq. (1) which becomes

$$I(R = R_p) = \frac{R_R^2 + F^2}{R_R\, F^2} \tag{8}$$

For small F_N ($F << R_R$), $I(R = R_p) \approx R_R F^{-2}$ and the peak SNR gets very large since receiver solid angle SNR losses and speckle/PFM losses are simultaneously low. For large F_N ($F >> R_R$), $I(R = R_p) \approx R_R^{-1}$, a constant value identical to the small R value of I, since R_p is small and we assumed $R = R_p$. The ratio of the SNR at the focal range to the peak SNR is found by combining Eqs. (3) and (8):

$$\frac{SNR(R=F)}{SNR(R=R_p)} = \frac{R_R^2}{R_R^2 + F^2} = \frac{1}{1 + F_N^2} \tag{9}$$

For small F_N ($F << R_R$), the ratio approaches unity, indicating that the peak SNR occurs at the focal range. For large F_N ($F >> R_R$), the ratio approaches zero as F^{-2}, indicating that a negligible contribution to SNR comes from the focal range.

The value of F which maximizes R_p is found by setting the derivative of Eq. (4) with respect to F to zero, yielding:

$$F_p = R_R \tag{10}$$

The value of R_p when $F = F_p$ is found by substituting Eq. (10) into Eq. (4):

$$R_p(F_p) = \frac{R_R}{2} \tag{11}$$

When $F = R_R$, the peak SNR (and the beam waist) is at its greatest range and this range is $R_R/2$. Focus settings smaller or larger will cause the peak SNR to move closer to the laser radar. As F is increased from 0 towards ∞, the peak SNR decreases and moves to larger ranges until $F = R_R$. Then the peak SNR continues to decrease and moves back to smaller ranges. For small F, the illuminated aerosol spot at $R = F$ is very small, and the losses due to finite receiver solid angle and speckle/PFM are both small. On the other hand, the losses due to speckle/PFM increase quickly away from the focus. Therefore the SNR is high and peaks sharply at $R_p \sim F$. For large F, the effects of speckle/PFM loss compete with the effect of R^2, producing a broad SNR curve with a peak collocated with the beam waist at $R_p < F$. When the focal range is set to the Rayleigh range, the integrand value at the Rayleigh range is $I(R = F = R_R) = R_R^{-1}$. The integrand takes on this same value for very small R, from which we draw the remarkable conclusion that, e.g., the first cm of range contributes the same SNR as a 1 cm slice of range at $R = R_R$, which may be many km away. Put another way, the solid angle SNR loss at $R = R_R$ exactly equals the speckle/PFM SNR loss at small R.

As shown by Sonnenschein and Horrigan,[22] the integral in Eq. (1) may be solved analytically. Eq. (1) may be written as

$$\mathrm{SNR} = \frac{\eta\, P_{cw}\beta\lambda}{h\nu B} \int_0^{\infty} \frac{dR_N}{1 - \dfrac{2R_N}{F_N} + \left[1 + \dfrac{1}{F_N^2}\right] R_N^2} \tag{12}$$

where

$$R_N \overset{\Delta}{=} R/R_R \tag{13}$$

is the range normalized by the Rayleigh range (dimensionless). Letting $a = 1$, $b = -2/F_N$, $c = 1 + 1/F_N^2$, and $\Delta = 4ac-b^2 = 4$, we may look up the integral[23]

$$\int \frac{dx}{a + bx + cx^2} = 2\Delta^{-1/2} \tan^{-1}\left[(b + 2cx)\Delta^{-1/2}\right] \tag{14}$$

for $\Delta > 0$. Using Eq. (14), Eq. (12) becomes

$$\mathrm{SNR}(\infty) = \frac{\eta\pi P_{cw}\beta\lambda}{2h\nu B}\left[1 + \frac{2}{\pi} \tan^{-1}\left[\frac{1}{F_N}\right]\right] \tag{15}$$

where the argument ∞ for SNR indicates that all ranges from 0 to ∞ are included.

Note that only the second term in the brackets contains any dependence on D_o or F, the beam diameter and focal range. For a sufficiently tight focus, $F_N << 1$, the expression in the brackets equals 2. For $F_N >> 1$, i.e., a collimated beam, the expression in the brackets equals 1. Therefore, the beam diameter and focal range may affect the SNR only within a factor of 2 (3 dB). A tightly focused CW laser radar will have twice the SNR of a collimated CW laser radar in a uniform atmosphere. (Recall that we are neglecting atmospheric extinction and refractive turbulence effects.)

3. Comparison to Past Work

Eq. (15) may be directly compared to Eq. (24) of Sonnenschein and Horrigan[22]. The RHS of their Eq. (24) must be multiplied by 2 due to an unreported error. Also their variable "R" is the e^{-2} intensity radius and corresponds to our D/2. Finally, our Eq. (1) is for a photovoltaic detector as is their Eq. (24) when multiplied by 2. With these caveats, our Eq. (15) equals their Eq. (24).

4. Wavelength Dependence of SNR

Since $\nu = c/\lambda$, Eq. (15) contains an explicit λ^2 dependence. The detection bandwidth B will also be proportional to λ^{-1} if allowance is made for a fixed atmospheric velocity width ΔV [m/s], or for a maximum unknown radial velocity of the aerosol particles, V_{max} [m/s], either toward or away from the laser radar. Ignoring any λ dependence of η or P_{cw}, and neglecting the terms in the brackets, we see that $SNR(\infty) \propto \beta\lambda^3$. The λ dependence of β varies greatly in nature but lies between λ^0 (Mie limit) and λ^{-4} (Rayleigh limit). A commonly used approximation that $\beta \propto \lambda^{-2}$ would result in $SNR(\infty) \propto \lambda$, favoring larger wavelengths. Of course, larger values of λ may lower $SNR(\infty)$ by as much as 3 dB through the bracketed terms in Eq. (15). (Strictly, the above reasoning applies only to aerosol backscatter measurements. Wind velocity error expressions include both SNR and other terms that also depend on λ.)

5. Cumulative SNR

The dimensionless cumulative SNR is defined as

$$CUMSNR(R_N) \triangleq \frac{SNR(R_N)}{SNR(\infty)} \qquad (16)$$

where $SNR(\infty)$ is given in Eq. (15). Using Eq. (12)

$$\mathrm{SNR}(R_N) = \frac{\eta\ P_{cw}\beta\lambda}{h\nu B} \int_0^{R_N} \frac{dz}{1 - \frac{2z}{F_N} + \left[1 + \frac{1}{F_N^2}\right] z^2} \tag{17}$$

Employing Eq. (14) to solve Eq. (17) produces

$$\mathrm{SNR}(R_N) = \frac{\eta P_{cw}\beta\lambda}{h\nu B}\left\{\tan^{-1}\left[-\frac{1}{F_N} + \left[1 + \frac{1}{F_N^2}\right]R_N\right] + \tan^{-1}\left[\frac{1}{F_N}\right]\right\} \tag{18}$$

We now use the trigonometric identity[23]

$$\tan^{-1}x + \tan^{-1}y = \alpha + \tan^{-1}\left[\frac{x + y}{1 - xy}\right] \tag{19}$$

where $\alpha = 0$[rad] if $xy < 1$, $\alpha = \pi$ if $x > 0$ and $xy > 1$, and $\alpha = -\pi$ if $x < 0$ and $xy > 1$. We set

$$x = \frac{1}{F_N} \tag{20}$$

and

$$y(R_N) = \left[1 + \frac{1}{F_N^2}\right]R_N - \frac{1}{F_N} \tag{21}$$

yielding

$$xy(R_N) = \left[\frac{1}{F_N}\right]\left[\left[1 + \frac{1}{F_N^2}\right]R_N - \frac{1}{F_N}\right] \tag{22}$$

In the limit of a tight focus, $F_N << 1$, $xy(R_N) \sim R_N F_N^{-3}$ which will be greater than 1 except for very small values of R_N. In the collimated limit, $F_N >> 1$, $xy(R_N) \sim R_N F_N^{-1}$ which will be less than 1 except when $R > F$. Using Eqs. (18) and (19) we find

$$\mathrm{SNR}(R_N) = \frac{\eta P_{cw}\beta\lambda}{h\nu B}$$

$$\times \left\{ \alpha(R_N) + \tan^{-1}\left[\frac{\left[1 + \frac{1}{F_N^2}\right] R_N}{1 - \left[1 + \frac{1}{F_N^2}\right] \left[\frac{R_N}{F_N}\right] + \left[\frac{1}{F_N}\right]^2} \right] \right\}$$

$$= \frac{\eta\, P_{cw} \beta \lambda}{h\nu B} \left\{ \alpha(R_N) + \tan^{-1}\left[\frac{R_N}{1 - \left[\frac{R_N}{F_N}\right]} \right] \right\} \tag{23}$$

where α is shown as a function of R_N since α depends on the value of $xy(R_N)$. Combining Eqs. (15), (16), and (23), we obtain

$$\mathrm{CUMSNR}(R_N) = \frac{\alpha(R_N) + \tan^{-1}\left[\frac{R_N}{1 - \left[\frac{R_N}{F_N}\right]} \right]}{\frac{\pi}{2} + \tan^{-1}\left[\frac{1}{F_N}\right]} \tag{24}$$

CUMSNR(R_N) should range from 0 to 1 as R_N goes from 0 to ∞. For very small R_N, $xy(R_N) \sim F_N^{-2}$, $\alpha = 0$, and CUMSNR(0) = 0. For very large R_N, $\alpha = \pi$, and using

$$\tan^{-1}(-z) = -\frac{\pi}{2} + \tan^{-1}\left(\frac{1}{z}\right) \tag{25}$$

for $z > 0$, we find CUMSNR(∞) = 1, as expected.

Figure 1 shows CUMSNR vs normalized range R_N for normalized focal ranges F_N of 0.1, 0.5, 1, 5, and 10. The range at which CUMSNR = 0.5, the 50th percentile range R_N(50%), is always smaller than F_N, with the difference increasing with increasing F_N. (Inclusion of atmospheric extinction and refractive turbulence in the theory would increase the difference between R_N(50%) and F_N.) The range resolution, e.g., the range interval over which cumulative SNR increases from 5% to 95%, increases with increasing values of F_N. Note that for some values of R_N, the cumulative SNR does not monotonically decrease with increasing values of F_N. The curves may be translated into actual range R and focal range F values through knowledge of the Rayleigh range R_R of a particular laser radar system.

6. Percentile Ranges and Range Resolution

As stated in the introduction, we would like to know the range to any percentile of the SNR. For a desired value of CUMSNR(R_N), e.g., 5%, 25%, 50%, 75%, 95%, etc., Eq. (24) may be inverted to solve for R_N:

$$R_N(\text{CUMSNR}) = \frac{F_N \tan\gamma}{F_N + \tan\gamma} \tag{26}$$

where the angle γ [rad] is given by

$$\gamma = (\text{CUMSNR}) \left[\pi - \tan^{-1} F_N\right] \tag{27}$$

Eqs. (26) and (27) are an analytic solution for R_N(CUMSNR).

Figure 2 shows five normalized percentile ranges R_N plotted vs normalized focal range F_N. The R_N(95%) curve (dashed line) is shown divided by 10 to fit on the plot. Note the spread of curves once the focal range F exceeds the Rayleigh range R_R (i.e., $\log_{10} F_N > 0$). R_N becomes equal to F_N for small F_N. For large F_N, R_N becomes independent of F_N and equal to tan(π CUMSNR/2).

The normalized range resolution of the CW focused CLR measurement might be defined as the distance between two particular normalized percentile ranges R_N. For example, the normalized 50% range resolution (dimensionless) would be

$$W_N(50\%) \triangleq R_N(75\%) - R_N(25\%) \tag{28}$$

and the normalized 90% range resolution would be

$$W_N(90\%) \triangleq R_N(95\%) - R_N(5\%). \tag{29}$$

In general, we may use Eqs. (26) and (27) to calculate

$$W_N(1 - 2\epsilon) = \frac{2\left[1 + \frac{F_N}{\tan 2\delta}\right]}{\left[F_N + \frac{1}{F_N}\right]\left[1 + \frac{\tan\delta}{F_N}\right]} \tag{30}$$

where the angle δ [rad] is

$$\delta = \epsilon(\pi - \tan^{-1}F_N) \tag{31}$$

and $0 < \epsilon < 0.5$ [dimensionless]. The normalized range resolution for any percentile of the signal is solved analytically. For $W_N(50\%)$, we insert $\epsilon = 0.25$, etc. For small values of F_N, Eqs. (30) and (31) become

$$W_N(1 - 2\epsilon) \approx \frac{2\,F_N^2}{\tan(\pi\epsilon)}\,, \tag{32}$$

and for large F_N,

$$W_N(1 - 2\epsilon) \approx \frac{2}{\tan(\pi\epsilon)}\,. \tag{33}$$

Note that $W(50\%) = R_R\,W_N(50\%)$ [m] which equals $2F^2R_R^{-1}$ and $2R_R$ for the tight focus and collimated cases, respectively.

As with R_N, W_N becomes independent of F_N for large F_N. However, for small F_N, W_N is proportional to F_N^2. Figure 3 plots $W_N(50\%)$, $W_N(60\%)$, $W_N(70\%)$, $W_N(80\%)$, and $W_N(90\%)$ vs normalized focal range F_N. As predicted by Eq. (33) for large F_N, Figure 3 shows $W_N(50\%) = 2$ when $F_N = 100$.

7. Tight Focus Case

We now examine the special case of a tight focus, i.e., F_N

<< 1. In most cases we can set $\alpha = \pi$. Under these assumptions Eq. (24) becomes

$$\mathrm{CUMSNR}(R_N) = \frac{\pi + \tan^{-1}\left[\dfrac{F_N R_N}{F_N - R_N}\right]}{\pi - F_N} \tag{34}$$

Inverting Eq. (34) we find

$$R_N(\mathrm{CUMSNR}) = \frac{F_N \tan(\pi\mathrm{CUMSNR})}{F_N + \tan(\pi\mathrm{CUMSNR})} \tag{35}$$

We may also obtain Eq. (35) from Eqs. (26) and (27). Letting CUMSNR = 0.5 we obtain $R_N(50\%) = F_N$ or $R(50\%) = R_R R_N(50\%) = F$, as expected. Half of the SNR is due to ranges from 0 to the focal range F. Similarly, we can calculate

$$R(25\%) \approx F(1 - F_N) = F - \frac{F^2}{R_R} \tag{36}$$

$$R(75\%) \approx F(1 + F_N) = F + \frac{F^2}{R_R} \tag{37}$$

Using Eqs. (36) and (37), or Eq. (32), we also find

$$W(50\%) = R(75\%) - R(25\%) = 2FF_N = \frac{2F^2}{R_R} = \frac{8\lambda F^2}{\pi D_o^2} \tag{38}$$

This answer matches the results of others[3,16] who assumed tight focusing and calculated the distance between ranges where the SNR fell to half of its peak value. However, Eqs. (26) and (27) are valid under any focusing conditions and for any definition of the CW laser radar range resolution. It is interesting to note that for the tight focusing case W(50%) can, through the use of Eq. (43), be written as

$$W(50\%) = 2\ \frac{\pi D_{min}^2}{4\lambda} \tag{39}$$

which is just twice the Rayleigh range of the focused spot [see Eq. (2)]. Also, the product of W(50%) and the receiver solid angle is simply 2λ, independent of focal range.[12] This is interesting since the SNR is approximately proportional to the product of the interaction length, W(50%), the receiver solid angle, and β.

8. Beam Diameter

Calculations of the behavior of the beam diameter are necessary for the measurement volume calculations in Sections 9 and 10. The e^{-2} intensity diameter [m] of the beam at any range is[19]

$$D(R) = D_o\left[\left[1 - \frac{R}{F}\right]^2 + R_N^2\right]^{1/2} \tag{40}$$

At the focal range, $R = F$ or $R_N = F_N$, the beam diameter is

$$D(F) = \frac{4\lambda F}{\pi D_o} = \frac{D_o F}{R_R} = D_o F_N \tag{41}$$

The e^{-2} intensity diameter at the beam waist (peak SNR) position, $R = R_P$, is

$$D(R_P) = D_{min} = \frac{D_o}{\left[1 + (\frac{1}{F_N})^2\right]^{1/2}}, \tag{42}$$

For a tight focus ($F_N << 1$)

$$D_{min} \approx D_o F_N \tag{43}$$

which is identical to D(F) since $R_P \approx F$. The tight focus beam waist is simply the transmitted beam diameter multiplied by the normalized focal range. For the large F ($F_N >> 1$) case

$$D_{min} \approx D_o, \qquad (44)$$

which together with Eq. (7) implies that the beam waist occurs at the transmitter and that the beam gets larger with increasing range.

9. Measurement Volume

The e^{-2} intensity diameter of the Gaussian beam at any range, D(R), is given by Eq. (40). The measurement volume V [m^3] may be found by integrating elements of volume $dV = \pi D^2(R)dR/4$ from a lower range limit RL to an upper range limit, RU:

$$V = \frac{\pi}{4} \int_{RL}^{RU} D^2(R)dR = \frac{\pi D_o^2}{4} \int_{RL}^{RU} \left[\left[1 - \frac{R}{F}\right]^2 + \left[\frac{R}{R_R}\right]^2\right] dR$$

$$= \frac{\pi D_o^2}{4} \left[(RU-RL) - \frac{1}{F}\left[RU^2-RL^2\right] + \frac{1}{3}\left[\frac{1}{F^2} + \frac{1}{R_R^2}\right]\left[RU^3-RL^3\right]\right] \qquad (45)$$

We define V(50%) as the measurement volume calculated with RL = R(25%) and RU = R(75%), and therefore as the measurement volume from which 50% of the SNR arises. Plots of the 50% and 90% measurement volumes will be given in the next section. Inserting Eqs. (26) and (27) for RU and RL into Eq. (45) leads to an analytic expression for V, which is quite complicated. We can, however, make a rough estimate of V(50%) for the tight focusing case. We have shown that the 50% range resolution in this case is $W(50\%) = 2FF_N$ [see Eq. (38)]. An approximate volume can be calculated by taking the volume element as a cylinder of this length and with a diameter $D = D_oF_N$. Since at the extremes of the true volume element the beam diameter will be $\sqrt{2}$ larger, this estimate will be less than a factor of 2 too small. The volume of this cylinder can then be written as

$$V(50\%) \approx \frac{32}{\pi^2} \frac{\lambda^3 F^4}{D_o^4} \quad (46)$$

From this expression we see that in the tightly focused case, the 50% contributing volume is proportional to the optical wavelength cubed and to the fourth power of the focal range. It is inversely proportional to the fourth power of the laser radar beam diameter. This rapid decrease in V for smaller λ and F values, and for larger D_o values may be a very important consideration in cases where aerosol densities are low, such as at high altitudes.

We find it interesting to note that, as far as we can determine, there exists no "natural" volume to which the calculated volumes can be normalized. The parameters R and F can be normalized to the Rayleigh range R_R, whereas volumes cannot.

10. Example Plots

The equations and plots of normalized parameters provided so far will allow investigators to characterize their specific laser radar system over a wide span of parameter values. Familiarity and intuition can be gained from examining unnormalized parameter plots for a specific laser radar system. We will examine the case of the NASA-Marshall Space Flight Center (MSFC) monostatic CLR system[11,13] that has recently made two Pacific ocean basin survey flights on the NASA DC-8 aircraft for the purpose of measuring the atmospheric aerosol backscatter coefficient β as part of NASA's Global Backscatter Experiment (GLOBE). The laser radar's parameters were approximately $\lambda = 9.13\ \mu m$, $D_o = 6$ cm, and F = 50 m; resulting in a Rayleigh range of 309.7 m.

Figure 4 shows relative SNR vs range R for six settings of the focal range F [see Eq. (1)]. Close examination shows that the peak SNR occurs at the greatest range when $F = R_R = 309.7$ m, and is located at $R_R/2$, as expected. The curves were normalized to have a value of 1 at R = 0. The normalization constant involves only D_o and λ, but not F.

Figure 5 plots CUMSNR vs range R for focal ranges F of 50, 100, 200, 400, and 1000 m. Eq. (24) is employed with $R = R_R R_N$ and $F = R_R F_N$. These curves correspond to five of the six curves in Figure 4. Even when focused at 50 m, at least 1% of the signal comes from ranges greater than 250 m. Therefore, a cloud or other object located at $R \lesssim 250$ m, with a backscatter coefficient 10 or more times greater than the aerosol backscatter coefficient, will cause errors of 10% or more.

Figure 6 shows percentile ranges R(x), for x = 5%, 25%, 50%, 75%, and 95%, as a function of focal range F [see Eqs. (26) and (27)]. The maximum plotted focal range of 200 m is still smaller than the Rayleigh range of 309.7 m. Therefore, Figure 6 corresponds to the left half of Figure 2. Figure 7 gives the range resolution for the "center" 50% of the signal, W(50%) = R(75%) - R(25%), and also the range resolutions W(60%), W(70%), W(80%), and W(90%) vs focal range F. It corresponds to the left half of Figure 3. Figure 8 plots the same five range resolutions W vs diameter D_o when F = 50 m. The largest values of W (poorest range resolution) occur for $D_o \sim 2$ cm. The existence of a diameter giving the poorest range resolution is perhaps not at first obvious, but it can be explained as follows. For very small diameters D_o, the beam will diffract quickly and hence as $D_o \to 0$, the range contributing to SNR also goes to zero. For large D_o, the beam can be focused tightly, and as $D_o \to \infty$ the beam waist diameter approaches zero, and hence the contributing range again approaches zero. Between these two extremes lies an area where the range resolution W must be nonzero, and as a result, a maximum must exist. Figure 9 plots five percentile ranges vs diameter. The smallest percentile ranges appear monotonic for this excursion of diameter values, while the largest percentile ranges exhibit a peak. Therefore, the range resolution peaking observed in Figure 8 is due to the larger percentile ranges. Similar plots for F = 200 m show the poorest range resolution (largest W) occuring at $D_o \sim 5$ cm. For very small values of D_o, both the percentile ranges R and the range resolutions W are proportional to D_o^2. For large D_o, the percentile ranges R become independent of D_o and converge to the value of F, and the widths W become proportional to D_o^{-2}. This is consistent with the small and large F_N behavior discussed earlier, since that corresponds to large and small D_o behavior, respectively.

Using Eq. (45), Figure 10 presents V(50%) vs focal range F for diameter D_o values of 2, 4, 6, 8, and 10 cm. For F = 50 m and D_o = 6 cm, V(50%) $\approx 10^{-3}$ m^3. Figure 11 shows the corresponding values of V(90%). For F = 50 m and D_o = 6 cm, V(90%) $\approx 7\ 10^{-2}$ m^3, or a factor of 70 larger than V(50%). For small values of F, the larger values of D_o have smaller measurement volumes due to greater focusing efficacy. The situation is reversed for large values of F; larger values of D_o have larger measurement volumes, since the beams are approximately collimated. Figures 12 and 13 plot V(50%) and V(90%) vs diameter D_o for values of focal range F of 10, 100, 1000, and 10,000 m. The measurement volumes peak for some diameter D_o depending on F and λ. Both V(50%) and V(90%) appear to peak at the same value of D_o. We suspect that the diameter yielding the maximum measurement volume is the same as that yielding the largest (poorest) range resolution (see Fig. 8). For the special case of a tightly focused beam, one can make rough estimates of the ratio V(90%)/V(50%). Such estimates show that the ratio is approximately 100. Numerical calculations bear this out, and in addition, show that the ratio stays in the very narrow range of 50-100 for <u>all</u> values of F and D_o shown in Figures 10-13. While it appears difficult to prove this statement analytically, it is nevertheless an interesting result. Figures 10-13 exhibit a large dynamic range of measurement volumes.

11. Conclusions

The CW laser radar SNR changes by only a factor of 2 due to beam diameter and focal range, and is proportional to $\beta\lambda^3$. General analytic expressions were derived for the cumulative SNR vs range, for the range to a given value of cumulative SNR, for the range resolution of the measurement given any definition of it in terms of percentile ranges, and for the measurement volume. The equations are valid for any parameters of the CW laser radar. Plots were presented in normalized parameters to cover a large portion of parameter space, and in unnormalized parameters for a specific example to gain familiarity with, and intuition from the curves. The behavior of the measurement volume vs focal range and beam diameter was plotted. The ratio of the volume containing 90% of the signal to the volume containing 50% stays in the narrow span of 50 to 100. Both the range resolution and the measurement volume peak for a certain diameter value. The measurement volumes vary over a large dynamic range. The question of whether small or large values of range resolution and measurement volume are desired depends on the specific application of the focused CW laser radar system.

12. Acknowledgments

We acknowledge many helpful technical discussions with Sammy W. Henderson. Computer programming support was provided by Dan B. Austin, A. Vincent Huffaker, and Mark H. Layne. This work was partially supported by NASA Marshall Space Flight Center contract NAS8-37580 (William D. Jones, technical monitor), Boeing Aerospace contract LJ6568 (J. Doyle McClure, technical monitor), and Rockwell International contract POL8GDQ-999977M (John J. Wang, technical monitor).

13. References

1. R.M. Huffaker, "Laser Doppler Detection Systems for Gas Velocity Measurement," Appl. Opt. 9(5), 1026-1039 (1970).
2. A.J. Hughes, J. O'Shaughnessy, E.R. Pike, A. McPherson, C. Spavins, and T.H. Clifton, "Long range anemometry using a CO_2 laser," Opto-electronics 4, 379-384 (1972).
3. T.R. Lawrence, D.J. Wilson, C.E. Craven, I.P. Jones, R.M. Huffaker, and J.A.L. Thomson, "A Laser Velocimeter for Remote Wind Sensing," Rev. Sci. Instrum. 43(3), 512-518 (1972).
4. R. Foord, R. Jones, W.R.M. Pomeroy, J.V. Vaughan, and D.V. Willetts, "Infrared laser velocimetry," Proc. SPIE 197, Modern Utilization of Infrared Technology, 325-328 (1979).
5. J.W. Bilbro, "Atmospheric laser Doppler velocimetry: an overview," Opt. Engr. 19(4), 533-542 (1980).

6. F. Kopp, R.L. Schwiesow, and C. Werner, "Remote Measurements of Boundary-Layer Wind Profiles Using a CW Doppler Lidar," J. Climate and Appl. Meteorol. 23(1), 148-154 (1984).
7. R.M. Munoz, H.W. Mocker, and L. Koehler, "Airborne Laser Doppler Velocimeter," Appl. Opt. 13(12), 2890-2898 (1974).
8. A.A. Woodfield and J.M. Vaughan, "Airspeed and Wind Shear Measurements with an Airborne CO_2 CW Laser," International J. of Aviation Safety 1, 207-224 (1983).
9. L.Z. Kennedy and J.W. Bilbro, "Remote measurement of the transverse wind velocity component using a laser Doppler velocimeter," Appl. Opt. 18(17), 3010-3013 (1979).
10. R.M. Huffaker, A.V. Jelalian, and J.A. Thomson, "Laser-Doppler System for Detection of Aircraft Trailing Vortices," Proc. IEEE 58(3), 322-326 (1970).
11. W.D. Jones, J.W. Bilbro, S.C. Johnson, H.B. Jeffreys, L.Z. Kennedy, R.W. Lee, and C.A. DiMarzio, "Design and calibration of a coherent lidar for measurement of atmospheric backscatter," Proc. SPIE 300, Physics and Technology of Coherent Infrared Radar, 66-71 (1981).
12. R.L. Schwiesow, R.E. Cupp, V.E. Derr, E.W. Barrett, R.F. Pueschel, and P.C. Sinclair, "Aerosol Backscatter Coefficient Profiles Measured at 10.6 μm," J. Appl. Meteorology 20(2), 184-194 (1981).
13. J.L. Gras and W.D. Jones, "Australian aerosol backscatter survey," Appl. Opt. 28(5), 852-856 (1989).
14. S.B. Alejandro, G.G. Koenig, J.M. Vaughan, and P.H. Davies, "SABLE: A South Atlantic Aerosol Backscatter Measurement Program," Bull. Amer. Meteorol. Soc. 71(3), 281-287 (1990).
15. M.J. Post, R.L. Schwiesow, R.E. Cupp, D.A. Haugen, and J.T. Newman, "A Comparison of Anemometer- and Lidar-Sensed Wind Velocity Data," J. Appl. Meteorol. 17(18), 1179-1181 (1978).
16. C. Werner, F. Kopp, and R.L. Schwiesow, "Influence of clouds and fog on LDA wind measurements," Appl. Opt. 23(15), 2482-2484 (1984).
17. R.L. Schwiesow and R.F. Calfee, "Atmospheric refractive effects on coherent lidar performance at 10.6 μm," Appl. Opt. 18(23), 3911-3917 (1979).
18. R.L. Schwiesow and R.E. Cupp, "Calibration of a cw infrared Doppler lidar," Appl. Opt. 19(18), 3168-3172 (1980).
19. R.G. Frehlich and M.J. Kavaya, "Coherent Laser Radar SNR Including Atmospheric Refractive Turbulence Using Path Integral Techniques," submitted for publication (1990).
20. A.E. Siegman, An Introduction to Lasers and Masers, pp. 310-314, McGraw-Hill, New York (1971).
21. J.W. Goodman, Introduction to Fourier Optics, p. 61, McGraw-Hill, San Francisco (1968).
22. C.M. Sonnenschein and F.A. Horrigan, "Signal-to-Noise Relationships for Coaxial Systems that Heterodyne Backscatter from the Atmosphere," Appl. Opt. 10(7), 1600-1604 (1971). A list of unpublished errata for this paper can be obtained from the present authors.
23. I.S. Gradshteyn and I.M. Ryzhik, Table of Integrals, Series, and Products, pp. 24, 49, and 68, Academic Press, New York (1965).

14. Figure Captions

Figure 1. Cumulative SNR vs normalized range as a function of normalized focal range.

Figure 2. Normalized percentile ranges vs normalized focal range. Note that $R_N(95\%)$ is divided by 10 and shown as a dashed line.

Figure 3. Normalized range resolutions vs normalized focal range.

Figure 4. Relative SNR vs range as a function of focal range. The SNR is normalized to 1 at R = 0.

Figure 5. Cumulative SNR vs range as a function of focal range.

Figure 6. Percentile ranges vs focal range.

Figure 7. Range resolution widths vs focal range.

Figure 8. Range resolution widths vs beam diameter.

Figure 9. Percentile ranges vs beam diameter.

Figure 10. V(50%) vs focal range as a function of beam diameter.

Figure 11. V(90%) vs focal range as a function of beam diameter.

Figure 12. V(50%) vs diameter as a function of focal range.

Figure 13. V(90%) vs diameter as a function of focal range.

Figure D-1

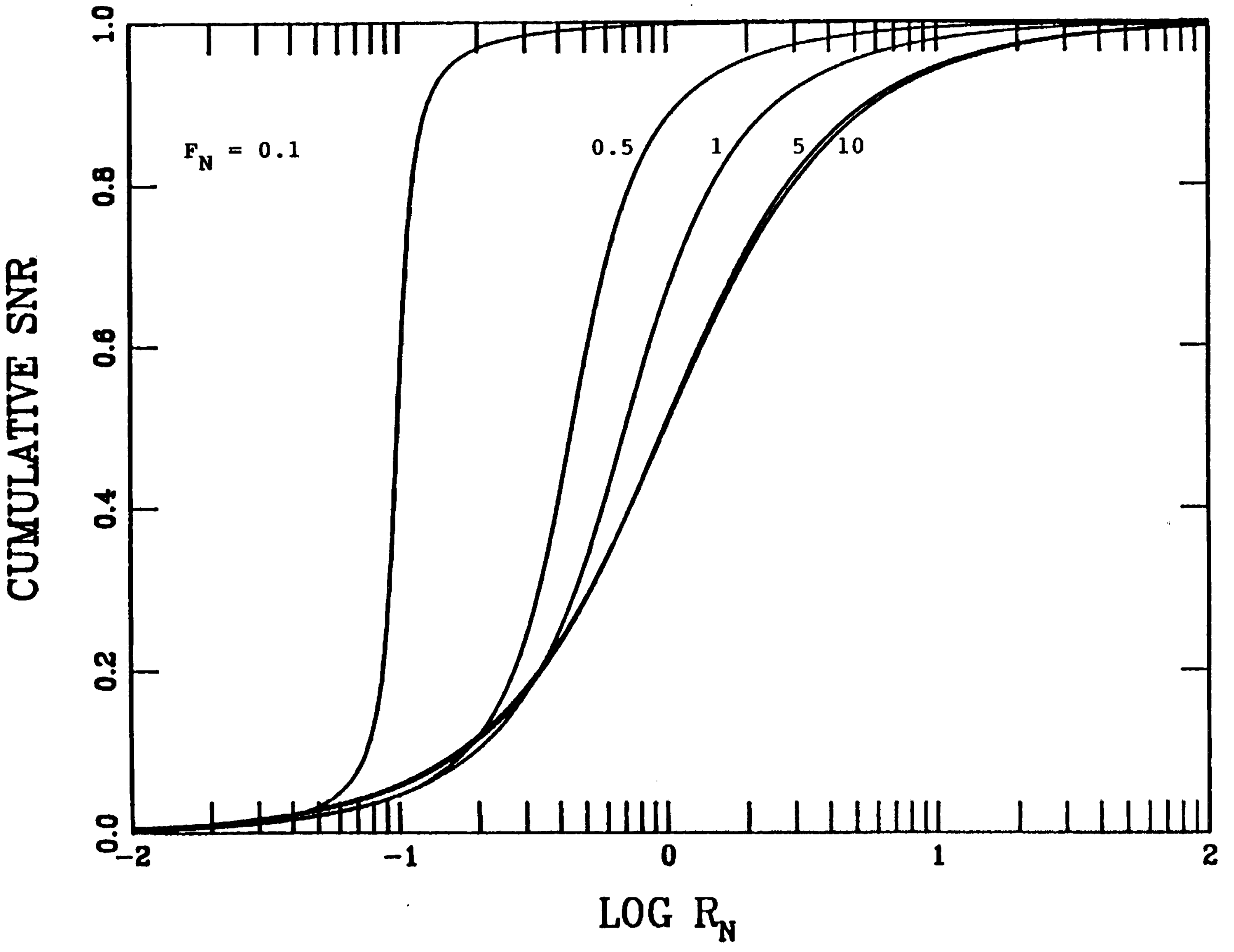

Figure D-2

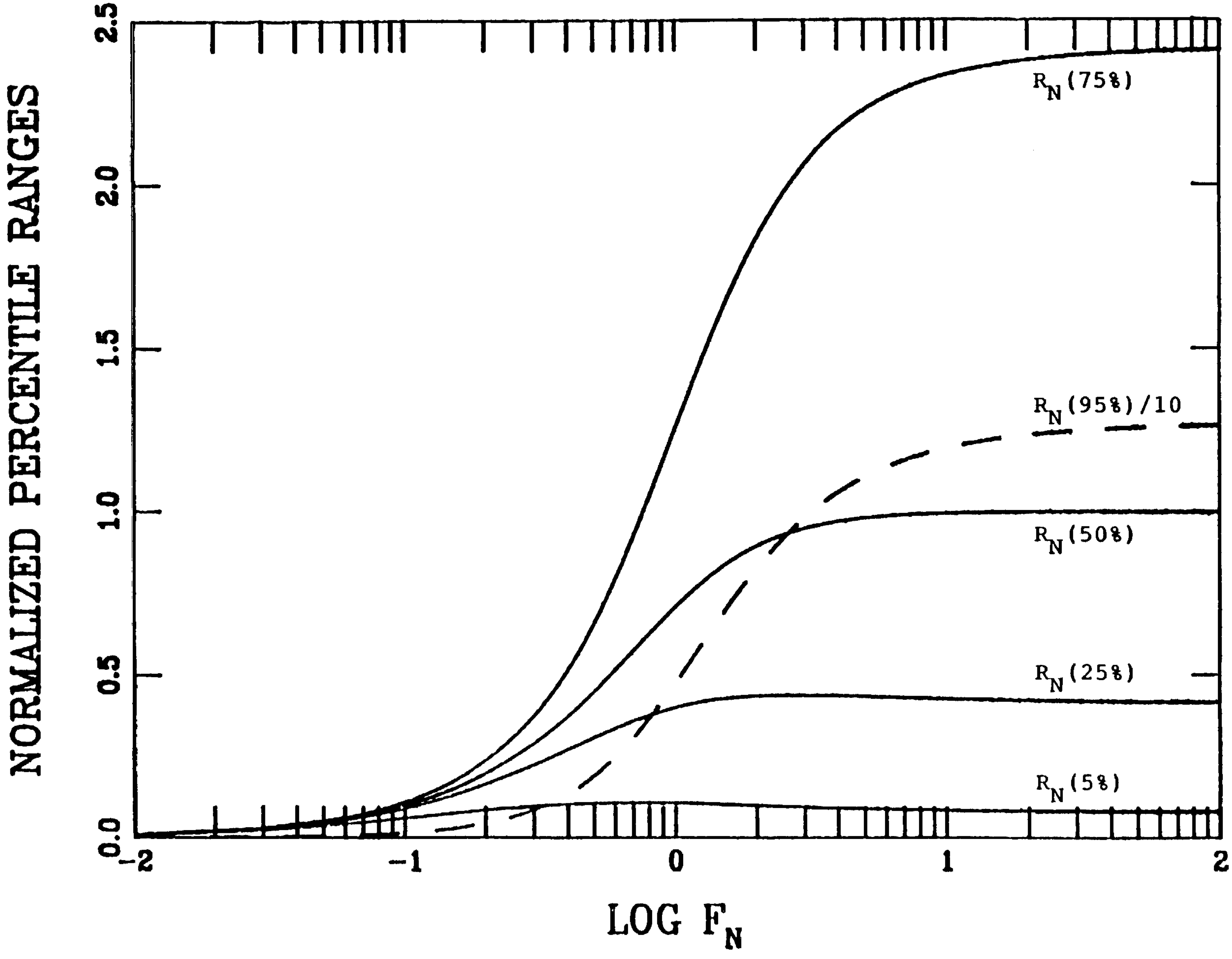

NORMALIZED PERCENTILE RANGES
0.0
0.5
1.0
1.5
2.0
2.5
-2
-1
0
1
2
LOG F_N
R_N(75%)
R_N(95%)/10
R_N(50%)
R_N(25%)
R_N(5%)

Figure D-3

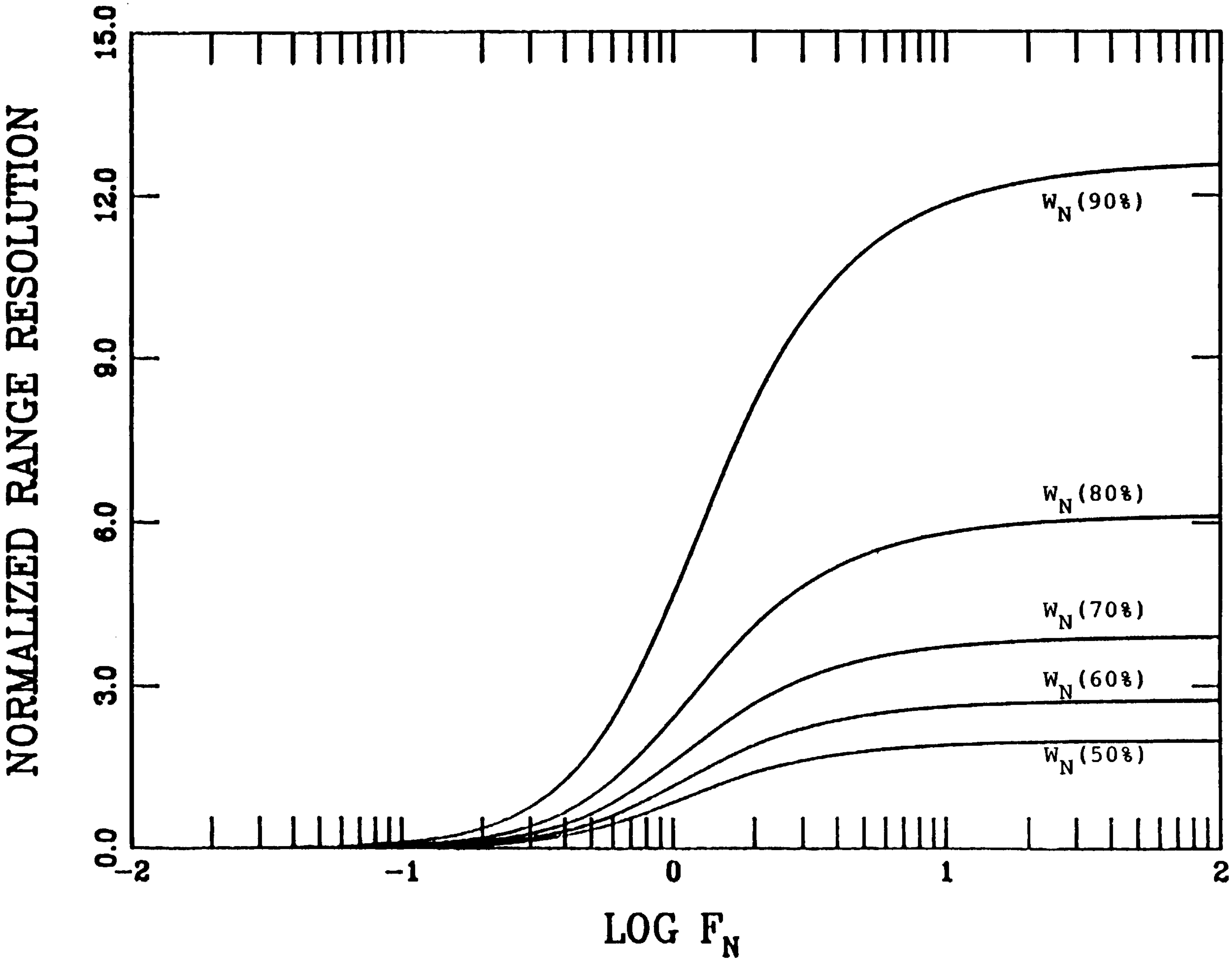
NORMALIZED RANGE RESOLUTION
0.0
3.0
6.0
9.0
12.0
15.0
LOG F_N
−2
−1
0
1
2
W_N(90%)
W_N(80%)
W_N(70%)
W_N(60%)
W_N(50%)

Figure D-4

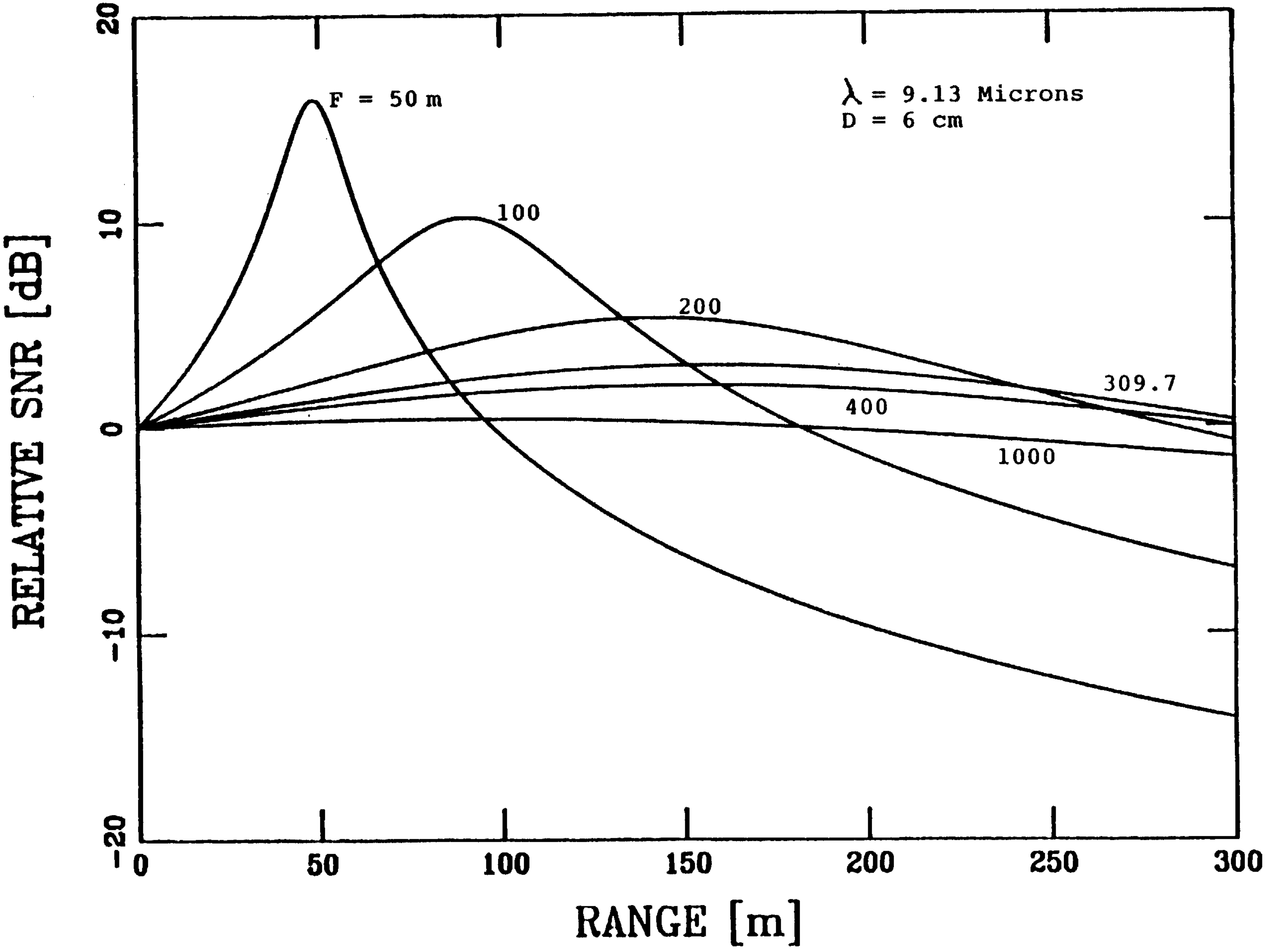
F = 50 m
100
200
309.7
400
1000
λ = 9.13 Microns
D = 6 cm
RELATIVE SNR [dB]
20
10
0
-10
-20
RANGE [m]
0
50
100
150
200
250
300

Figure D-5

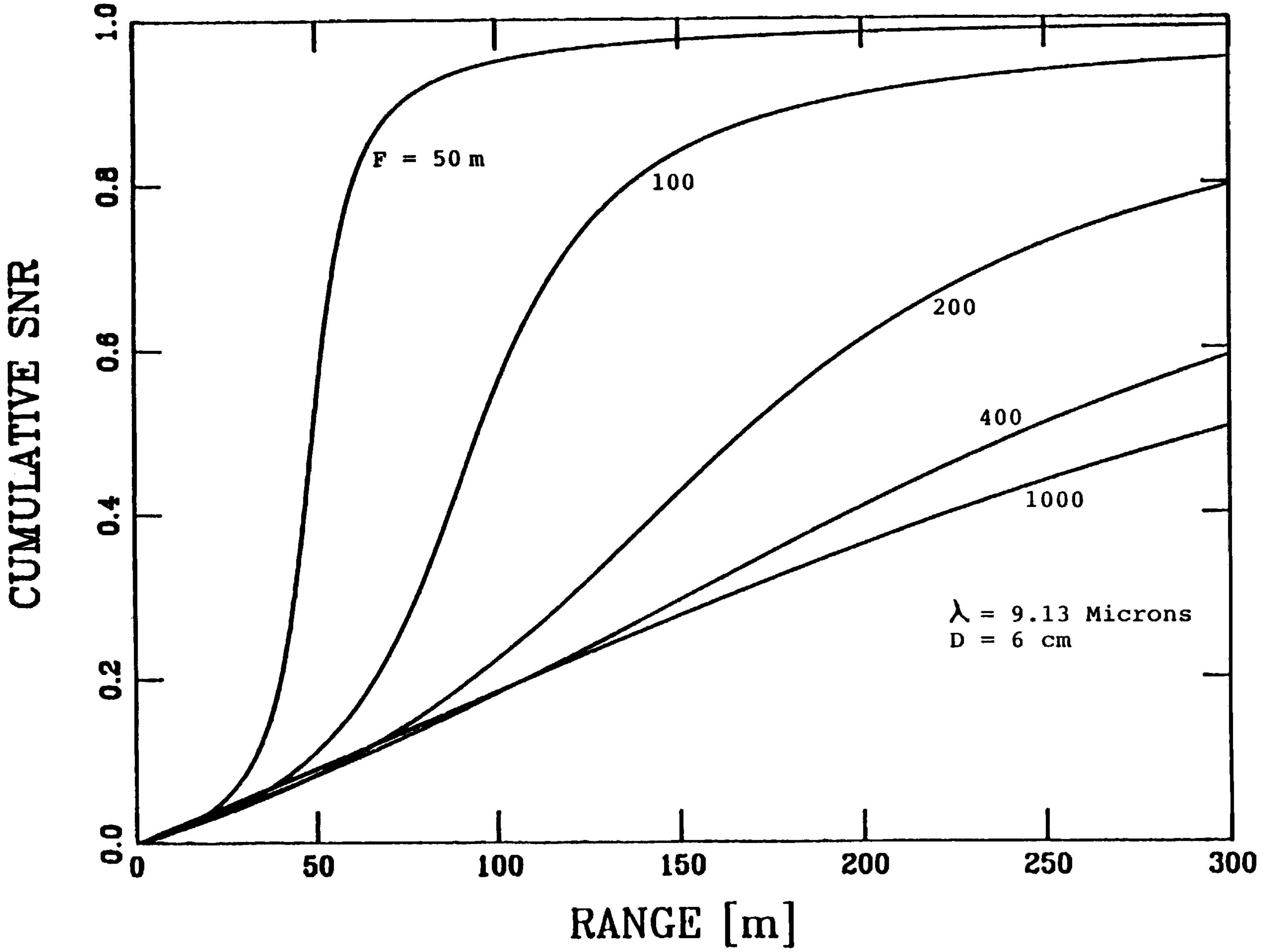
F = 50 m
100
200
400
1000
λ = 9.13 Microns
D = 6 cm
CUMULATIVE SNR
0.0
0.2
0.4
0.6
0.8
1.0
RANGE [m]
0
50
100
150
200
250
300

C-2

Figure D-6

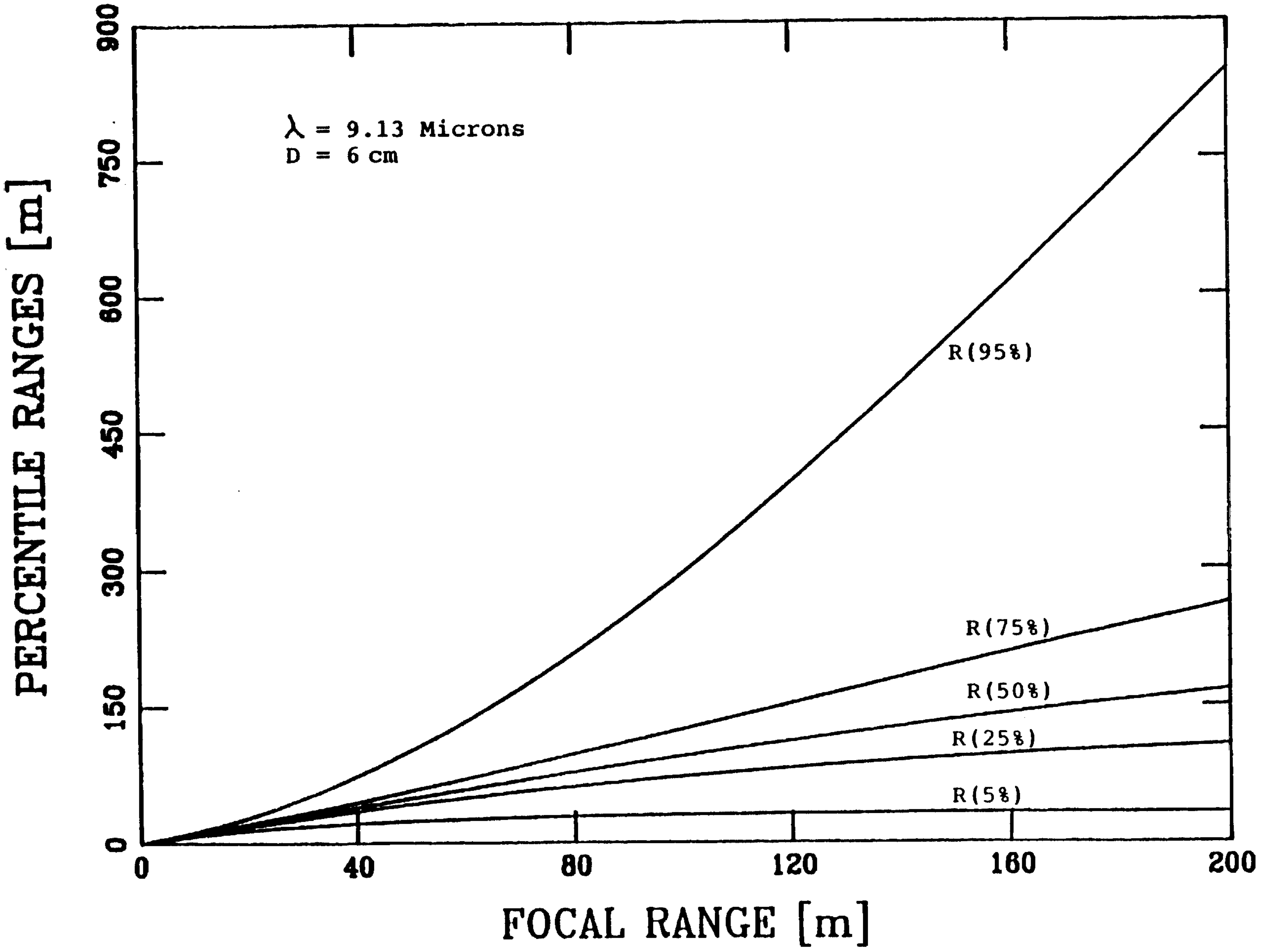
λ = 9.13 Microns
D = 6 cm
R(95%)
R(75%)
R(50%)
R(25%)
R(5%)
PERCENTILE RANGES [m]
0
150
300
450
600
750
900
FOCAL RANGE [m]
0
40
80
120
160
200

Figure D-7

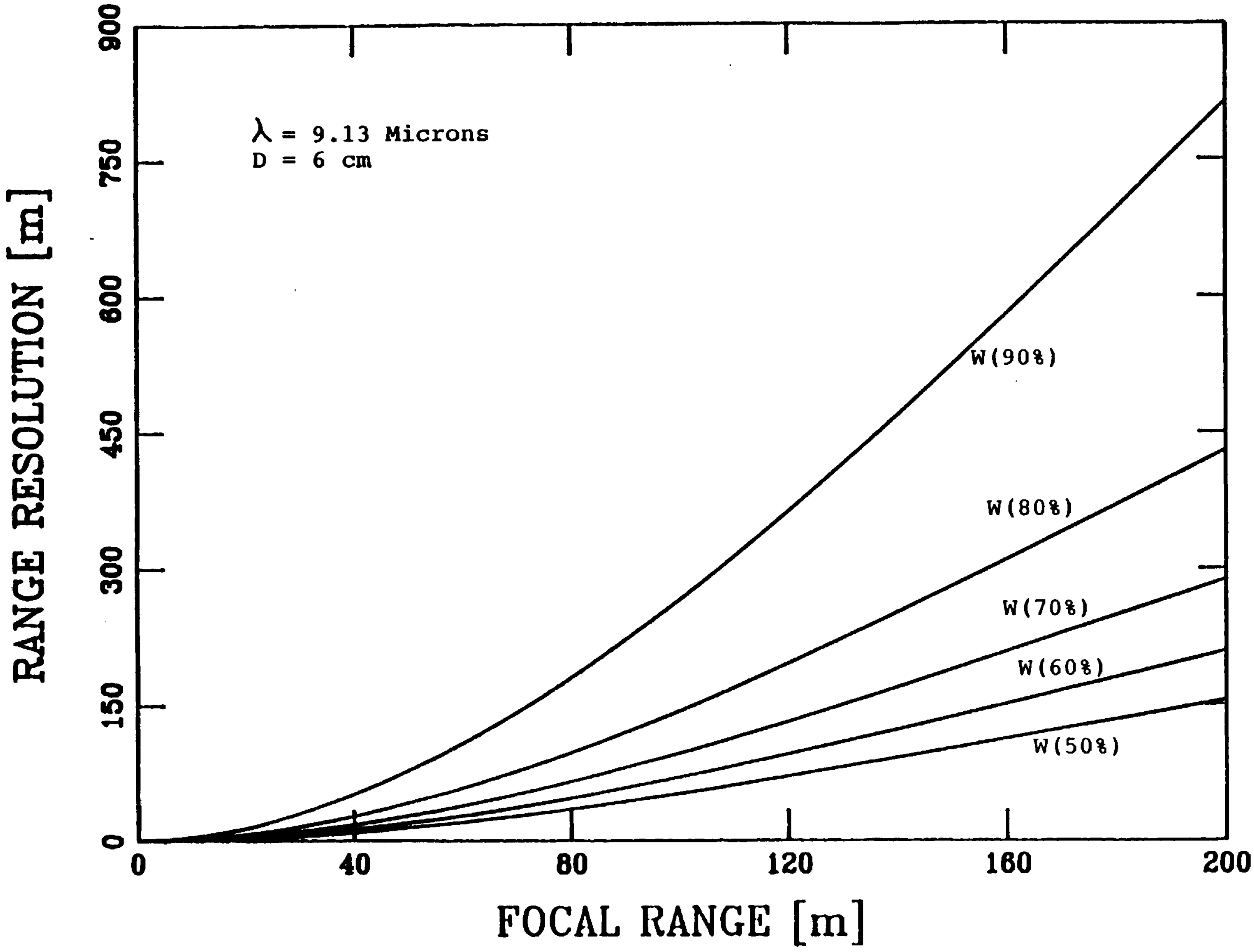
λ = 9.13 Microns
D = 6 cm
W(90%)
W(80%)
W(70%)
W(60%)
W(50%)
RANGE RESOLUTION [m]
0
150
300
450
600
750
900
FOCAL RANGE [m]
0
40
80
120
160
200

Figure D-8

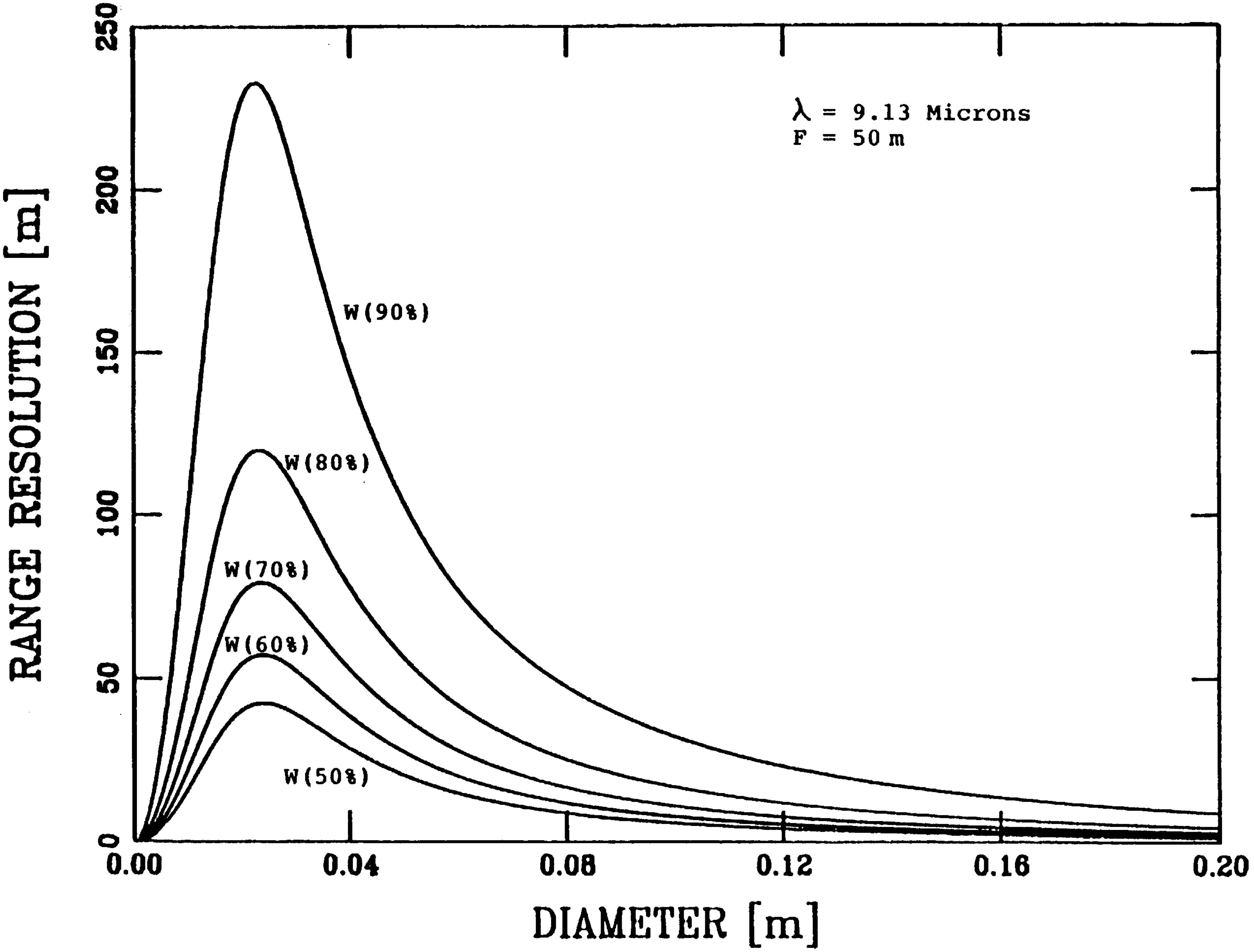
λ = 9.13 Microns
F = 50 m
W(90%)
W(80%)
W(70%)
W(60%)
W(50%)
RANGE RESOLUTION [m]
0
50
100
150
200
250
0.00
0.04
0.08
0.12
0.16
0.20
DIAMETER [m]

Figure D-9

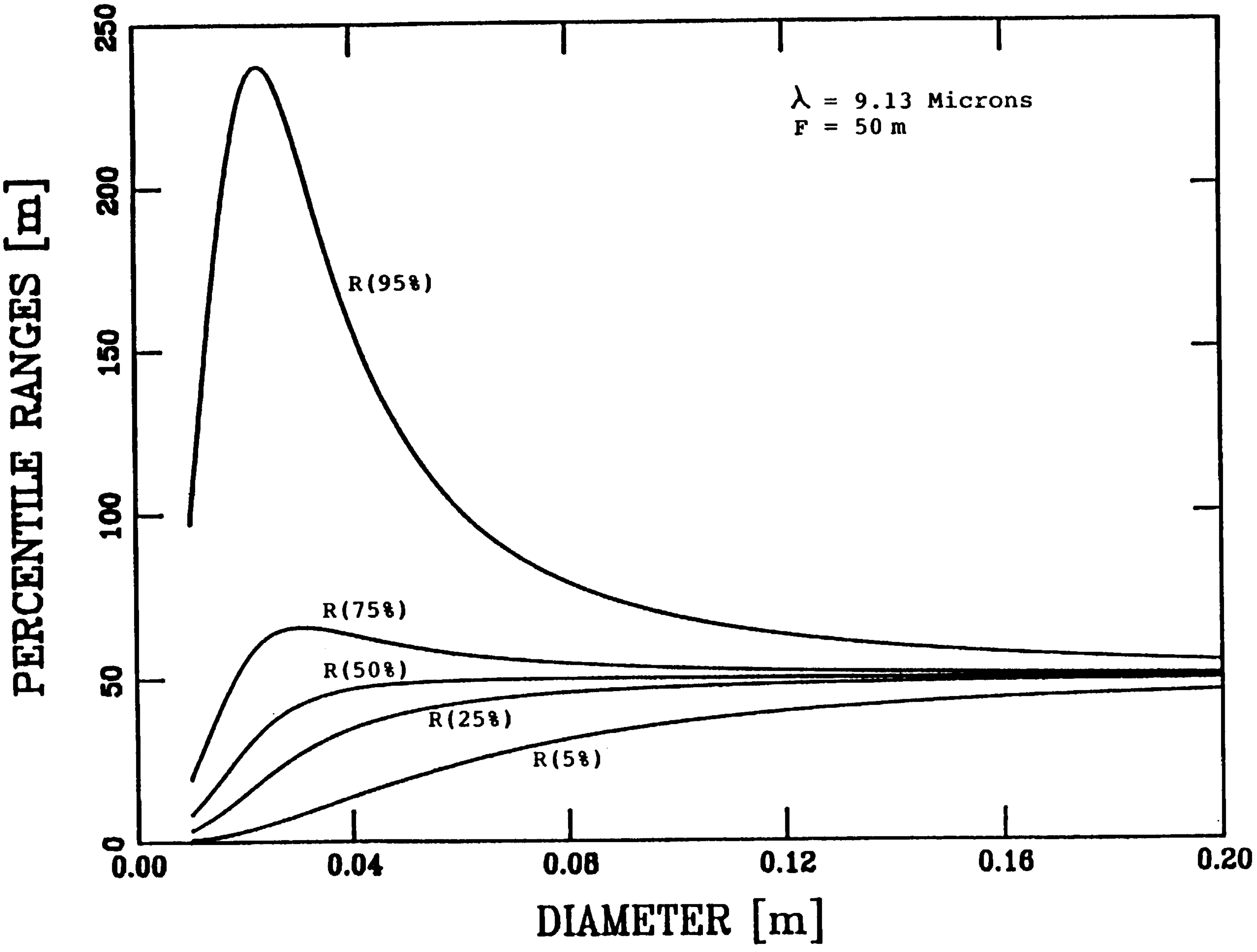
λ = 9.13 Microns
F = 50 m
R(95%)
R(75%)
R(50%)
R(25%)
R(5%)
PERCENTILE RANGES [m]
0
50
100
150
200
250
DIAMETER [m]
0.00
0.04
0.08
0.12
0.16
0.20

Figure D-10

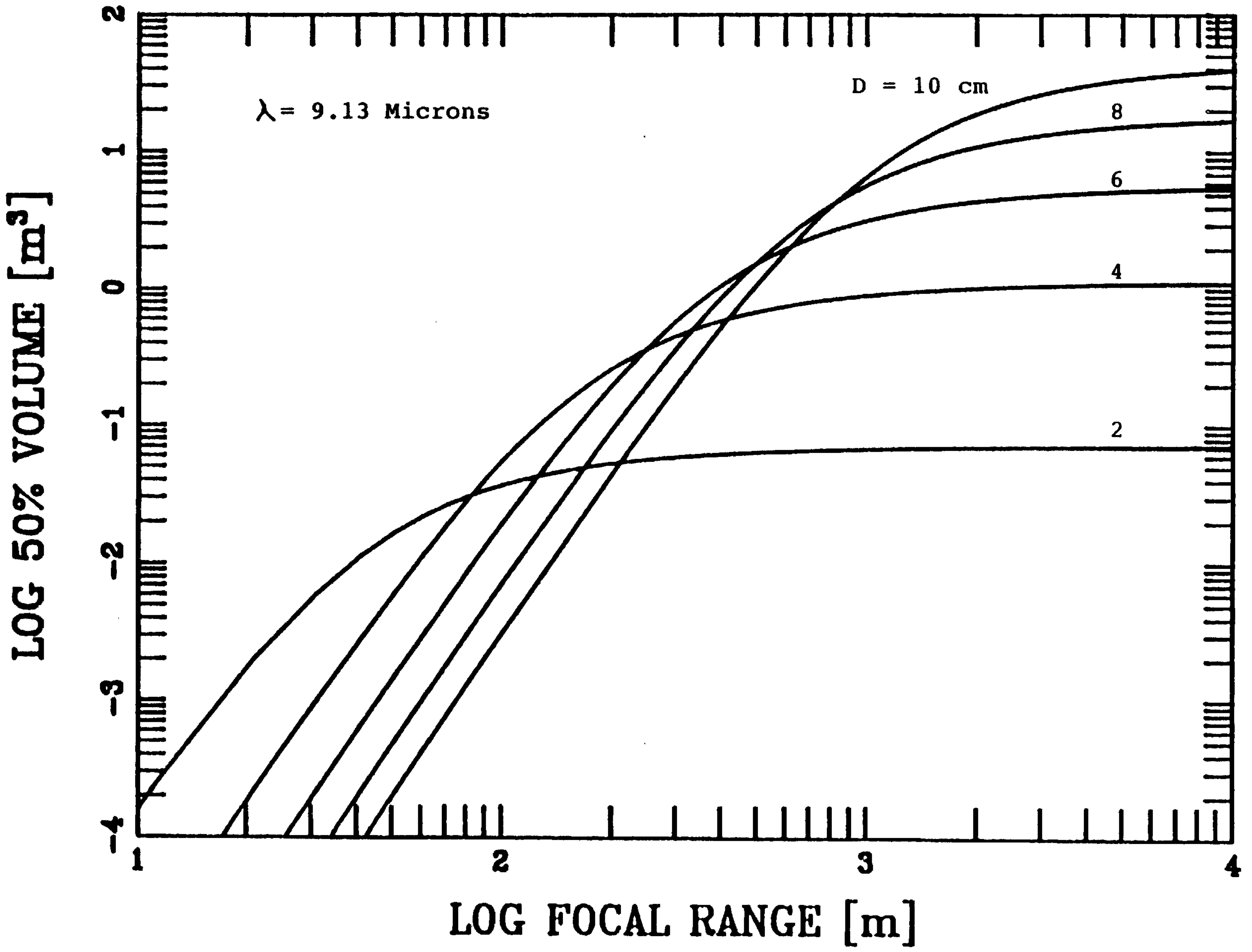
λ= 9.13 Microns
D = 10 cm
8
6
4
2
LOG 50% VOLUME [m³]
2
1
0
-1
-2
-3
-4
1
2
3
4
LOG FOCAL RANGE [m]

Figure D-11

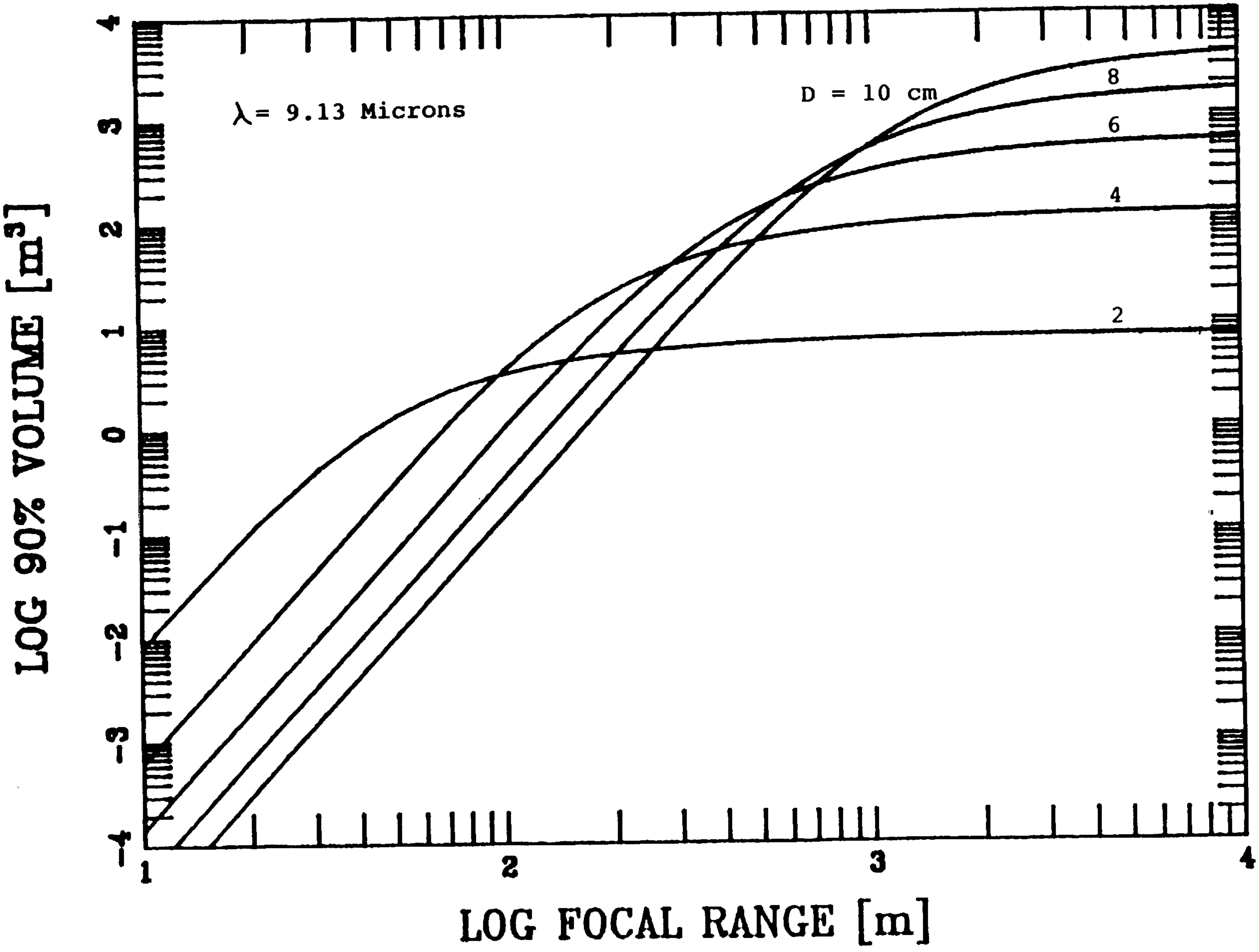
λ= 9.13 Microns
D = 10 cm
8
6
4
2
LOG 90% VOLUME [m^3]
4
3
2
1
0
-1
-2
-3
-4
LOG FOCAL RANGE [m]
1
2
3
4

Figure D-12

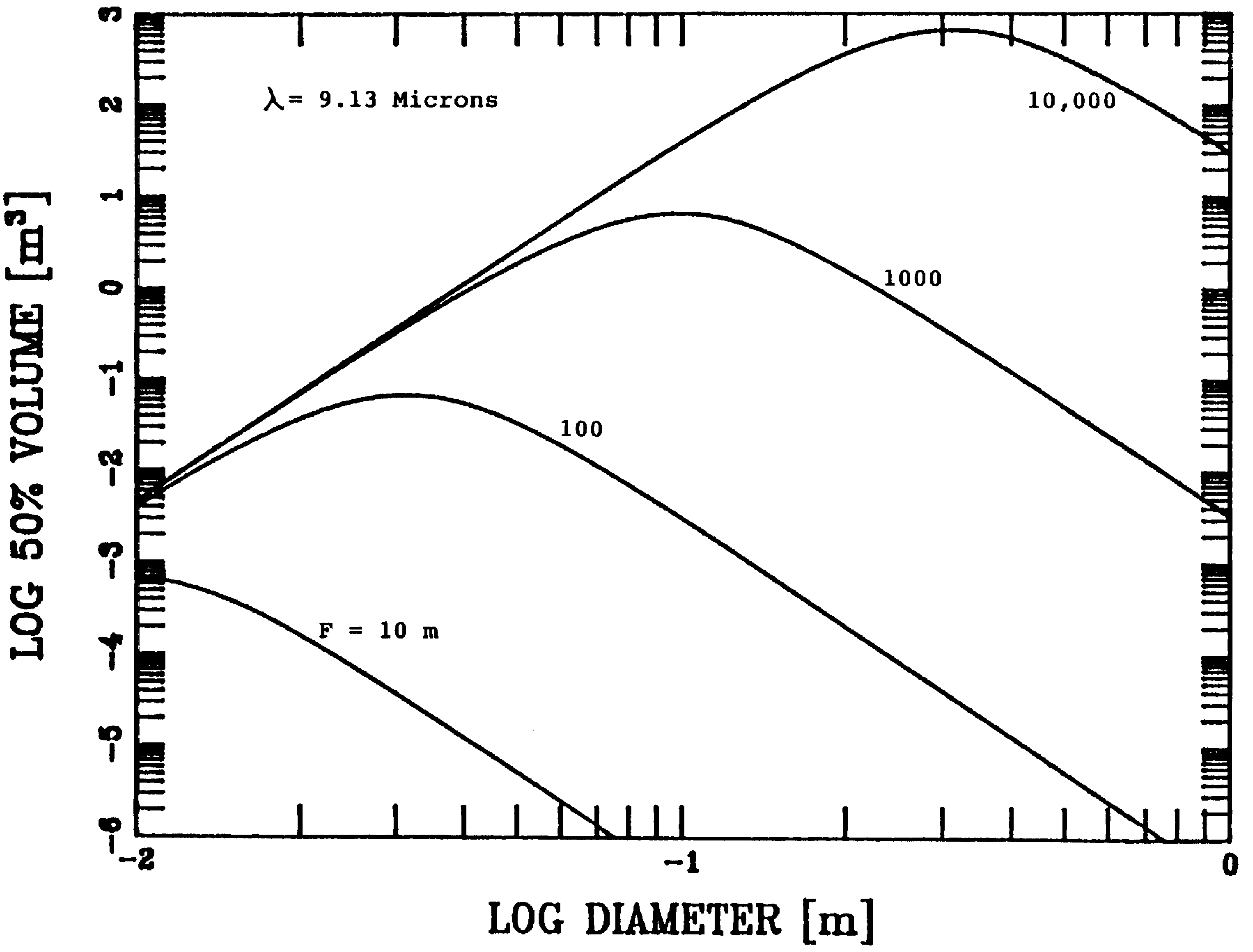
λ= 9.13 Microns
10,000
1000
100
F = 10 m
LOG 50% VOLUME [m^3]
LOG DIAMETER [m]
3
2
1
0
−1
−2
−3
−4
−5
−6
−2
−1
0

Figure D-13

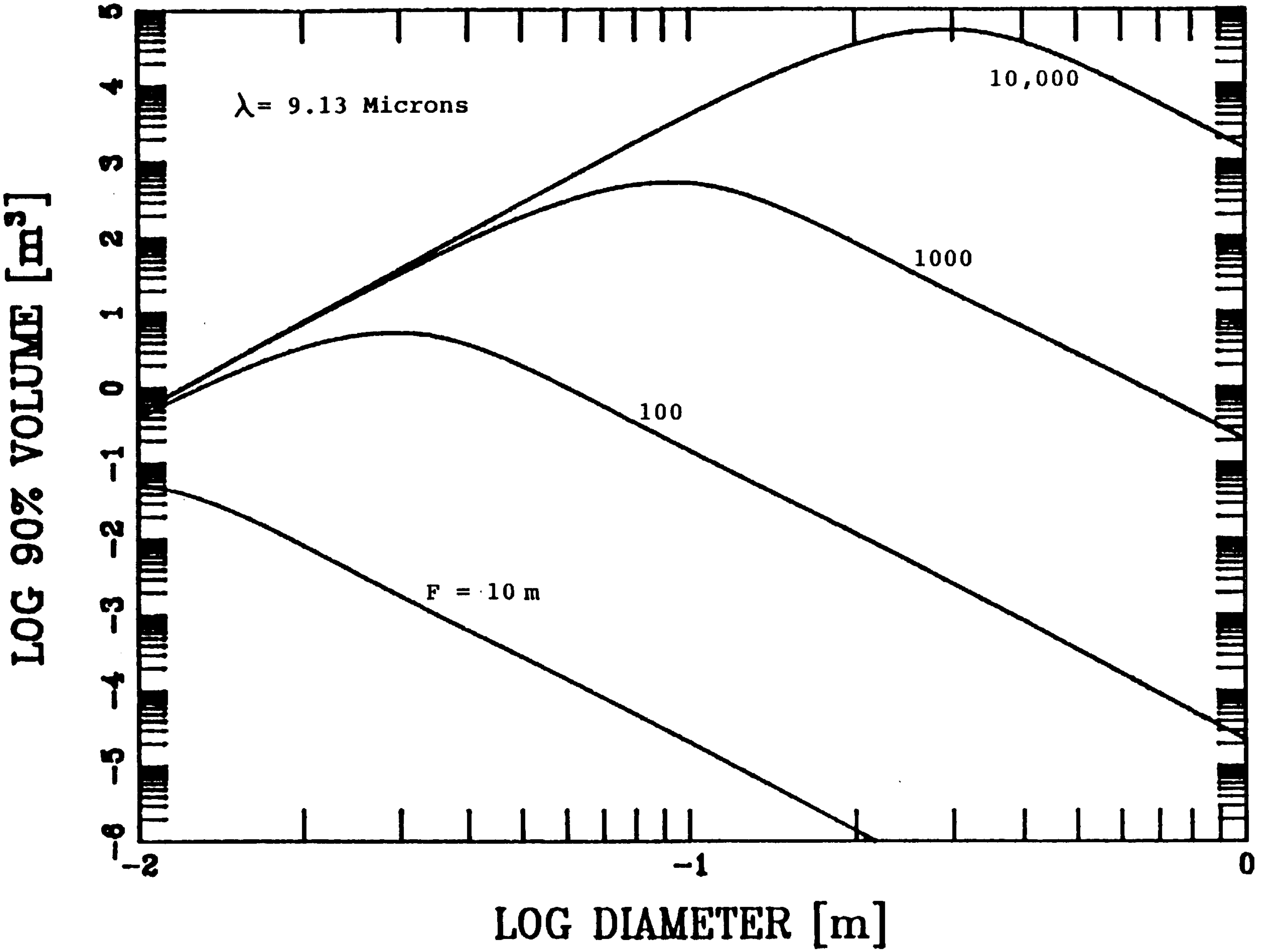
λ= 9.13 Microns
10,000
1000
100
F = 10 m
LOG 90% VOLUME [m^3]
5
4
3
2
1
0
−1
−2
−3
−4
−5
−6
−2
−1
0
LOG DIAMETER [m]

APPENDIX E

a reprint from Applied Optics

Tunable single-longitudinal-mode diode laser pumped Tm:Ho:YAG laser

Sammy W. Henderson and Charley P. Hale

Coherent Technologies, Inc., P.O. Box 7488, Boulder, Colorado 80306.

Received 2 October 1989
0003-6935/90/121716-03$02.00/0.

Continuous wave single-longitudinal-mode power of 58 mW and frequency tuning of ~1 THz has been obtained near 2.1 μm using a diode laser pumped thermoelectrically cooled Tm:Ho:YAG laser. Key words: *solid state lasers, single-frequency lasers, holmium lasers.*

Recent demonstrations of cw diode laser pumped thulium (Tm) and holmium (Ho) doped solid state lasers operating at wavelengths near 2 μm have shown that these lasers can operate efficiently at or near room temperature.[1-5] Fan *et al.*[2,3] first demonstrated cw room temperature operation of a diode laser pumped Tm:Ho:YAG laser, obtaining laser threshold with only 4.4 mW of absorbed pump power. Kintz *et al.*[4] demonstrated a slope efficiency of 56% in a room temperature cw diode laser pumped Tm:YAG laser and Kane and Wallace[5] demonstrated a slope efficiency of 58% in a cw diode laser pumped Tm:Ho:YAG laser cooled to −55°C. The long lifetime of the upper laser levels in Tm:YAG and Tm:Ho:YAG lasers make efficient energy storage for pulsed operation a possibility. Their emission wavelengths near 2 μm are eyesafe, making their use in applications requiring atmospheric propagation attractive. In this Letter we describe a tunable cw single-longitudinal-mode (SLM) Tm:Ho:YAG laser which is being developed as part of a 2.1-μm coherent laser radar system. This is, to our knowledge, the first demonstration of SLM operation from a diode laser pumped Tm:Ho:YAG laser.

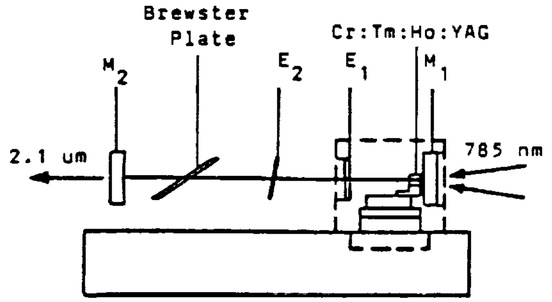

Fig. 1. Schematic of the diode laser pumped Tm:Ho:YAG oscillator.

The resonator configuration is shown in Fig. 1. The flat resonator mirror, M_1, is a high reflector at wavelengths near 2100 nm and transmits 88% of the diode laser pump light near 785 nm. Resonator mirror M_2 serves as the output coupler transmitting ~2.5% of the laser light near 2100 nm. The radius of curvature of this mirror is 7.5 cm and the two resonator mirrors are in a near hemispheric configuration being separated by ~7.5 cm. The Cr:Tm:Ho:YAG crystal used in these experiments has nominal dopant concentrations of 7.9×10^{19}-cm^{-3} Cr^{3+}, 8.2×10^{20}-cm^{-3} Tm^{3+}, and 5.0×10^{19}-cm^{-3} Ho^{3+}. The Cr ions are present for flashlamp pumping and do not play an active role in the energy transfer under diode pumping.[3] The crystal dimensions are 4 mm wide × 2 mm high × 3 mm long. The endfaces of the crystal are polished flat and AR coated with the power reflectivity being <0.2% at wavelengths near 2100 nm and <5.0% at the 785-nm pump wavelength. The 3-mm long laser crystal transmits 26% of the incident 785-nm diode laser pump light. The crystal is mounted on a three-stage thermoelectric (TE) cooler allowing its temperature to be varied from +30 to −40°C. All the data reported below is for operation at −40°C. The TE cooler and laser crystal are enclosed in a nitrogen-purged chamber and one end of the laser crystal is ~0.5 mm from M_1.

The uncoated solid fused silica etalons, E_1 and E_2, have thicknesses of 1.0 and 0.09 mm, respectively. The thin etalon, E_2, is used to control the laser wavelength and the thick etalon, E_1, is used to obtain SLM operation. The fused silica Brewster plate controls the polarization of the laser. The laser is longitudinally pumped with the output from a ten-stripe 500-mW cw phase coupled diode laser array (Spectra Diode Labs SDL-2432-P1). The diode laser wavelength is tuned to the Tm:Ho:YAG absorption maximum near 785 nm and controlled there using another TE cooler which is integral to the diode laser package. The optical train that couples the diode laser output into the laser crystal delivers ~85% of the diode laser output to the resonator end mirror, M_1, and focuses it to a spot size of ~88 × 37 μm in the Cr:Tm:Ho:YAG crystal.

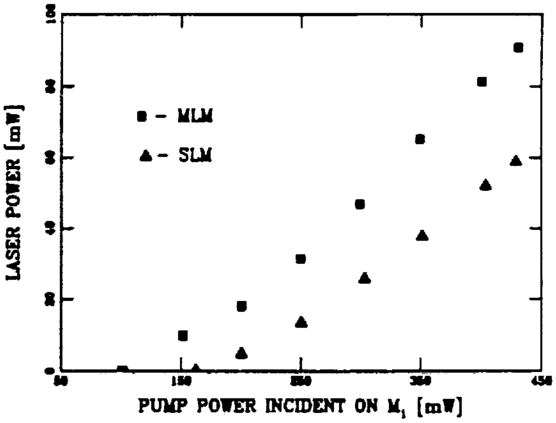

Fig. 2. Laser output power near 2100 nm vs diode laser pump power near 785 nm incident on rear cavity mirror M_1.

With the two intracavity etalons removed, the output from the laser is made up of several longitudinal modes at both 2090 and 2096 nm. The output power vs pump power incident on M_1 for this TEM$_{00}$ multiple-longitudinal-mode (MLM) operation at −40°C is shown in Fig. 2 (squares). The oscillation threshold occurs at 100 mW and the slope efficiency for points well above threshold is 33%. The nonlinear behavior near threshold is characteristic of quasi-three-level laser operation.[6,7] Approximately 65% of the pump power incident on M_1 is absorbed by the laser crystal. Therefore, a plot of output power vs absorbed pump power would yield a slope efficiency of 51%. This compares favorably with the theoretical maximum slope efficiency for Tm:Ho:YAG lasers of 75% (i.e., $\eta_s = 2\eta_{qd}$ where $\eta_{qd} = \lambda_p/\lambda_L$ = 785/2090 = 37.6% and the factor of 2 is for perfect two-for-

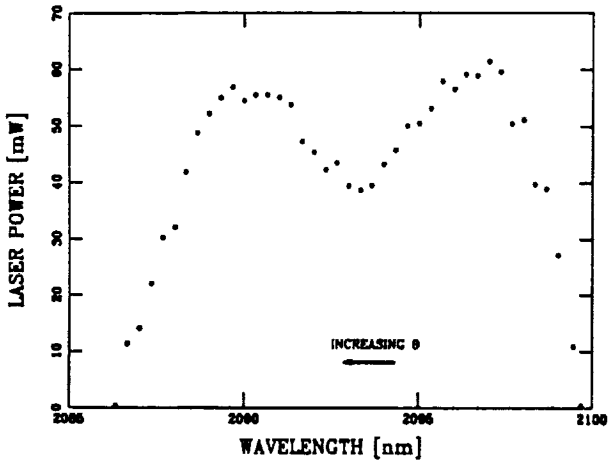

Fig. 3. Output power vs wavelength obtained by tilt tuning the 0.09-mm thick intracavity etalon E_2 and with the 1.0-mm thick intracavity etalon E_1 removed from the cavity.

one cross relaxation of the Tm ions[3]). Due to the Brewster plate and a slight tilt of the laser crystal in the near hemispheric resonator, the TEM_{00} laser output is slightly astigmatic. The degree of astigmatism is a strong function of the exact mirror separation. When the SLM data in Figs. 1–4 were taken, the ellipticity was ~1.16 × 1.0, and the TEM_{00} spot size on M_1 ($1/e^2$ intensity radius) calculated from the far field divergence was ~81 × 70 μm.

If the thin (0.09-mm thick) etalon is inserted into the cavity, the laser typically operates on three to four nonadjacent longitudinal modes spread out over 30 GHz. The laser wavelength depends on the incident angle between the axis of the laser mode and the normal to the etalon surface. Figure 3 is a plot of output power vs wavelength obtained by angle tuning the thin etalon. The pump power incident on M_1 during the collection of data for Fig. 3 was 430 mW. The initial tilt angle in Fig. 3 is ~5° at $\lambda = 2100$ nm and increases as λ decreases. The lower output power at 2090 nm compared with 2097 nm is due to increased walk-off loss due to the higher tilt angle of the thin etalon. Operation with 78 mW of output power near 2090 nm can also be obtained with a tilt angle of ~2°.

With all the other elements shown in Fig. 1 in place, insertion of thick etalon E_1 into the cavity at near normal incidence results in SLM operation as shown in Fig. 4. Figure 4(A) shows the laser spectrum as measured with a scanning Fabry-Perot interferometer. The two peaks are separated by the 15-GHz free spectral range (FSR) of the interferometer and the linewidth is due to instrument resolution. The longitudinal modes of the laser are separated by ~2 GHz and, if other longitudinal modes were present, they would easily be resolved by the Fabry-Perot. Figure 4(B) shows the spectrum as measured by a scanning confocal interferometer having a FSR of 300 MHz. Again the 1.7-MHz FWHM linewidth is due to instrument resolution. The laser was operating at 2090.3 nm, as measured with a 0.25-m monochromator, and the output power was 55 mW when the spectra of Fig. 4 were recorded. The output power vs pump power incident on M_1 for SLM operation at 2090 nm and at −40°C is shown in Fig. 2 (triangles). Oscillation threshold occurs at 162 mW and the slope efficiency for points well above threshold is 27%. By angle tuning thin etalon E_2, SLM operation was demonstrated at several points in the tuning range between 2088 and 2099 nm with a response vs wavelength very similar in shape to that shown in Fig. 3.

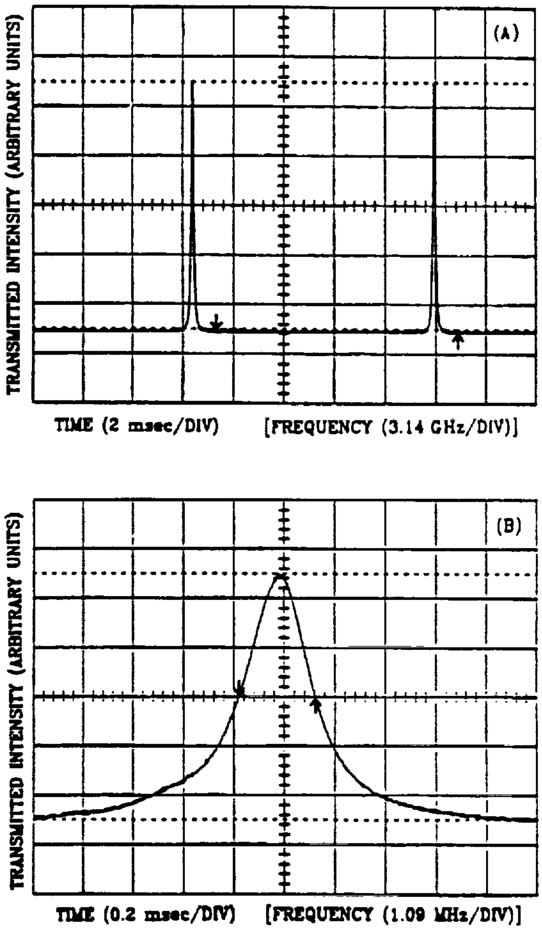

Fig. 4. Spectrum of the single-longitudinal-mode Tm:Ho:YAG laser. (A) The spectrum as measured using a scanning Fabry-Perot interferometer. The peaks are separated by the 15-GHz free spectral range of the interferometer and the linewidth is due to instrument resolution. (B) The spectrum as measured with a scanning confocal interferometer whose free spectral range is 300 MHz. The linewidth is again due to instrument resolution.

If the 2.5% output coupler (M_2 in Fig. 1) is replaced with a 0.5% output coupler, the laser can also be made to operate SLM and tune at wavelengths near 2121 nm. This dependence of operating wavelength on output coupling in Tm:Ho:YAG lasers has been described by Fan *et al.*[3]

In summary, we have achieved broadly tunable SLM operation from a TE-cooled diode laser pumped Tm:Ho:YAG laser operating at −40°C. No special precautions have been taken for long term stability with the current hardware. The laser mirrors are mounted on an aluminum baseplate and the TE cooler for the laser crystal is not actively stabilized. Even so, the laser runs for many tens of minutes before two-mode operation or longitudinal mode hops occur. In the near future, we will replace the aluminum baseplate with a super Invar baseplate and actively stabilize the TE cooler to achieve long term stability.

This research was part of a Small Business Innovation Research program monitored by the Defense Meteorological System's Advanced Technology Office at the U.S. Air Force Space Division, Los Angeles Air Force Base, California.

References

1. G. Huber, E. W. Duczynski, and K. Petermann, "Laser Pumping of Ho-, Tm-, Er-Doped Garnet Lasers at Room Temperature," IEEE J. Quantum Electron. QE-24, 920–923 (1988).

2. T. Y. Fan, G. Huber, R. L. Byer, and P. Mitzscherlich, "Continuous-Wave Operation at 2.1 μm of a Diode-Laser-Pumped, Tm-Sensitized Ho:$Y_3Al_5O_{12}$ Laser at 300 K," Opt. Lett. 12, 678–680 (1987).

3. T. Y. Fan, G. Huber, R. L. Byer, and P. Mitzscherlich, "Spectroscopy and Diode Laser-Pumped Operation of Tm,Ho:YAG," IEEE J. Quantum Electron. QE-24, 924–933 (1988).

4. G. J. Kintz, R. Allen, and L. Esterowitz, "Continuous-Wave Laser Emission at 2.02 μm from Diode-Pumped Tm^{3+}:YAG at Room Temperature," in *Technical Digest, Conference on Lasers and Electro-Optics* (Optical Society of America, Washington, DC, 1988), paper FB2.
5. T. J. Kane and R. W. Wallace, "Performance of a Diode-Pumped Tm:Ho:YAG Laser at Temperatures Between −55 and +20°C," in *Technical Digest, Conference on Lasers and Electro-Optics* (Optical Society of America, Washington, DC, 1988), paper FB3.
6. T. Y. Fan and R. L. Byer, "Modeling and CW Operation of a Quasi-Three-Level 946 nm Nd:YAG Laser," IEEE J. Quantum Electron. QE-23, 605–612 (1987).
7. W. P. Risk, "Modeling of Longitudinally Pumped Solid-State Lasers Exhibiting Reabsorption Losses," J. Opt. Soc. Am. B 5, 1412 (1988).

APPENDIX F

INJECTION SEEDED OPERATION OF A Q-SWITCHED Cr,Tm,Ho:YAG LASER

Sammy W. Henderson, Charley P. Hale, and James R. Magee
Coherent Technologies, Inc.
P.O. Box 7488
Boulder, CO 80306-7488

to be published in the proceedings of the
Topical Meeting on
Advanced Solid-State Lasers
Salt Lake City, Utah
March 5-7, 1990

ABSTRACT

Single-frequency Tm,Ho:YAG and Tm:YAG lasers operating near 2 μm are attractive sources for several applications including eyesafe laser radar (lidar) and pumping of AgGaSe$_2$ parametric oscillators for efficient generation of longer wavelengths. As part of a program to develop a coherent lidar system using Tm,Ho:YAG lasers, we have developed a diode laser-pumped, tunable, CW, single-longitudinal-mode (SLM) Cr:Tm:Ho:YAG laser and a flashlamp-pumped, single-transverse-mode, Q-switched Cr,Tm,Ho:YAG laser. The CW laser has been used to injection seed the flashlamp-pumped laser, resulting in SLM Q-switched output. Operational characteristics of the CW and Q-switched lasers and injection-seeding results are reported here.

SLAVE OSCILLATOR

The flashlamp-pumped Q-switched slave oscillator utilizes a polarization-coupled, large-volume-TEM$_{00}$ cavity configuration. (See Slave Oscillator in Figure 4.) The end mirrors are flat high reflectors at 2.09 μm and the cavity is dynamically stabilized using the thermal lens of the pumped laser rod. The YAG laser crystal has nominal dopant concentrations of 7.9×10^{19} cm^{-3} Cr^{3+}, 8.2×10^{20} cm^{-3} Tm^{3+}, and 5.0×10^{19} cm^{-3} Ho^{3+}. In order to produce the long duration Q-switched pulses (i.e., the narrow Fourier-transform-limited bandwidth) required for the coherent lidar application, the cavity mirrors are separated by ~ 1.2 m. The output energy vs input energy for operation at ~ 20° C is shown in Figure 1 for both normal mode and single-pulse Q-switched operation at a PRF of ~ 3 Hz. Note that ~ 50% of the normal mode energy is extracted in single Q-switched pulses. This is expected for the dopant concentration utilized since the active Ho ions only store ~ 50% of the energy near room temperature, with the Tm ions storing the other 50%. The transfer time from Tm to Ho is estimated to be > 5 μs, which is much longer than the Q-switched pulse lengths. This slow transfer can result in multiple pulses when the laser is Q-switched;[1] to avoid this we gate the voltage applied to the Pockels cell, bringing the laser cavity back to a low-Q state before the second pulse evolves.

The low slope efficiency shown in Figure 1 is due to the combination of an inefficient flashlamp pump chamber and a very lossy Pockels cell (bad AR coatings). The 5.1% slope efficiency demonstrated by Quarles et al.,[2] in a multiple transverse and normal mode Cr,Tm,Ho:YAG laser, leads us to expect an increase of a factor of four or more in slope efficiency when the cavity losses are minimized and a more efficient pump chamber is utilized. The pulse duration for 30 mJ and 50 mJ Q-switched pulses is ~ 250 ns and ~ 150 ns FWHM, respectively. Although no damage has been experienced, the Q-switched pulse energy has been limited to ~ 50 mJ to date for fear of damaging intracavity optics.

At the 3 Hz PRF used throughout this study, the thermal lens created by the rod is correct for large-volume TEM$_{00}$ operation and excellent mode quality is obtained. The intensity profile of the slave oscillator output, measured by scanning a 100-μm diameter long-wavelength InGaAs photodetector across the beam, is shown in Figure 2. Also shown is a Gaussian fit to the

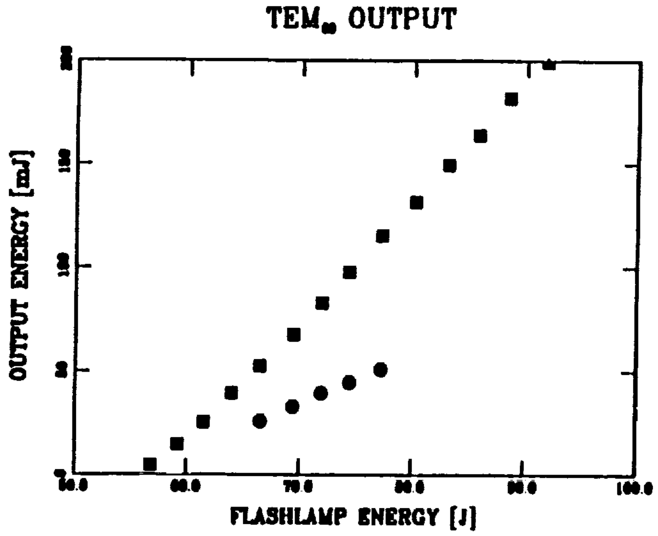

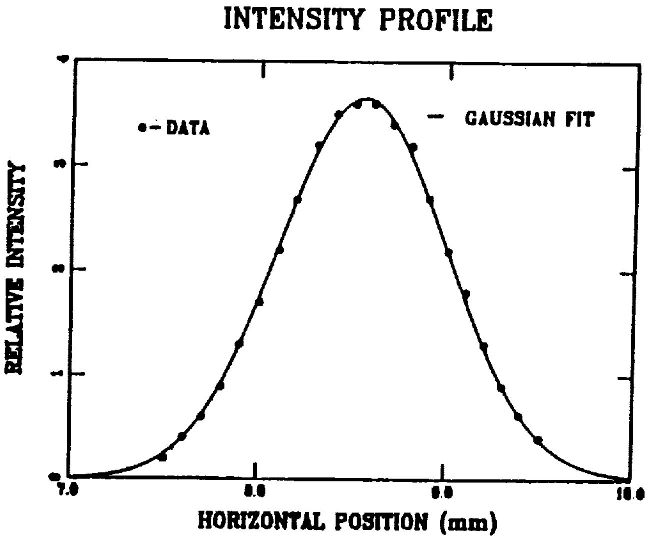

Figure 1. Output pulse energy for TEM_{00} operation vs energy supplied to the flashlamp for both normal-mode and single-pulse Q-switched (circles) operation.

Figure 2. Intensity profile of the TEM_{00} output from the slave oscillator.

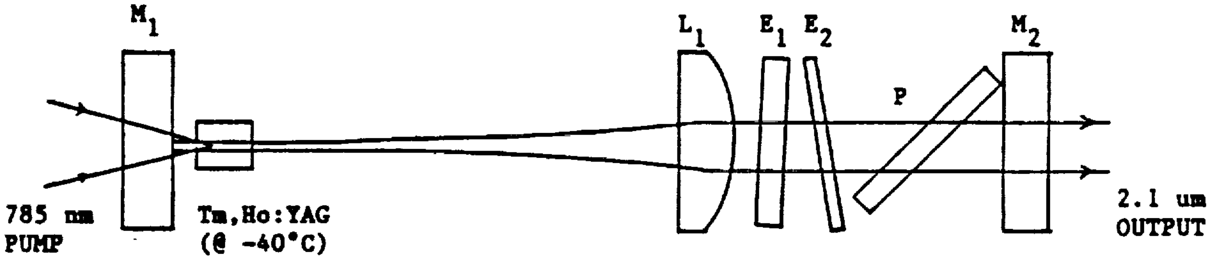

Figure 3. Schematic of the optical configuration used in the single-frequency master oscillator.

data. Operation of the slave laser in any one of the four wavelength regions near 2090, 2096, 2121, and 2128 nm can be obtained by tilt-tuning the intracavity thin-film polarizer. (The transmission of the polarizer for p-polarization light varies with wavelength and the spectral transmission peak can be tuned by small changes in the tilt angle.)

MASTER OSCILLATOR

The diode laser-pumped, CW master oscillator shown in Figure 3 utilizes a linear cavity with an intracavity Brewster plate for polarization control, and two solid fused-silica etalons (thicknesses of 0.5 and 0.09 mm) for frequency control. The 0.09 mm thick etalon, E_2, is uncoated and the 0.5 mm thick etalon, E_1, is coated for 18% reflectivity at 2.09 µm. The intracavity lens, L_1, (focal length = 75 mm) is utilized to provide stability and to minimize the walkoff loss introduced as the 0.5 mm thick etalon is tilted. Both mirrors, M_1 and M_2, are plano/plano with M_1 highly reflecting and M_2 ~ 97.5% reflecting at 2.09 µm. The entire optical train is mounted in a temperature-controlled super invar block. Other than higher frequency stability, the other operational characteristics of this laser are virtually identical to those described in reference 3, so we only provide a summary here. With the laser crystal thermo-electrically cooled to ~ 230 K, we have obtained ~ 50 mW of SLM output power near 2090 nm and 2096 nm using 430 mW of pump power from the diode laser. A scanning confocal interferometer has shown that the linewidth and short-term frequency jitter from this laser are less than 1 MHz. By tilt-tuning the intracavity etalons, tuning over the wavelength range between 2087 and 2099 nm has been achieved. Tuning near 2121 nm has also been demonstrated, using the laser described in reference 3, by changing the reflectivity of the output coupler.

INJECTION SEEDING

The apparatus used for the injection-seeding studies is illustrated in Figure 4. The output of the master oscillator was mode matched and injected into the slave oscillator using the "back" of the intracavity thin-film polarizer. Isolation of ≳ 40 dB is provided by a yttrium iron garnet Faraday isolator. Neutral density filters can be placed in between the master and slave oscillators to reduce the injected intensity. The output of either laser can be analyzed using scanning interferometers and a quarter-meter monochromator. A fast long-wavelength InGaAs photodetector is used to observe the temporal profile of the pulsed output. The longitudinal mode frequency of the slave laser is controlled by translation of a slave cavity end mirror which is mounted on a piezoelectric pusher. Throughout this study the required match between the master oscillator frequency and the slave cavity longitudinal mode frequency was maintained by manually controlling the voltage applied to the end mirror PZT. The "man in the loop" adjusted the PZT voltage so as to minimize the observed pulse buildup time.[4] A second quarterwave plate can be added to the slave oscillator (shown as the optional $\lambda/4$ plate in Figure 4) to minimize spatial hole burning in the laser rod.[5] For the results presented here, the optional waveplate was not utilized.

Figure 5 shows an example of the temporal evolution of the Q-switched slave laser pulse for both seeded and unseeded operation with the wavelength near 2090 nm. The right-most 30 mJ unseeded pulse exhibits longitudinal mode beating at ~ 120 MHz (shown as ~ 20 MHz due to aliasing by the 100 magasample-per-second digital oscilloscope used). Note the earlier buildup time and smooth profile for the left-most seeded pulse. The lack of mode beating on the seeded pulse suggests SLM output. In this example, the seeded laser pulse contains ~ 70% of the energy that the unseeded laser pulse contains. This reduction is probably due to a combination of spatial hole burning in the laser crystal and the lower gain experienced due to the detuning of the seed laser frequency from line center (see next paragraph).

With the experimental conditions the same as those used to produce Figure 5, a scanning Fabry Perot (FP) etalon whose free spectral range (FSR) is 75 GHz was used to measure the spectrum of the slave and master oscillator outputs (see Figure 4). Figure 6 shows the spectrum measured during a 50 second scan with the master oscillator output blocked from the slave oscillator. The "grass" to the left is due to the unseeded Q-switched slave laser output and the smooth peak to the right is due to the master oscillator output. The width of the smooth peaks represents the resolution of the interferometer and the repetitive nature of the display results from scanning by more than 1 FSR. The right-most feature on the display is due to resetting the FP mirror spacing to begin another scan. Figure 6 shows that for this example the bandwidth of the unseeded Q-switched output is ~ 10 GHz and the frequency of the CW master oscillator is offset by ~ 22 GHz from the centroid of the slave laser output

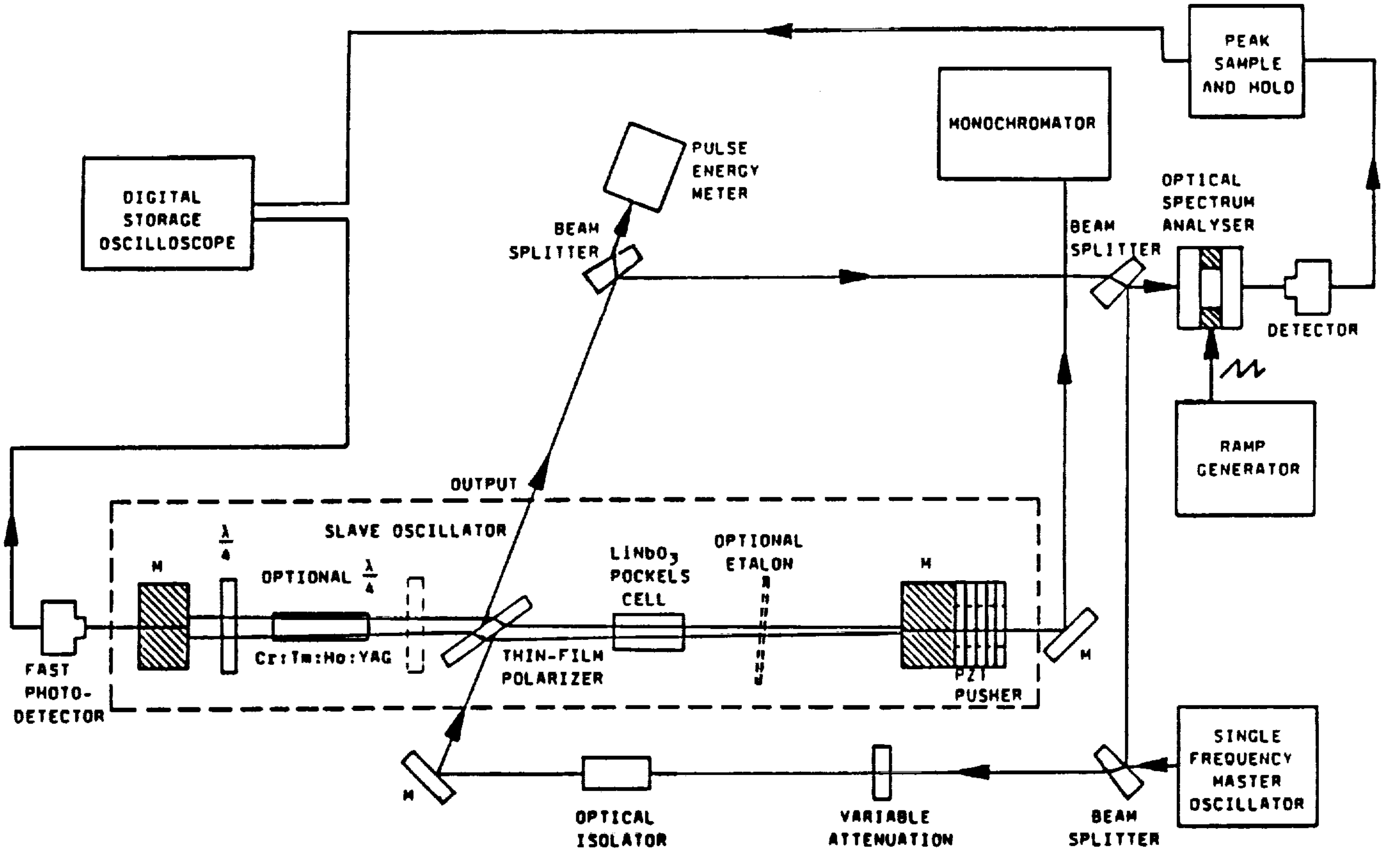

Figure 4. Experimental apparatus used to study injection seeding.

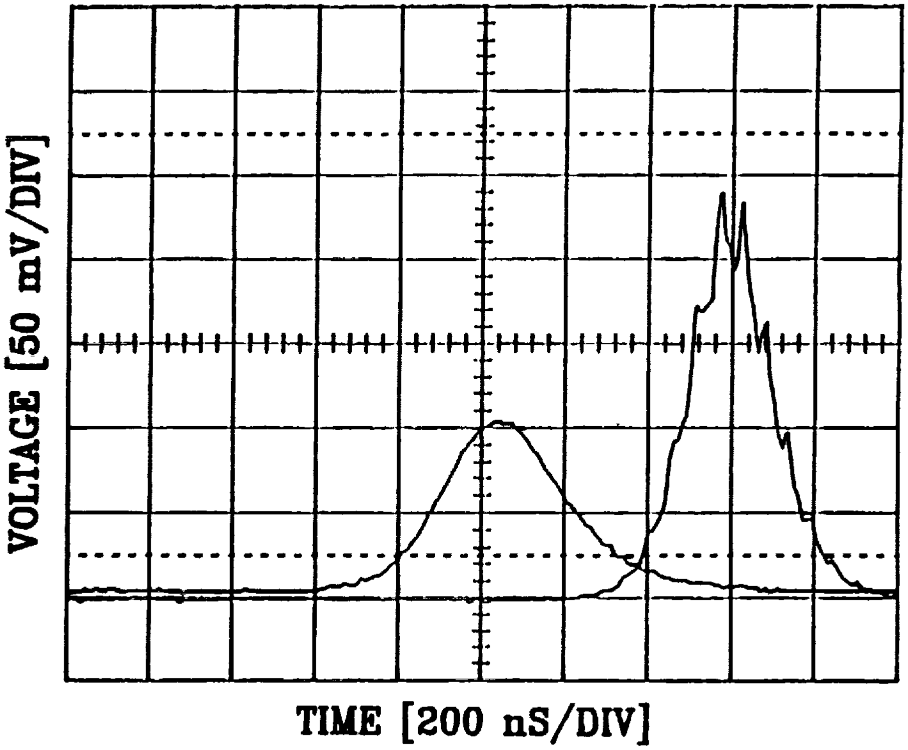

Figure 5. Temporal evolution of the unseeded (right) and seeded (left) Q-switched pulses.

frequency. If the output of the CW master oscillator is allowed to enter the slave oscillator and if the seed radiation is resonant or nearly resonant with a longitudinal mode frequency of the slave oscillator, the spectrum of the slave laser output collapses and is pulled to the longitudinal mode which is closest to that of the seed radiation. This is illustrated in Figure 7 where the experimental conditions were identical to those described in the discussion of Figure 6, except that the master oscillator was allowed to seed the slave oscillator. The peak voltage seen in Figure 7 represents the saturation voltage of the detector circuitry.

Higher resolution spectra of the pulsed output are shown in Figures 8 and 9 for both unseeded and seeded operation. For this measurement a scanning confocal interferometer whose FSR is 300 MHz was used. The upper trace in both figures shows the 50-second voltage ramp used to drive the scanning interferometer. Note that when seeded the spectrum collapses to < 6 MHz FWHM of which a large part is due to the resolution of the interferometer. The transmitted intensity scale in Figure 9 is ten times larger than that of Figure 8. The spectrum of Figure 8 is uniformly filled due to aliasing of the 10-20 GHz wide unseeded spectra into the 300 MHz FSR of the interferometer.

By tuning the wavelength of the master oscillator, we have achieved SLM operation over a ~ 250 GHz (3.7 nm) wide band centered at 2090 nm and ~ 100 GHz (1.5 nm) wide bands centered at 2096.2 nm and 2097.7 nm. At the center of each of these bands, the energy of the seeded SLM pulses is typically 80-90% of that of the unseeded pulses. At the edges of each wavelength band, the seeded energy is ~ 50% of the unseeded energy. Seeding near 2121 nm and 2128 nm has not been attempted at this time.

A measurement of the maximum detuning between the frequency of the master oscillator and that of the nearest slave cavity longitudinal mode, which results in SLM operation, was made as a function of the injected power. This maximum detuning is commonly called the injection-seeding (or locking) range.[6] A large injection-seeding range is useful since it eases the requirements on the servo system locking the frequency of the master oscillator to a slave cavity longitudinal mode. The injection-seeding range vs injected power is shown in Figure 10 for seeding at 2097.8 nm when the unseeded pulse energy was ~ 25 mJ and the seeded pulse energy was ~ 20 mJ. Note that with only 1 mW of injected power the injection-seeding range is ~ 10 MHz. We have also obtained SLM Q-switched operation with only 670 nW of injected power; this point is not shown because the injection-seeding range was so small (< 2 MHz) that a reliable measurement could not be easily made.

SUMMARY

We have demonstrated tunable injection-seeded SLM operation of a room temperature Q-switched Cr,Tm,Ho:YAG laser. To accomplish this task a highly-stable tunable single-frequency CW master oscillator was constructed and a tunable TEM_{00} Q-switched flashlamp-pumped oscillator which produces over 50 mJ/pulse was constructed. In the near future we will construct electronics to automatically servo the slave cavity longitudinal mode frequency resulting in unattended SLM Q-switched operation of the slave laser.

REFERENCES

1. M.E. Storm, "Laser characteristics of a Q-switched Ho:Tm:Cr:YAG," Appl. Opt. 27, 4170 (1988).
2. G.J. Quarles, A. Rosenbaum, C.L. Marquardt, and L. Esterowitz, "High-efficiency 2.09 μm flashlamp-pumped laser," Appl. Phys. Lett. 55, 1062 (1989).
3. S.W. Henderson and C.P Hale, "Tunable single-longitudinal-mode diode laser pumped Tm:Ho:YAG laser," Appl. Opt. 29, April 20, 1990.
4. L.A. Rahn, "Feedback stabilization of an injection-seeded Nd:YAG laser," Appl. Opt. 24, 940 (1985).
5. E.S. Fry and S.W. Henderson, "Suppression of spatial hole burning in polarization-coupled resonators," Appl. Opt. 25, 3017 (1986).
6. Y.K Park, G. Guiliani, and R.L. Byer, "Single axial mode operation of a Q-switched Nd:YAG oscillator by injection seeding," IEEE J. Quant. Electron. QE-20, 117 (1984).

ACKNOWLEDGMENTS

This research was sponsored by the Defense Meteorological Systems Advanced Technology Office at the U.S. Air Force Space Division under SBIR contract F04701-87-C-0144, (Lt. Alvin Lee, monitor). Partial support was also provided by NASA/Marshall Space Flight Center under contract NAS8-37580 (W.D. Jones, technical monitor).

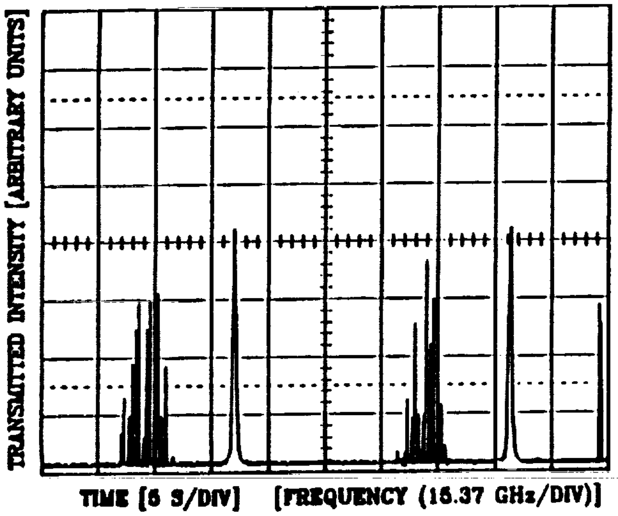

Figure 6. Unseeded spectra as observed using a scanning interferometer whose free spectral range is 75 GHz.

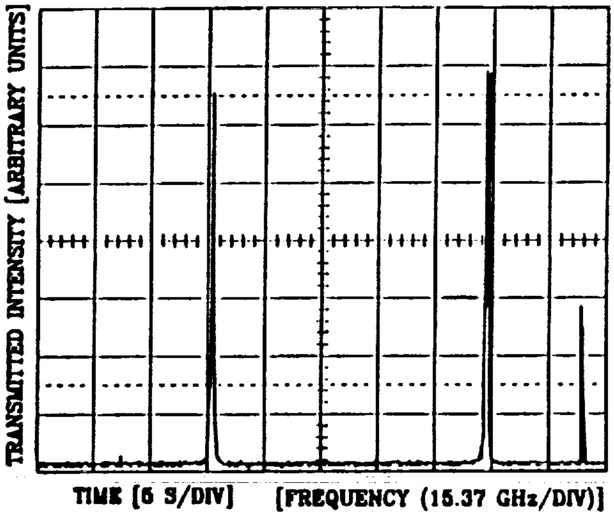

Figure 7. Seeded spectra as observed using a scanning interferometer whose free spectral range is 75 GHz.

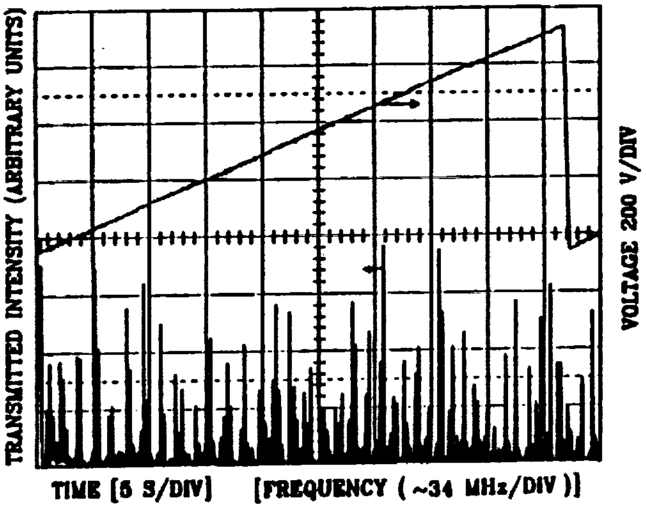

Figure 8. Unseeded spectra as measured using a scanning interferometer whose free spectral range is 300 MHz.

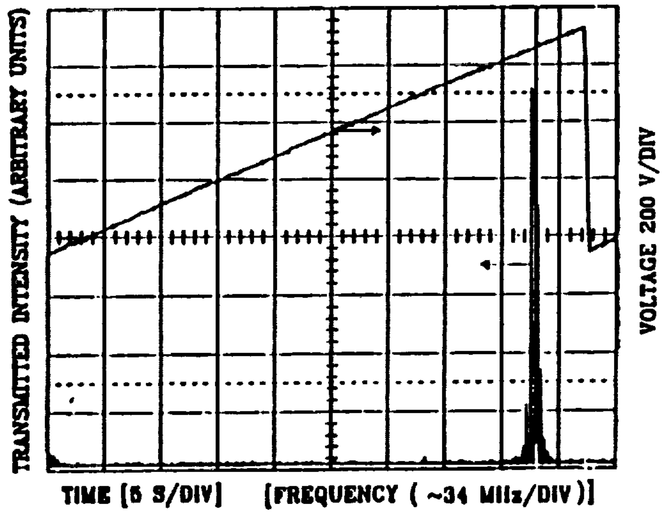

Figure 9. Seeded spectra as measured using a scanning interferometer whose free spectral range is 300 MHz. The transmitted intensity scale is ten times that of Figure 8.

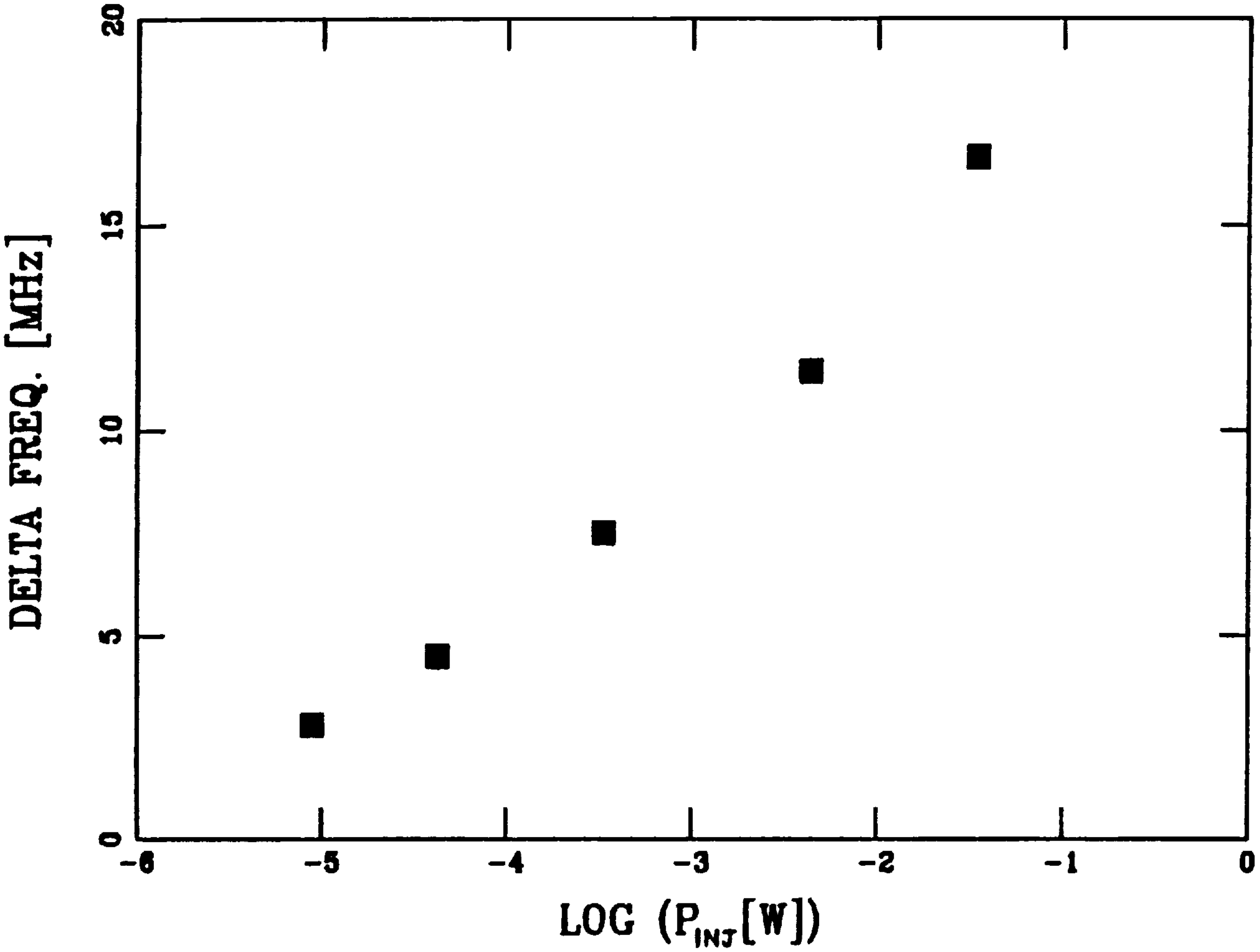

Figure 10. Injection-seeding range vs injected power for operation near 2097.8 nm.

APPENDIX G

β CALIBRATION CONSIDERATIONS FOR THE AFGL PULSED CO_2 COHERENT LASER RADAR

Michael J. Kavaya
Coherent Technologies, Inc.

An AFGL ground-based pulsed CO_2 coherent laser radar (lidar) has been used and will be used in the future to obtain calibrated profiles of the atmospheric aerosol backscatter coefficient β (Alejandro et al., 1990). (See Section 11 for references.) This appendix attempts to list the legion of calibration choices and trade-offs faced by the lidar designer and operator. The typical trade-offs for improved calibration are: increased cost, increased complexity of lidar design, increased difficulty, and/or increased measurement/calibration time. The overall goals are:

1. Reduce random noise
2. Model measurement physics and reduce systematic errors
3. Obtain accurate system zero
4. Obtain accurate system gain

1. Telescope Overlap Function

The telescope overlap function (TOF), $\theta(R)$, also referred to as crossover function or geometrical form factor, is a desired term in the coherent lidar equation, for received signal power or SNR, that is used to process received data and produce a $\beta(R)$ or $\beta(z)$ profile. Ideally, $\theta(R)$ represents all range dependent effects on the signal that have not been included in the lidar equation and data processing steps. In this perspective, the name telescope overlap function is a misnomer. The lidar equation employed, $P_r(R)$ or SNR(R), may originate from analytic theory or from computer numerical analysis, or may combine one of these techniques with a heuristic modification of the equation. A past analysis of $\theta(R)$ for a specific CO_2 coherent lidar system (Kavaya and Menzies, 1985) revealed that incorrect use or neglect of $\theta(R)$ could result in values of β in error by factors up to 30. Since that study was performed, newer lidar equations have become available (Frehlich and Kavaya, 1990) that include more of the range-dependent physics of the coherent lidar measurement. Therefore, the TOF is an evolving function, and is specific to each lidar system. It may or may not need to include the effects of misalignment of the transmitted (XMTR) beam and the back-propagated local oscillator (BPLO) beam; a bistatic lidar with separated XMTR and BPLO; beam truncation by optical elements; obscuration by the telescope (if any); the spatial profile of the XMTR or BPLO beams, if not Gaussian; the detector size, shape, and spatial profile of quantum efficiency; mis-positioning of the detector (related to misalignment); and pulsed profile temporal shape effects. For a bistatic lidar measuring at short ranges, $\theta(R)$ will be significant due to the XMTR/BPLO beam separation.

The best determination of $\theta(R)$ is to fire the lidar into an unchanging atmosphere with well known total extinction $\alpha(R)$ and aerosol backscatter $\beta(R)$ profiles. With enough shots averaged to reduce the effects of speckle; the SNR(R), $\beta(R)$, and $\alpha(R)$ profiles, and the chosen lidar equation could be used to calculate $\theta(R)$. This may be impossible for the present. A relative (vs absolute) $\theta(R)$ curve may be determined if the lidar is fired into a homogeneous atmosphere where $\beta(R) = \beta$ and $\alpha(R) = \alpha$, both constants vs range. The most likely scenario is to model $\theta(R)$ to include as much physics as possible that is not included in the lidar equation (Ancellet et al., 1986). This absolute model of $\theta(R)$ may then be checked by varying the settings of the lidar and comparing experiment to theory, by firing into an assumed uniform atmosphere and looking for a uniform $\beta(R)$ result, or by varying the elevation angle of the lidar and comparing the resultant β values at equal heights.

2. Calibration Target

The method of choice for calibrating pulsed coherent lidar measurements of β is to use a hard calibration target (Kavaya et al., 1983; Kavaya, 1985; Kavaya and Menzies, 1985; Kavaya, 1987). The use of the total backscatter to Rayleigh backscatter ratio calibration technique, which is used in the visible wavelength region (often in concert with a hard target anyway), is not feasible at CO_2 wavelengths since molecular backscatter is negligible. The calibration technique that assumes a functional relationship between backscatter and extinction (a field of research in itself) does not apply since CO_2 backscatter is dominated by aerosol particles while extinction is dominated by molecules. The rule of thumb that says to calibrate an instrument with a known target as close in character as possible to the eventual target (e.g., in this case, aerosol particles, oil drops, homogeneous spheres, etc.) is not practical since it is difficult to make a well characterized target that mimics aerosol particles, and since this calibration target would have to fill the expected measurement volume, which is more than 150 m long for a 1-μs long pulse. The technique of using a comprehensive lidar equation and then characterizing the reflectance or transmittance or gain of every component is very hard and prone to errors as components change with time.

The ideal calibration target would be easy to fabricate, inexpensive, lightweight, durable, and be as close to diffuse or Lambertian in its scattering behavior as possible. A large target area is desired so that it may be turned with respect to the lidar beam (to avoid specular reflectance) while still projecting a sufficient area to encompass the entire beam. The target should be turned about a vertical axis to avoid backscatter from the ground. While the field target should be large, a small witness sample with exactly the same reflectance behavior is desired to allow laboratory calibration of the desired reflectance. The laboratory calibration of the witness sample should employ conditions that match, as closely as possible, the use of the large field target in calibrating the lidar system. Specifically, continuity should be sought for:

1. the target itself, its reflectance characteristics,
2. the laser wavelength and linewidth,
3. the incident and reflected (detected) polarization states,
4. the polar angle of the laser beam with respect to the normal to the target (45^0 is a nice compromise between avoiding specular reflection and losing projected area, i.e., projected area = 71% of actual area),
5. the incident and detected solid angles (as close as possible),
6. the size relationship of the target area, the illumination area, and the detector's field of view (it is recommended that the target's projected area be the largest, and be sufficiently big that the beam is always contained in the projected area despite laser pointing jitter and beam wander due to atmospheric refractive turbulence),
7. complete averaging of speckle.

The target should exhibit no opposition effect (cube corner behavior) since the necessarily different solid angles employed in the laboratory calibration of the witness sample and the field calibration of the lidar will lead to errors in the target reflectance parameter $\rho*$, and hence errors in β.

It is desirable to ensure that the target is moving randomly over a distance of many wavelengths of light in order to average speckle effects. Often the wind or vibration from traffic will guarantee this. The probability distribution function (PDF) of the received IF power from the target shots should be checked to confirm negative exponential behavior.

The optical train used for atmospheric and hard target measurements should be identical. Any differences should be compensated for.

For CO_2 laser work, the researcher should employ the Lidar

Target Calibration Facility at NASA's Jet Propulsion Laboratory (Kavaya, 1985). Presently, there is no charge for calibration of witness samples.

3. Atmospheric Extinction

Proper derivation of the $\beta(R)$ profile requires knowledge of the total extinction profile $\alpha(R)$ that was encountered by the lidar beam. Components of extinction include molecular absorption, molecular scattering, aerosol absorption, aerosol scattering, and the effects of clouds. Ideally, $\alpha(R)$ would be measured independently for each lidar shot and used in data reduction. Practically, however, it is difficult to obtain $\alpha(R)$ even as an average over the measurement time. Models of the atmosphere may be employed to calculate $\alpha(R)$ for certain assumed conditions. This is probably the only practical choice at present. However, the atmosphere models do not account for a ground-based lidar shooting through a boundary layer. It is highly recommended that a separate measurement run of the lidar (aiming slightly above horizontal) be employed to determine the total extinction coefficient (assumed constant) and height of the boundary layer (Kavaya and Menzies, 1985).

4. Lidar System Zero

If one could order an atmosphere with $\beta = 0$, then the range dependent system zero profile or minimum detectable β profile could be experimentally determined. Since this is impossible, one has to choose a method of determining this curve. This information is needed to subtract any DC offsets from the data before processing, and to display a minimum detectable β curve along with the calculated β curve.

Choices available include blocking the transmitter telescope, using pretrigger recorded data (before the laser fires), or using data at ranges so large that there can be no signal. Blocking the telescope may create scattered light and electronics saturation that is not present during actual measurements. The pretrigger data may not include noise caused by the firing of the laser. The large range data may miss ringing of the electronics caused by firing the laser. The researcher should examine signals from all three techniques to determine the best approach.

5. Effects of Transmitted Pulse Profile

The effects of the actual temporal profile of the transmitted laser pulse can affect the accuracy of the calculated $\beta(R)$ profile (Kavaya and Menzies, 1985). The most accurate approach is to employ a lidar equation that has not assumed anything about the pulse shape or duration. However, if the pulse shape and duration are repeatable, a range-dependent correction factor may be calculated and applied during data reduction. Unfortunately, this correction profile depends on the total extinction profile, $\alpha(R)$.

6. Averaging a Nonlinear Function of Received Power

Because of speckle fluctuations, many lidar shots are averaged to obtain an estimate of the mean profile of received IF power. However, care must be taken since often the voltage into the A/D converter is a nonlinear function of IF power. Examples include outputs voltages that are the square root of power or the logarithm of power. Averaging these voltages over many pulses and performing the inverse operation on the average, e.g., V^2 or 10^V, will cause errors in $\beta(R)$ (Kavaya and Menzies, 1985). Ideally, it would be arranged to average a voltage linearly proportional to IF power. If more dynamic range is needed, then parallel A/D converters, or a switch to higher gain during the return signal, or a ramping up of gain should be considered. If this is not possible, then correction profiles for $\beta(R)$ can be calculated from knowledge of the nonlinear relationship and the PDF of the detected voltage.

7. Pulse Energy Normalization

Ideally, the received signal from every shot would be normalized by the pulse energy of that shot. Summing the pulse energies independently and dividing the summed signals by the energy sum may cause systematic error. If the laser is known to have sufficiently small fluctuations in transmitted energy, then the normalization step may be skipped, and appropriate error bars added to the $\beta(R)$ profile.

8. Gain Reduction for Hard Target Data

The reflectance ρ^* [sr^{-1}] of hard targets is typically so large compared to atmospheric β (actually $\beta c\tau_p/2$ sr^{-1}) that the lidar receiver gain must be decreased. Changing the telescope aperture in any way is not advisable since this changes the physics of the heterodyne detection, and hence changes the correct lidar equation. A convenient technique is to reduce the receiver gain by a known ratio (i.e., lower the gain by a known number of dB). Preferably, this gain reduction is accomplished with optical neutral density filters or low reflectance beamsplitters rather than with lower electronic gain, so that target calibration is performed under conditions similar to high β measurements. (The larger output of the beamsplitter could be used for a direct detection measurement for estimating ρ^*.) This technique is fine provided the recorded voltage is proportional to the IF signal power or its square root. Then the ratio of the two gains employed is all that is required. However, the use of a logarithmic amplifier in conjunction with this gain ratio technique can make proper calibration very hard (Kavaya and Menzies, 1985). The absolute values of the two receiver gains are then needed, which are much harder to obtain than their ratio.

9. Receiver Gain vs Signal Size

The lidar receiver should be mapped out to determine if its gain varies with signal size, especially for low signals. If the receiver gain is not constant, then the predetermined map should be used during data reduction.

10. Receiver Gain vs Signal Frequency

The return signal from a hard target duplicates the temporal profile of the transmitted pulse. The atmospheric return signal varies much slower in a mean value sense, but does have speckle fluctuations imposed on it. Care should be exercised to ensure the effect of the spectrum of the received signal on the receiver gain is understood.

11. Receiver Saturation

Saturation of any of the receiver components will cause errors in $\beta(R)$. The absence of saturation in each component should be checked.

12. Detector Operating Point

The DC and AC load lines imposed on the photodetector by the bias circuit and preamplifier should be chosen to provide linear operation over the required dynamic range of the signal (Post and Cupp, 1990).

13. Shot-Noise-Limited Operation

The term shot-noise-limited is ambiguous. Most researchers simply mean that shot noise is some factor larger than all other sources of noise together. The adjective has also been misused to mean that shot noise equals the sum of other noise sources. It should be arranged that shot noise is a least 10 times larger than the other noise. Otherwise, a correction factor should be inserted into the lidar equation (Post and Cupp, 1990).

14. Detector Quantum Efficiency

Many HgCdTe detectors are delivered with only the DC quantum efficiency specified. The actual AC quantum efficiency at the signal IF frequency should be employed in the lidar equation.

15. Misalignment

Both the lidar equation and the TOF model should include misalignment effects (but include each effect only once). Data should then be taken vs parameters of the lidar system such as XMTR and BPLO radii and focal ranges, and detector (x,y,z) position to confirm correct alignment. Maximizing the signal from a hard target at some close range does not provide good alignment.

16. A-Scope Capability

The researcher should be able to observe a pulse averaged A-scope display to confirm lidar operation

17. Polarization of Light

The fact that β is really a 4 x 4 Mueller matrix and that each optical component affects the polarization of the laser light should be accounted for (Kavaya, 1987; Anderson, 1989).

18. Neglected Processes

The usual lidar equation neglects multiple scattering, Rayleigh scattering, fluorescence, resonant fluorescence, Raman scattering, and any effect of the beam on the atmosphere itself.

19. Refractive Turbulence

Refractive turbulence effects may affect even CO_2 lidar systems when a long horizontal path is used for calibration. The lidar equation should include these effects (Frehlich and Kavaya, 1990). For collimated beams, the importance of refractive turbulence can be determined by measuring the scintillation of the on-axis transmitted irradiance at the calibration target.

20. Secondary Calibration Technique

A secondary calibration technique, that is much easier to do than the primary hard target technique, is desirable in order to provide frequent checks on lidar gain stability.

21. Data Quality Monitor

A real-time data quality monitor would alert the lidar operator of problems, and could save considerable amounts of time.

22. Signal Processing Hardware

Digital signal processing may provide more accuracy and flexibility than analog processing (e.g., a saw processor).

23. SNR or Power Calibration

Calibration using the aerosol and target SNR values removes any gain drifts in the system provided that shot noise is proportional to the system gain. Calibration using IF power values will be more accurate if the system gain is constant since estimation of only $S - N$ is needed rather than $(S - N)/N$.

24. Choice of Signal Spectrum Location

The typical heterodyne coherent lidar system has a frequency offset f_o between the pulsed and LO lasers. The nominal IF signal frequency from a nonmoving target is therefore f_o. In addition, the receiver bandwidth is designed to accept IF signals over the span of $f_o \pm 2V_{max}/\lambda$, where V_{max} is the highest allowed unidirectional radial wind velocity, which causes a Doppler shift in the received optical frequency. There are three reasons to choose a large value of f_o. First, electronic components are less expensive for smaller fractional bandwidths. In this case, the fractional bandwidth would be $(4\ V_{max})/(\lambda f_o)$. Second, it is easier to achieve a flat noise floor with smaller fractional bandwidths. A flat noise floor is desirable for many signal processing steps, such as noise subtraction. Third, the receiver will experience direct detection current as the laser pulse scatters during its transmission out of the lidar, and also when large returns from hard targets are received. The spectrum of the direct detection current will be approximately the spectrum of the transmitted pulse profile, i.e., DC to some upper frequency f_u. It is important that the direct detection signals do not saturate the receiver electronics, and therefore it is recommended that $f_u \ll f_o - 2\ V_{max}/\lambda$.

NASA
National Aeronautics and Space Administration

Report Documentation Page

1. Report No.
NASA CR-4347

2. Government Accession No.

3. Recipient's Catalog No.

4. Title and Subtitle
Theory of CW Lidar Aerosol Backscatter Measurements and Development of a 2.1-µm Solid-State Pulsed Laser Radar for Aerosol Backscatter Profiling

5. Report Date
March 1991

6. Performing Organization Code

7. Author(s)
M.J. Kavaya, S.W. Henderson, and R.G. Frehlich

8. Performing Organization Report No.

9. Performing Organization Name and Address
Coherent Technologies, Inc.
P.O. Box 7488
Boulder, Colorado 80306

10. Work Unit No.
M-656

11. Contract or Grant No.
NAS8-37580

12. Sponsoring Agency Name and Address
National Aeronautics and Space Administration
George C. Marshall Space Flight Center
Marshall Space Flight Center, Alabama 35812

13. Type of Report and Period Covered
Contractor Report/Final

14. Sponsoring Agency Code

15. Supplementary Notes

Prepared for Information and Electronic Systems Laboratory,
Science and Engineering Directorate

16. Abstract

The performance and calibration of a focused, continuous wave, coherent detection CO_2 lidar operated for the measurement of atmospheric backscatter coefficient, B(m), was examined. This instrument functions by transmitting infrared (10 micron) light into the atmosphere and collecting the light which is scattered in the rearward direction, Two distinct modes of operation were considered. In volume mode (VM), the scattered light energy from many aerosols is detected simultaneously, whereas in the single particle mode (SPM), the scattered light energy from a single aerosol is detected. The analysis considered possible sources of error for each of these two cases, and also considered the conditions where each technique would have superior performance. The analysis showed that, within reasonable assumptions, the value of B(m) could be accurately measured by either the VM of SPM method. The understanding of the theory developed during the analysis was also applied to a pulsed CO_2 lidar operated by the Geophysical Laboratory, Hanscomb AFB, MA. The CW Tm, Ho: YAG solid-state oscillator was demonstrated by Coherent Technologies, Inc. (CTI) under this contract. Preliminary results of field testing of a solid state 2-micron lidar using this CW oscillator are included in the report. This study was motivated by the need to better understand the performance of NASA's proposed Laser Atmospheric Wind Sounder (LAWS) lidar an Earth observing system (EOS) facility instrument scheduled for a 1998 launch.

17. Key Words (Suggested by Author(s))
Lidar, Lidar Calibration, Remote Sensing, Atmospheric Measurements, Atmospheric Aerosol Backscatter, Earth Observing System (EOS), Laser Atmospheric Wind Sounder (LAWS), Global Backscatter Experiment (GLOBE)

18. Distribution Statement
Unclassified-Unlimited
Subject Category: 43, 74

19. Security Classif. (of this report)
Unclassified

20. Security Classif. (of this page)
Unclassified

21. No. of pages
128

22. Price
A07

For sale by the National Technical Information Service, Springfield, VA 22161-2171

NASA-Langley, 1991